NKS-497
ISBN 978-87-7893-595-3

Reactor Pressure Vessel LTO Assessment

Pål Efsing[1,4]
Jonas Faleskog[1]
Daniela Klein[1]
Noora Hytönen[2]
Sebastian Lindqvist[2]
Mattias Thuvander[3]
David Mayweg[3]
Johan Blomström[4]

[1] Department of Solid Mechanics, Royal Institute of Technology (KTH), SE-10044 Stockholm Sweden
[2] VTT Technical Research Centre of Finland Ltd, PO Box 1000, FI-02044 VTT, Helsinki, Finland
[3] Chalmers University of Technology, Department of Physics, SE-41296, Göteborg, Sweden
[4] Ringhals AB, SE-43285 Väröbacka, Sweden

March 2025

Abstract

As part of the NKS-R program, VTT, Chalmers University of Technology and KTH have extended the assessment of micro-structural and mechanical property evolution during irradiation to analyze the as-aged material properties of the retired reactor pressure vessel, RPV, from Barsebäck unit 2. The testing has included impact and fracture mechanical testing of material, as well as high and low magnification microstructural characterization of the weld metal from the reactor pressure vessel using LOM, SEM and APT. Due to the nature of the work, the NKS-project is connected to several adjacent activities, including support from the Finnish Nuclear Safety Program, the SAFIR-program, the Swedish Radiation Safety Authority SSM and Swedish Centre for Nuclear Technology, and SKC.

Key words

Low alloy steel, irradiation effects, fracture toughness, ductile to brittle transition temperature, constraint effects, high resolution microscopy, microstructural characterization

NKS-497
ISBN 978-87-7893-595-3
Electronic report, March 2025
NKS Secretariat
P.O. Box 49
DK - 4000 Roskilde, Denmark
Phone +45 4677 4041
www.nks.org
e-mail nks@nks.org

Reactor Pressure Vessel LTO Assessment

Final Report from the NKS-R RePOUSSES 2024 activity

(Contract: AFT/NKS-R(24)142/8)

Pål Efsing[1,4], Jonas Faleskog[1], Daniela Klein[1]
Noora Hytönen[2], Sebastian Lindqvist[2]
David Mayweg[3], Mattias Thuvander[3]
Johan Blomström[4]

[1] Department of Engineering Mechanics – SMC, Royal Institute of Technology (KTH), SE-100 44 Stockholm Sweden
[2] VTT Technical Research Centre of Finland Ltd, PO Box 1000, FI-02044 VTT, Espoo, Finland
[3] Chalmers University of Technology, Department of Physics, SE-412 96, Göteborg, Sweden
[4] Ringhals AB, SE-43285 Väröbacka, Sweden

Table of contents

1. Introduction

The current trend in the worldwide nuclear power business is to extend the operational life length of the currently existing nuclear power plant fleet. The Nordic countries show no difference from this perspective, where all the existing plants now are slated for operation of at least to 60 years[1]. To prepare for operation beyond the original licensing basis a procedure collectively summarized as Long-Term Operations Preparation, LTO preparation, need to be executed. Many western type reactors follow procedures developed by the IAEA collected in the safety guide SSG-48 (IAEA 2018). These procedures outline the general basis of which programs and procedures that need to exist to establish the requirements for LTO. This is particularly valid in countries that has no specific licence limit, as is the case in Sweden and Finland where the operations are accepted through a periodic safety review and is continuously verified and re-assessed. An important portion of an LTO-program is the surveillance program or the follow-up of the ageing of the reactor pressure vessel material with respect to is assumed and assessed neutron fluence. The surveillance programs have for most been in operation since the start of the reactors and are based on applicable ASTM standards, such as the ASTM e185. The engineering basis here is to assess the shift of the ductile to brittle transition temperature by means of drop-weight or Charpy impact testing.

Recently a technical basis including direct fracture toughness measurements by fracture mechanical tools have been not only codified, ASTM E1921 and ASME Code Case N-830-1 but also assessed for actual use in safety related plant assessments (PWROG 2021) and accepted by the US Nuclear Regulatory Commission. SSM in Sweden has accepted the use in analyses and endorsed the use of the aforementioned Code Case. The next step for the end-users is to fully transition to using fracture mechanical data, in all analyses, also those conducted based on US regulations.

Given the now foreseen long operating periods, there is a imminent need for knowledge retention and transfer. In the Nordic countries this has been clear over the last 10 years or so. The predecessor to RePOUSSES, the NKS, Energiforsk and SAFIR sponsored program “BREDA-RPV” has focussed on the initial collection and testing of the materials harvested from the Barsebäck Reactor Pressure Vessel, RPV (Efsing 2024). Materials harvested from both the core region where the neutron dose is the highest, and from the reactor pressure vessel head, where the dose is the lowest, have been tested and the results show that the thermal ageing portion of the ageing is limited, or non-existent. The objective of RePOUSSES is to collect and analyse the results so far, assess the influence the findings have on the operation of current reactors and also lay a firm basis that existing and future knowledge transfer programs can be based on to assure the availability of correct data and tools as wells a knowledgeable and well trained base of researchers and engineers with deep understanding of the issues connected to RPV ageing.

The results allow for a connection of perspectives ranging from nano to macro sized aspects of the properties of low alloy steels after ageing using a range of assessment tools, from Atom Probe Tomography, APT, to fracture mechanical testing and assessment of the results from a reactor safety perspective. From an end-user perspective, i.e. both the industry and regulators, the data produced extends the knowledge base on the active ageing mechanisms in a vital component for the owners and regulators of nuclear power plants.

[1] https://www.energinyheter.se/20240531/31420/modernisering-av-lovisa-karnkraftverks-lagtryckturbiner-planeras

One foreseen result in this context is to compare the data produced during execution of surveillance programs of the ageing and degradation processes, and the attenuation of radiation effects through the thickness of the pressure vessel wall, with the actual outcome when assessing an actual RPV.

In the 2024 NKS-R program, the participants of the RePOUSSES project have continued the investigations of ageing effects on Reactor pressure vessel steels from the BREDA activity and also started the assessment part. The most recent summary report from NKS-BREDA can be seen in (Efsing et al. 2024).

The key deliverables during RePOUSSES 2024 are the publications from CTH and VTT on the mechanical and microstructural testing of the materials from both the reactor pressure vessel and the surveillance chains, and the study on effects of heterogeneity on fracture initiation in low alloy steels. A further key deliverable was an assessment meeting held at VTT with the stakeholders of the technical question.

The RePOUSSES/BRIGHT program has with the support from NKS, the Finnish national research program SAFER and the Swedish Centre for Nuclear Technology, SKC, been instrumental in the development of a close relationship between VTT, CTH and KTH in the perspective of research on reactor pressure vessel materials. It has been actively pursuing the knowledge retention and knowledge transfer in an important area of reactor safety and has so far, fully or in part, resulted in three successfully completed M. Sc. theses, and 3 Ph. D. theses, with three more Ph. D. theses to be completed in the near future.

2. Microstructural characterization of irradiated and thermally aged material used APT

At Chalmers the post-doc researcher David Mayweg continued to re-examine some of the old samples from the Barsebäck RPV weld material with the new atom probe instrument (LEAP 6000 XR) that they have available. The work in 2024 includes more analysis positions. In previous work CTH did not find any clusters in the low irradiated material, but in the new runs with a more sensitive tool, agglomerates were identified. This was somewhat surprising, as the number of runs performed before should have been enough to find clusters. It can be concluded that the local Ni and Mn concentration has a large effect on the formation of clusters. The observed clusters are similar to the clusters found after high fluence irradiation, the size is slightly smaller, and the chemistry is the same, but the number density is much smaller. The results suggest that clusters do form very early, more or less from the start of irradiation. The results are presented in a paper that was recently accepted in Scripta Materialia, (Mayweg 2025), see appendix.

Figure 1. A large APT dataset from the irradiated Barsebäck weld showing clusters.

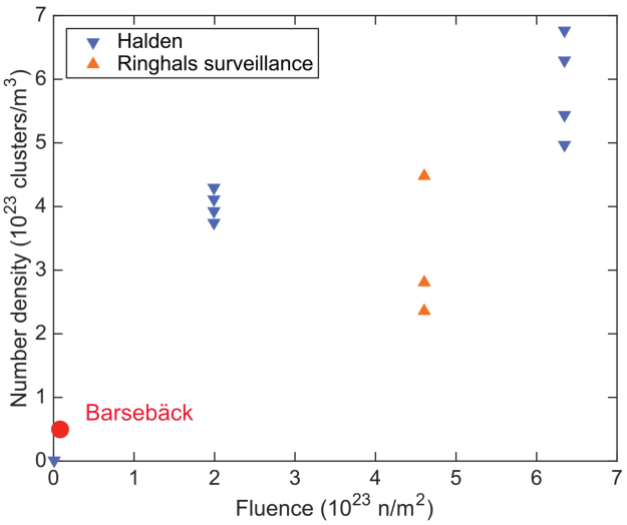

Figure 2. Cluster number density as a function of fluence. The Barsebäck weld is compared with welds irradiated in the Halden Reactor and surveillance samples from Ringhals.

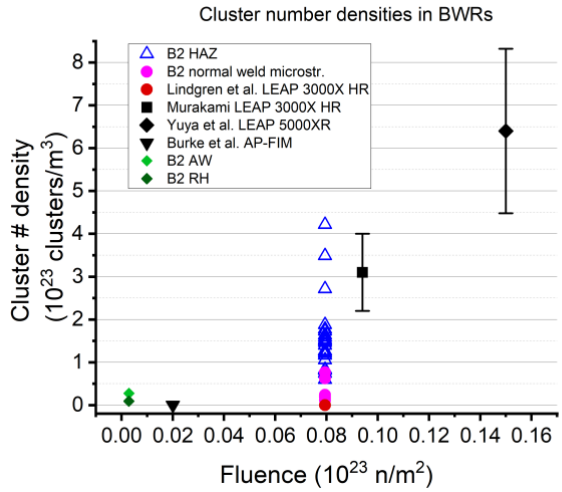

Figure 3. Recent data from the refined assessment of cluster density (Mayweg 2025)

3. Mechanical testing and microstructural characterization at VTT

The SAFER2028 research project BRIGHT (Barsebäck RPV investigation through thickness) investigates the Barsebäck 2 BWR RPV material in irradiated and thermally aged conditions, focusing on the attenuation effect of the base material and advanced microstructural characterization. The NKS project supports the project dissemination to Nordic stakeholders and provides possibility for additional collaboration.

Focus in 2024 has been on fracture mechanical testing of the base material from the beltline region at ¼ thickness, see (Sirkiä et al 2024). Earlier in the year the specimens were machined, however, unexpected challenges in pin-hole drilling were faced which caused some delay in progress. Despite the delay, the planned testing could be fulfilled. Tensile testing included two sets of specimens at different orientations (L and T) and temperatures -100°C, RT, +125°C and +280°C see figure 4. The RPV head shows higher strength compared to the beltline plate. The data presented indicates that there is no effect from thermal ageing on the RPV head, which is consistent with previous findings that exposure of 270°C does not facilitate the necessary driving force to result in either hardening or non-hardening effects on

the material as opposite to the finding from material aged at 345°C where a significant effect is noted.

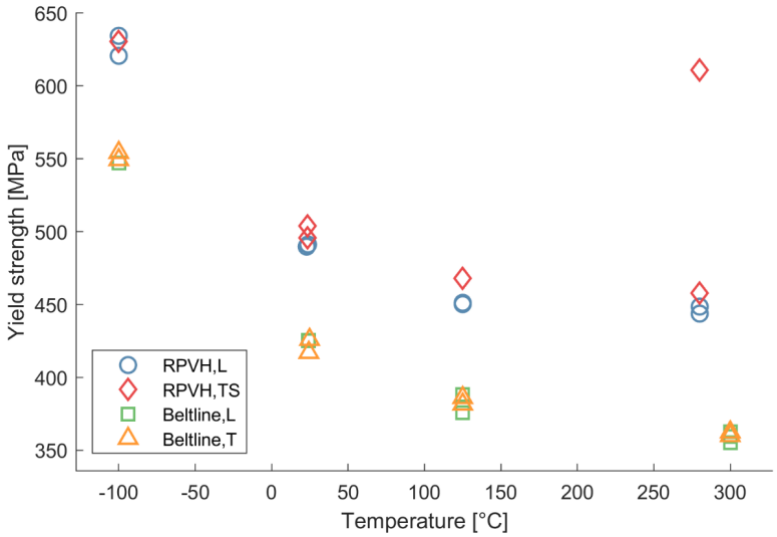

Figure 4, tensile test data from the RPV head and beltline base material at ¼T in different orientations.

The DBTT curve and transition temperature were obtained on Charpy impact toughness testing (L-S) and fracture toughness testing in two orientations (L-S and T-L). The beltline impact toughness resulted at transition temperature of T_{41J}=-26°C, and the fracture toughness testing measured T_0 at -67°C in T-L orientation and -78°C in L-S orientation, see figure 5. The results were compared to the representative surveillance material where the impact results correlate relatively well with a reasonable conservatism when comparing actual data to data from the surveillance programs However, further analysis is needed to fully establish a relationship and formalize any conservatisms.

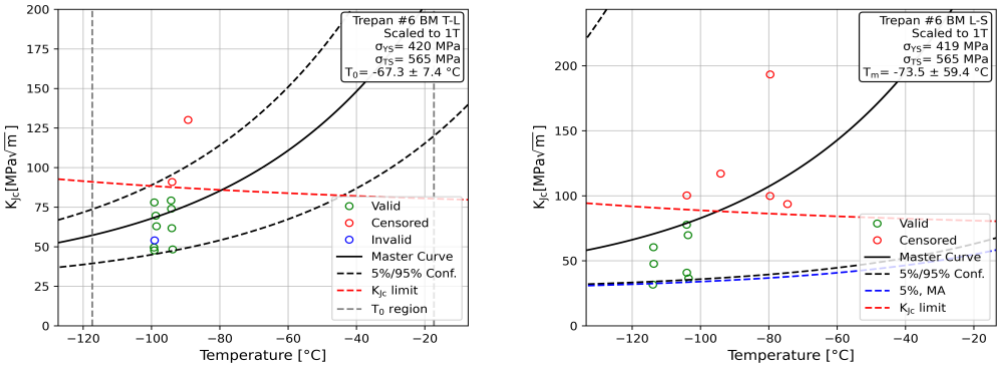

Figure 5, fracture toughness test results of beltline base material at ¼T in T-L and L-S orientation in accordance to ASTM E1921. The objective of the test is to establish the fracture mechanical DBTT, T_0, which is where the average fracture toughness equals 100 MPa√m.

Fractography was performed on all tested brittle specimens, including the impact toughness specimens in the lower transition region and all fracture toughness specimens. The fracture surfaces appeared typical for a base material and in almost all specimens, the primary initiator of cleavage fracture is a Mn-rich carbide. TEM analysis on the second-phase particles at the brittle fracture initiation site was advanced. The previous analyses of the oxide inclusions were further analysed, and one new lamella was produced of a carbide-type initiator. The microstructural characterisations have been presented in various conferences in 2024.

Under the NKS project RePousses, collaboration between VTT and Chalmers realized in APT study at the end of the year. At VTT, samples from the beltline axial weld were extracted using Focused Ion Beam, FIB, technique, and sent to Chalmers for APT analysis. The samples represent four different microstructures of the weld, i.e., acicular ferrite and grain boundary ferrite from the as-welded region and coarser-grained and finer-grained reheated regions. The objective is to find possible differences in elemental clustering based on microstructural features, as within the heterogeneous weld there are local differences in e.g. chemical composition and grain boundaries, which affect the elemental clustering and segregation.

NKS-Repousses seminar was organised at VTT for the collaborators and stakeholders in February, 2024. The discussions and knowledge transfer are an important part of the project and meeting on-site with discussions and presentations is invaluable for the project group.

4. Modelling of fracture properties

AT KTH the modelling work continues to progress, and so do the testing that is being performed on thermally aged material from Ringhals. The current work is an expansion of the previous modelling effort by (Boåsen et al, 2021), where also a heterogeneity in fracture toughness is fully accounted for. For example, such heterogeneity may be found in welds where the fracture toughness can differ significantly. A study addressing this topic has been published in the open literature, (Klein and Faleskog 2023). An extended proposed methodology is in the process of acceptance in the open literature which is based on the fact that the inhomogeneity of the weld in parts is caused by the occurrence of several different zones of material with very different behaviors, i.e. reheated weld material with small equi-axed grains, and elongated columnar grains stemming from the solidification process of the weld but where the strength of the individual grain depends if a crack is located parallel to the dendrites or in an angle.

Based on this notion, the experiments carried out on the aged Ringhals unit 4 pressurizer material were revisited and an extensive fractography study using SEM imaging of the fracture surfaces and etching of cross-sections was done to determine in which type of weld zone the crack front in each specimen was located in. It was observed that a crack front in the as-welded zone with elongated grains parallel to the crack plane led to failure along the grain boundaries and low toughness. The toughness was significantly increased if the axis of grain elongation was sufficiently inclined compared to the crack plane. In specimens with crack fronts located in the reheated zone with equiaxed grains, exhibited a toughness in between the extremes found in the as-welded zone. Thus, the fracture toughness in specimens that failed along grain boundaries were typically lower than that observed in specimens that failed by transgranular cleavage. This means that the bimodality observed in the cumulative probability of failure in some of the test series stems from heterogeneity which may be reinforced by intergranular failure by phosphorous segregation. For the purpose of extending the knowledge, extensive fracture mechanical testing has been executed. Some portions still remain for the activity in 2025 before reporting can be relevant. However, both students using the results for their planned defense of their respective Ph. D. theses during 2025.

5. Conclusions

Samples have been extracted from the RPV of Barsebäck Unit 2 and shipped to VTT. Mechanical testing of the material indicates that the influence of thermal ageing on the measurable sizes is very small. The theory based on microstructural grain features affecting

the failure probability and behavior have been further extended and will be reported in full in 2025.

Results from the mechanical testing is starting to become available thus allowing for initial assessments of the resulting changes in the properties. This work is foreseen to be extended in 2025 with expanded collaboration between the executing partners and the industrial and regulatory partners.

Studies on the BWR irradiated materials have previously shown few or no signs of agglomerates as have been evident in the higher dose materials previously investigated. However, a re-examination of the data shows signs of clustering of Ni that may be the precursors of agglomeration.

6. References

Boåsen M. et al, 2021, A weakest link model for multiple mechanism brittle fracture – Model development and application, In *J of the Mechanics and Physics of Solids*, vol. 147, paper Id 104224, https://doi.org/10.1016/j.jmps.2020.104224

Efsing P et al, 2024 Barsebäck as research and development platform, extraction and analysis of reactor pressure vessel material, NKS-486, ISBN: 978-87-7893-582-3

IAEA, 2018, Ageing management and development of a programme for long term operation of nuclear power plants, International Atomic Energy Agency, Vienna, ISSN 1020-525X, ISBN 978-92-0-104318-4.

Klein and Faleskog, 2023, Influence of heterogeneity due to toughness variations on weakest-link modeling for brittle failure, Engineering Fracture Mechanics 292 (2023) 109643, https://doi.org/10.1016/j.engfracmech.2023.109643

Lindkvist et al., 2023, Mechanical behaviour of high-Ni/high-Mn Barsebäck 2 reactor pressure vessel welds after 28 years of operation, Journal of Nuclear Materials, vol 581, paper id 154447

Mayweg, et. al., 2025, Irradiation-induced clustering in a high-Ni, high-Mn, low-Cu boiling water reactor pressure vessel weld after 28 full power years, Scripta Mater. 258, paper id 116497

PWROG-18086-NP, rev. 1, 2021, Use of direct fracture toughness for evaluation of RPV integrity, Brian Hall et. al. https://www.nrc.gov/docs/ML2406/ML24068A103.pdf

Sirkiä et al., 2024, On comparison of fracture toughness of irradiated and thermally aged decommissioned nuclear weld materials with miniature specimen test technique, Theoretical and applied fracture mechanics, vol 133, Paper Id 104598

body supporting NKS activities can be held responsible for the material presented in this report.

Acknowledgements

NKS conveys its gratitude to all organizations and persons who by means of financial support or contributions in kind have made the work presented in this report possible.

The support from the Finnish nuclear safety program, the SAFER2028-program, the Swedish Radiation Safety Authority and the Swedish Centre for Nuclear Technology, SKC as well as the Swedish Nuclear Power Plants permit holders and owners (Ringhals AB, Forsmarks Kraftgrupp AB, OKG AB, Vattenfall AB, Fortum and Uniper) for the work is gratefully acknowledged.

Appendices

1. D. Mayweg, K. Lindgren, J. Roudén, J. Blomström, P. Efsing and M. Thuvander, Irradiation-induced clustering in a high-Ni, high-Mn, low-Cu boiling water reactor pressure vessel weld after 28 full power years, *Scripta Mater*. 258 (2025) 116497

2. Hytönen, N., Lindqvist, S., Lydman, J., Ge, Y., Que, Z., Efsing, P. 2025. Microscopic characterisation of brittle fracture initiation in irradiated and thermally aged low-alloy steel welds of a decommissioned reactor pressure vessel. *Journal of Nuclear Materials*, volume 603, 155423.

3. Sirkiä, L., Suman, S., Arffman, P., Hytönen, N., Virkkunen, I. 2024. On comparison of fracture toughness of irradiated and thermally aged decommissioned nuclear weld metals with miniature specimen test technique. *Theoretical and Applied Fracture Mechanics*, volume 133, B, 104598.

4. Ferreiros P., Hytönen N., Lydman J., Ge, Y., Que Z., Efsing P., Advanced characterization of inclusions acting as brittle fracture initiators of miniature compact tension C(T) specimens from RPV welds of a decommissioned boiling water reactor, Presented at the NuMat conference 2024.

Bibliographic Data Sheet **NKS-497**

Title	Reactor Pressure Vessel LTO Assessment
Author(s)	Pål Efsing[1,4], Jonas Faleskog[1], Daniela Klein1 Noora Hytönen[2], Sebastian Lindqvist[2] Mattias Thuvander[3], David Mayweg[3] Johan Blomström[4]
Affiliation(s)	[1] Department of Solid Mechanics, Royal Institute of Technology (KTH), SE-10044 Stockholm Sweden [2] VTT Technical Research Centre of Finland Ltd, PO Box 1000, FI-02044 VTT, Helsinki, Finland [3] Chalmers University of Technology, Department of Physics, SE-41296, Göteborg, Sweden [4] Ringhals AB, SE-43285 Väröbacka, Sweden
ISBN	978-87-7893-595-3
Date	March 2025
Project	NKS-R / RePOUSSES 2024 activity (Contract: AFT/NKS-R(24)142/8)
No. of pages	9
No. of tables	0
No. of illustrations	5
No. of references	8
Abstract max. 2000 characters	As part of the NKS-R program, VTT, Chalmers University of Technology and KTH have extended the assessment of micro-structural and mechanical property evolution during irradiation to analyze the as-aged material properties of the retired reactor pressure vessel, RPV, from Barsebäck unit 2. The testing has included impact and fracture mechanical testing of material, as well as high and low magnification microstructural characterization of the weld metal from the reactor pressure vessel using LOM, SEM and APT. Due to the nature of the work, the NKS-project is connected to several adjacent activities, including support from the Finnish Nuclear Safety Program, the SAFIR-program, the Swedish Radiation Safety Authority SSM and Swedish Centre for Nuclear Technology, and SKC.
Key words	Low alloy steel, irradiation effects, fracture toughness, ductile to brittle transition temperature, constraint effects, high resolution microscopy, microstructural characterization

Theoretical and Applied Fracture Mechanics 133 (2024) 104598

Contents lists available at ScienceDirect

Theoretical and Applied Fracture Mechanics

journal homepage: www.elsevier.com/locate/tafmec

On comparison of fracture toughness of irradiated and thermally aged decommissioned nuclear weld metals with miniature specimen test technique

Laura Sirkiä [a,*], Siddharth Suman [a], Pentti Arffman [a], Noora Hytönen [a], Iikka Virkkunen [b]

[a] Nuclear Safety, VTT Technical Research Centre of Finland, Kivimiehentie 3, 02150 Espoo, Finland
[b] Department of Mechanical Engineering, Aalto University, Puumiehenkuja 3, 02150 Espoo, Finland

ARTICLE INFO

Keywords:
Nuclear materials
Fracture toughness
Miniature specimen testing
Miniature C(T) specimen
Experimental research

ABSTRACT

This paper investigates the fracture toughness of thermally aged and irradiated weld metals extracted from head and beltline regions of a decommissioned nuclear reactor pressure vessel. Miniature compact tension specimens are fabricated from the thermally aged reactor pressure vessel head weld as well from the circumferential and axial beltline welds having fluences of 2.90×10^{16}n/cm^2 and 7.94×10^{17}n/cm^2, respectively. Master curve approach in accordance with the ASTM E1921 is applied to determine the reference temperature T_0 and it is found to be − 113.5 °C, −104.4 °C, and − 89.3 °C for the reactor pressure vessel head, axial beltline, and circumferential beltline welds, respectively. In addition, the multimodal reference temperature T_m to assess the homogeneity of welds as well as key curve analysis for the quality assurance of testing are also provided. Fractographic analysis identified variations in crack initiation sites and microstructural inhomogeneities, particularly in the irradiated beltline welds. Overall, fracture mechanical testing of the materials demonstrated that miniature compact tension specimens are effective for characterizing the fracture toughness of limited surveillance weld materials, revealing differences due to irradiation and weld location.

1. Introduction

Long term operation (LTO) is an area of interest for many nuclear power plants (NPPs) as the initially planned lifetimes of many NPPs are approaching their end-of-life. In order to monitor the structural integrity of one of the most critical components of the NPPs, reactor pressure vessel (RPV) surveillance programs have been established. Fracture toughness assessment in these programs is traditionally based on impact testing on $10 \times 10 \times 55$ mm^3 Charpy V-Notch (CVN) specimens. The tests only serve as an indirect means of assessment. Due to the extending lifetime of the plants, the available volume of the RPV surveillance specimens constantly decreases. Therefore, the applicability of miniature specimen test techniques requires validation, specifically in the hot cell environment with irradiated materials. Furthermore, the utilization of contemporary fracture mechanics testing methods allows direct fracture toughness assessment. This is a significant improvement in understanding actual material behavior and corresponding confidence levels for safety. However, introduction of new methodology requires additional tests and thus miniaturized specimens.

The fabrication and fracture mechanics testing methods of miniature compact tension (C(T)) specimens manufactured from irradiated, as well as non-irradiated, RPV steel have been studied and found to be very promising by means of determination of the reference temperature, T_0, in several studies. Naziris et al. [1] presented an in-cell manufacturing method of a miniature C(T) specimen from a tested CVN sample. The study by Cicero et al. [2] summarized a wide range of advantages and possibilities when using miniature C(T) specimens in the RPV steel investigations. These advantages included the reuse of tested CVN specimens and possibilities to measure local characteristics, like toughness to detect heterogeneities and toughness gradients from, e.g., welds. A valid reference temperature T_0 and fracture toughness were obtained successfully from irradiated miniature C(T) specimens by Ha et al. [3] and Sugihara et al. [4]. Research on irradiated Japanese RPV steel showed that the results from miniature C(T) specimens compare favorably with the Japanese surveillance database. Fracture toughness tests with miniature C(T) specimens on irradiated and unirradiated conditions were conducted in the ductile–brittle transition region as well as in the upper shelf regime by Lambrecht et al. [5]. A valid reference

* Corresponding author at: Nuclear Safety, VTT Technical Research Centre of Finland, Kivimiehentie 3, 02150 Espoo, Finland.
E-mail address: laura.sirkia@vtt.fi (L. Sirkiä).

https://doi.org/10.1016/j.tafmec.2024.104598
Received 29 December 2023; Received in revised form 19 June 2024; Accepted 22 July 2024
Available online 23 July 2024

temperature T_0 was obtained in the transition region for both unirradiated and irradiated materials. Three different analysis methods (normalization model, normalization method, and unloading compliance) were used in the upper shelf regime for miniature C(T) specimen testing at two different test temperatures, +20 °C and + 290 °C. All analysis methods yielded comparable results except at + 20 °C for unirradiated material.

The same material, weld metal from the RPV of Barsebäck 2 characterized in this research, was investigated by Arffman et al. [6] through tests with mini tensile, miniature C(T) and CVN specimens. The results offered a standpoint of the mechanical and fracture mechanical properties. Irradiated and unirradiated JRQ and JFL materials were investigated successfully with miniature C(T) specimens by Das et al. [7]. The reference temperature T_0 determined with standard size Charpy specimens was successfully validated with miniature C(T) specimens.

Due to its size, the RPV contains several welds, and the fact that any discontinuities can make the material more susceptible to degradation and failure, drives the need to monitor the integrity of weldments. Zerbst et al. [8] have compiled an overview of fracture and crack propagation studies in weld metal, in which the microstructure is highly inhomogeneous [9], and one notable matter is that welds consist of many layers of different microstructures. Considering this, miniaturized test specimens are an excellent configuration since their size enables the crack to propagate in a single microstructure within the weld material.

The RPV has two main orientations for welds. This was taken into account in this study, and test specimens from both circumferentially and axially orientated welds were prepared together with test specimens from the RPV head (RPVH) weld. Additionally, an overview of the fractographic characterization of the RPVH and core region welds is presented considering the material inhomogeneities, and their potential effect on the reference temperature T_0.

2. Materials and methods

2.1. Characteristics of studied materials

The studied materials were harvested from a decommissioned NPP of Barsebäck 2 after 28 years of operation. An RPVH weld metal and two different welds taken from the beltline region in the axial and circumferential orientation were investigated. Despite being in an NPP for 28 years, the RPVH weld is classified as thermally aged but non-irradiated material, while the beltline welds represent irradiated material. The neutron fluence is approximately 2.9×10^{16}n/cm^2 for the circumferentially orientated beltline weld and 7.94×10^{17}n/cm^2 for the axially orientated beltline weld. The RPV was manufactured from a plate material SA 533 Gr. B Class 1 and welded together using submerged arc welding with a weld filler metal S3NiMo. This filler type is a high-Mn-Ni and low-Cu weld material. The same welding procedure was used for all welding seams. The RPV was exposed to a post weld heat treatment at the manufacturing stage.

According to prior conducted tensile tests, yield strength ($R_{p0.2}$) and tensile strength (UTS) were 562 MPa and 628 MPa for the RPVH weld metal, 510 MPa and 573 MPa for the axially orientated beltline weld, and 580 MPa and 639 MPa for the circumferentially orientated beltline weld, respectively. The chemical composition of the studied materials is presented in Table 1. A schematic drawing of the studied RPV, the location of the welds and trepans, and the operating temperatures are presented in Fig. 1. The operational pressure was 7 MPa. However, the pressure loads and thermal stresses under plant operation have no effect on the fracture toughness of the RPV.

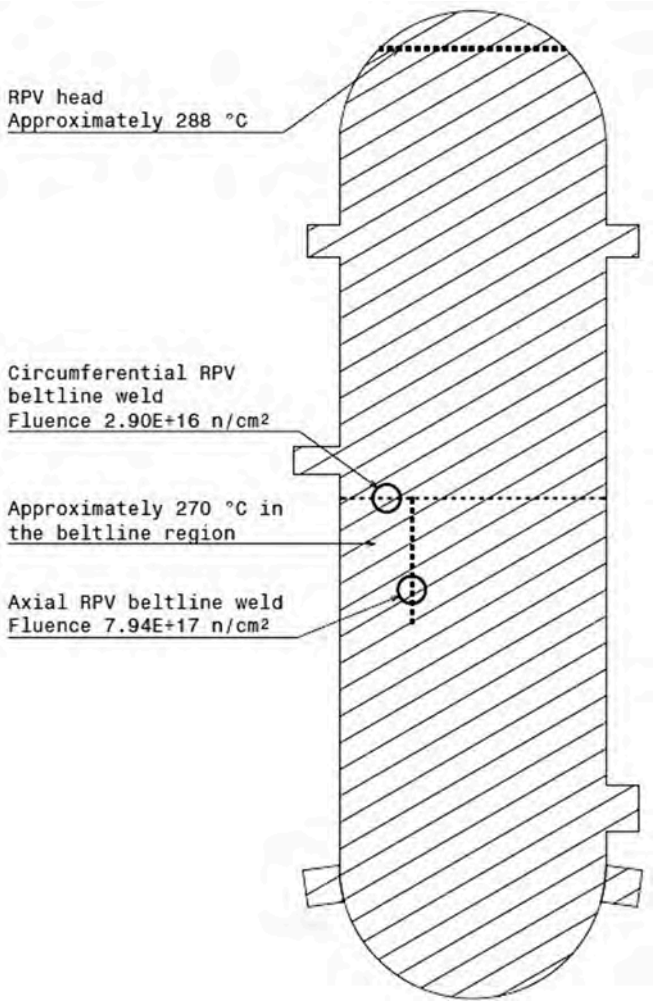

Fig. 1. Schematic drawing of the Barsebäck 2 RPV, extraction locations of the samples, including fluences and approximate temperatures.

2.2. Test specimens

The test specimens were manufactured from CVN halves (see Fig. 2a) by electric discharge machine (EDM) in a Hot Cell laboratory. The specimens were weld metal in full. The use of tested CVN halves to manufacture miniature C(T) specimens emphasizes the re-use aspect of surveillance specimens. Since the research project began, the standard methodology and methods have advanced, and consequently, the specimen geometry is slightly different between the RPVH and beltline tests. A crack open displacement (COD) measurement from the load line is considered advantageous in the hot cell environment in terms of handling. In order to manage possible challenges in the load line COD measurement, the beltline specimens were designed with seats for both types of COD gauges (see Fig. 2b). The pre-fatigue process with the load line COD gauge proved unreliable and the measurement was switched

Table 1
The chemical compositions (wt %) of the studied materials according to the manufacturer's reference and the OES measurements.

	Mn	Ni	Mo	Si	Cr	C	Cu	P	Co	S
RPVH	1.43	1.47	0.41	0.15	0.03	0.057	0.060	0.008	0.020	0.007
Axial beltline weld	1.47	1.65	0.43	0.16	0.03	0.054	0.068	0.010	0.018	0.005
Circumferential beltline weld	1.42	1.66	0.43	0.16	0.03	0.064	0.085	0.008	0.018	0.005

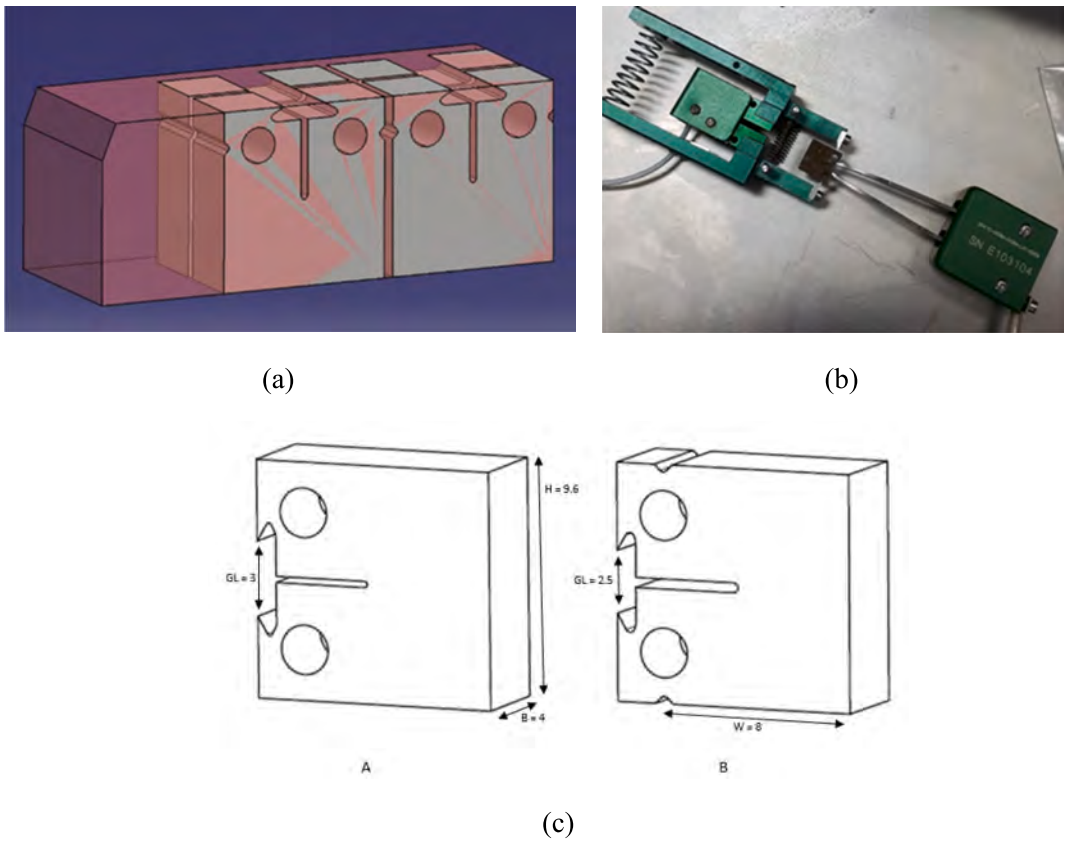

Fig. 2. A) extraction of miniature c(t) specimens from a cvn halve, b) cod gauge attached to the load line and the front face of the specimen, c) used specimens; front face cod on the left, and specimen with places for both cod gauges on the right (with main dimensions: H=height, B=thickness, W=width, and GL = gauge length).

back to the front face COD gauge. However, the COD during the beltline specimen tests was measured from the load line.

The RPVH material consisted of 20 specimens, using the configuration (specimen A) shown in Fig. 2c, with an option for the front face COD gauge only. The beltline weld test series, 15 specimens for both orientations, were manufactured according to the configuration (specimen B) shown in Fig. 2c. The beltline specimens had locations for both COD gauges, load line and front face (see Fig. 2b). The main dimensions of all specimens were height H=9.6 mm, width W=8 mm, and thickness B=4 mm. The gauge length of the front face COD (COD_{FF}) gauge in the RPVH specimens was 3 mm, and in the beltline weld specimens, was 2.5 mm (see Fig. 2c). The gauge length for the external load line COD (COD_{LL}) gauge was 9 mm in the beltline weld specimens. The used COD gauges are both custom-made. The COD_{FF} gauge has a travel range from − 1 mm to + 4 mm, the gauge length is 3 mm, and it has narrowed shafts. The COD_{LL} gauge has the travel range of 3 mm and 9 mm of the gauge length.

The manufacturing of the specimens was planned according to the general surveillance standard ASTM E185-16 [10] with one exception; the standard recommends T-L as for the specimen orientation, but since the orientation has been T-S in earlier surveillance tests, this orientation was kept. The specimens were not side grooved. The test matrix is presented in Table 2.

Table 2
A test matrix of the studied materials.

Material	Series [pc]	Test temperature [°C]	Orientation
RPVH	20	−130 – −120	T-S
Axial beltline weld	15	−146 – −115	T-S
Circumferential beltline weld	15	−146 – −120	T-S

2.3. Fracture mechanics testing procedure

In the fracture mechanics testing arrangements, the ASTM standard E1921-20 [11] was followed, which gives the basis for reference temperature, T_0, determination for ferritic steels. The initial procedure involves pre-fatigue of the test specimens, targeting to an a/W (pre-fatigued crack length/width) ratio of 0.45–0.55. Pre-fatigue was carried out with a servo hydraulic material testing machine for a frequency range between 10 Hz and 20 Hz via load control and keeping the ΔK under 15 MPa$\sqrt{m}$ as per the standard recommendations. The material testing machine was operated in a 10 kN load region and the COD_{FF} gauge was used to monitor the crack length and the pre-fatigue procedure. The actual testing was also conducted using the 10 kN load region, but with an electric material testing machine and inside an environmental chamber, which enables the use of liquid nitrogen to achieve the desired test temperature. In the beltline specimens testing, the COD_{LL} was used to monitor the crack propagation and the COD_{FF} was used for the RPVH specimens testing. During the testing, specimens were loaded with a loading rate of 0.3 mm/min at a quasi-static rate, with displacement control up to at least 20 % of a load drop or until fully fractured. As a post-test treatment, specimens that were not fully fractured, were broken in half by using liquid nitrogen and fracture surfaces were imaged with a stereo microscope. Finally, the initial crack lengths were measured according to the standard nine-point average procedure.

2.3.1. Homogeneity screening

In addition to the regular, homogeneous reference temperature determination, the test series' analyses included the homogeneity screening as well as bimodal and multimodal inhomogeneity assessment procedures. These procedures are included in the ASTM standard E1921.

The homogeneity screening procedure is based on the SINTAP lower-tail analysis method [12]. The lower-tail estimate is determined by

censoring the tests with fracture toughness higher than the median curve and calculating a new reference temperature for this dataset. This is repeated until the reference temperature does not change. Finally, the material is regarded as inhomogeneous, if the difference between the standard Master Curve T_0 value and the lower-tail estimate is larger than approximately 10 %.

In multimodal and bimodal evaluations, either two discrete or a normal distribution of Master Curves with distinct probabilities are determined for the test series. These evaluations provide their own confidences of correct identification, defined by measures of likelihood and corresponding limits [13]. While the ASTM standard E1921 advises the utilization of bimodal and multimodal assessments only for series with at least 20 tests, Wallin [14] demonstrated that the multimodal methodology can be used for all complete test series cases, given that an additional margin adjustment is included. The bimodal evaluation, however, is inconsistent for small datasets.

2.3.2. *Key curve – analysis*

The Key Curve – analysis is a quality assurance-based method to observe specimen to specimen variation in a test series. The load normalized by the limit load (P/P_L) is portrayed as a function of crack normalized by the specimen's width ($\Delta c/W$). The test end values were used in the analysis. Wallin [15] states that typical errors in fracture mechanics experiments are due to the measurements of crack length, displacement, and possible even load. Moreover, if specimen to specimen variation is large, it is mainly due to the errors or uncertainties in measurements of the crack length. These would most likely be seen as data points falling outside the scatter bands.

2.4. *Fractographical characterization*

Fractographical characterization was performed to investigate the primary initiation site of the brittle fracture for features affecting the crack initiation, and to see whether the primary initiation region has differences between as thermally aged RPVH weld and the irradiated core region welds. The fracture surfaces were examined using a Zeiss 540 Cross Beam with a field emission gun-scanning electron microscope (FEG-SEM) that has magnification range between 50 × and 15 000 × and uses acceleration voltage between 5 kV and 15 kV.

A more specific characterization of the brittle fracture initiation and microstructure of the studied RPVH weld metal was done by Que et al. [16], and together with the aid of an axially orientated beltline weld by Hytönen et al. [17].

3. Results and Discussion

3.1. *Reference temperature (T_0)*

Representative force-crack opening displacement curve of all the three RPV welds having a/W ratio of 0.48 and test temperature of −120 °C is shown in Fig. 3. Reference temperature, T_0, multimodal reference temperature, T_m, and the quality assurance-based Key Curve of studied materials are presented in Table 3 and Figs. 4–6. Additionally, for comparison, the reference temperature estimation of full-size Charpy V-Notch (CVN) specimens is presented in Table 3. The reference temperature estimation $T_{0est.}$ based on CVN impact toughness transition temperature corresponding to T_{28J} is also performed and provided in Table 3. This concept is presented by Wallin [15] when he describes the indirect fracture toughness estimation methods. The thermally aged RPVH weld passed, although barely, the inhomogeneity screening of the ASTM standard E1921 [12] and can be considered to represent macroscopically homogeneous material. Thus, T_0 and T_m are practically the same for the RPVH material.

There is more difference between the T_0 and T_m of axially and circumferentially orientated beltline welds. The difference, however, is quite small in the axially orientated beltline weld region, which would

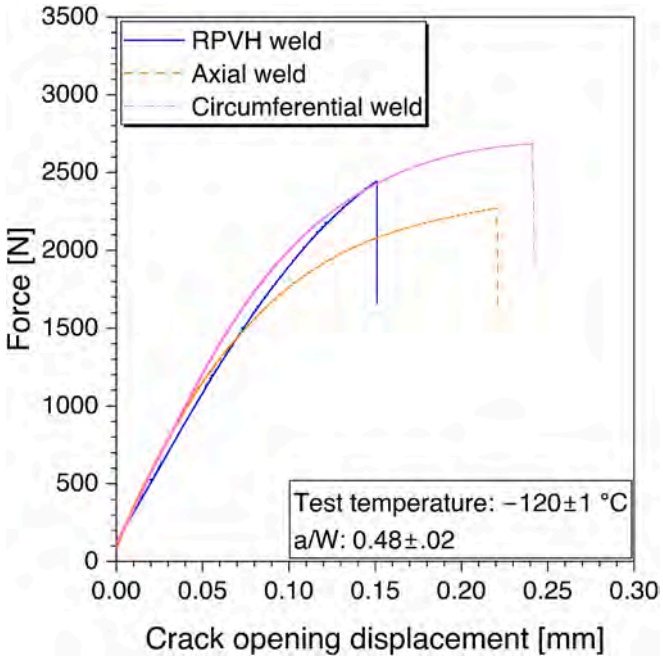

Fig. 3. Illustration of force – crack opening displacement curves from all three different investigated welds for similar test temperature and a/W ratio.

indicate that there is less inhomogeneity there than in the circumferentially orientated beltline weld region. Also, based on the reference temperature, the circumferentially orientated beltline weld region seems to be the most brittle one although its location is further from the center of the core and despite the lower amount of irradiation than the axially orientated beltline weld region. The miniature C(T) specimen results show that the lowest reference temperature was in the RPVH weld region. All results presented in Table 3 fit into the margin of error while the trend is slightly different and opposite between the results obtained with miniature C(T) specimens and full-size CVN specimens. Nevertheless, the margin of error is lower in T_0 values obtained with the miniature C(T) specimens.

The study by May et al. [18] focused on Ringhals NPP unit 3 and unit 4 RPV materials. Discussion can be found whether the manufacturing conditions have an influence for irradiation response and differences of T_0 values in an unirradiated condition. The R3 and R4 materials used in the study by May et al. have very similar chemical compositions as the materials investigated in this study (see Table 1), and thus it is unlikely that the chemical composition is a variable behind the T_0 value differences found in this study.

Unlike T_0, which is the lowest for homogeneous thermally aged head weld, $T_{0est.}$ is lowest for the inhomogeneous irradiated axial beltline weld. It implicates that indirect fracture toughness estimation based on empirical correlation shall be cautiously used. Even Wallin [15] has found that arc weld metals were clear outliers to this empirical correlation, and these results further corroborate this observation. One conjecture for such behavior for irradiated weld metals can be the insensitiveness of the Charpy impact test to local brittle zones.

While the surveillance program did not include direct experimental fracture toughness research during the plant lifetime, the investigations in this research illustrate the necessity of direct fracture mechanical assessment to study the integrity of the RPV. Furthermore, the local phenomena in the embrittlement are best observed with miniature specimens, which also help with the limited volume of the surveillance material, and particularly that of the welds.

3.1.1. *Inhomogeneity assessment*

This study applied two methods to assess the inhomogeneity of the

Table 3
T_0 results of studied materials.

Material	Fluence [n/cm^2]	T_0 [°C]	*Screening criterion*	$T_{m\ multimodal}$ [°C]	MLNH	CVN $T_{0est.}$ [°C]
RPVH weld	0	−113.5 ± 6.6	Homogeneous	−112.9 ± 39.3	6.83	−103 ± 18
Axial beltline weld	7.94 × 10^{17}	−104.4 ± 6.7	Inhomogeneous	−99.5 ± 17.6	2.60	−124 ± 18
Circumferential beltline weld	2.90 × 10^{16}	−89.3 ± 7.8	Inhomogeneous	−77.9 ± 31.9	4.09	−95 ± 18

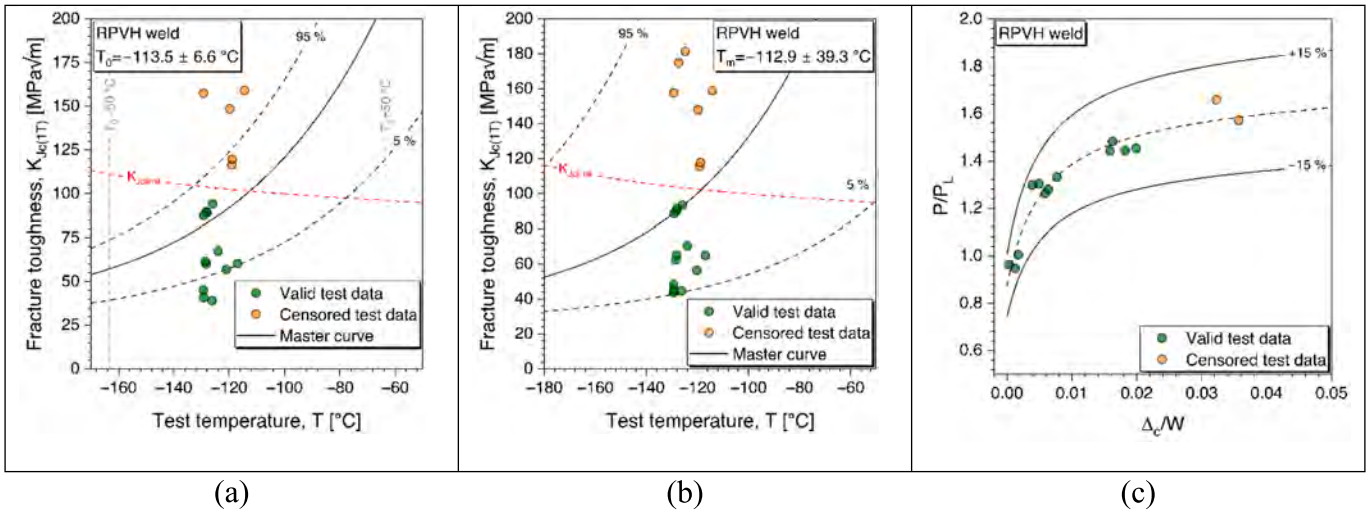

Fig. 4. T_0 (a), multimodal T_m (b), and Key Curve (c) of the RPVH weld.

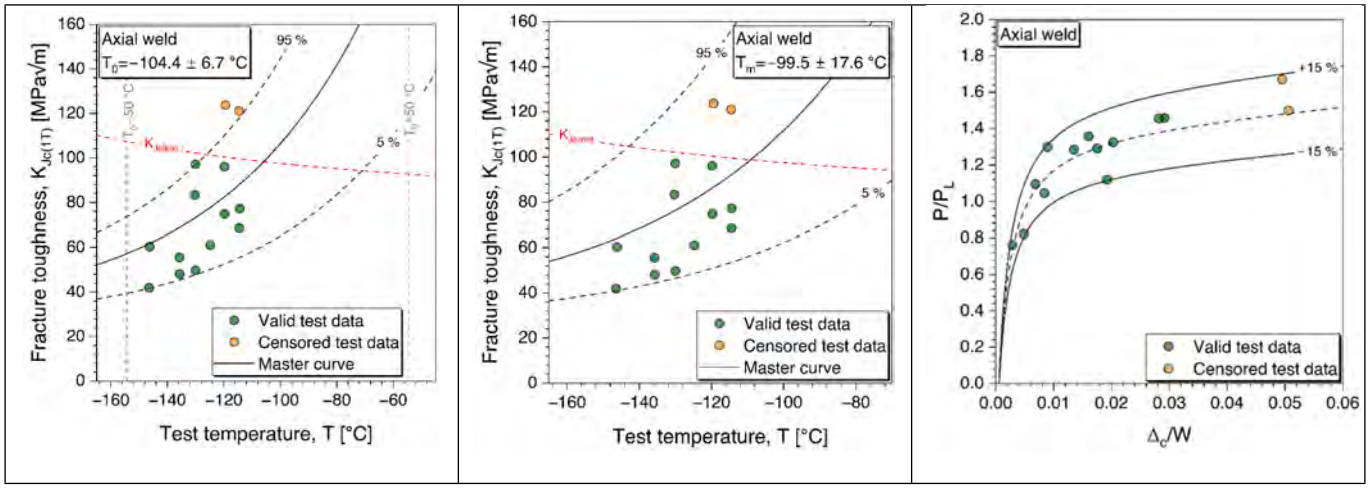

Fig. 5. T_0 (a), multimodal T_m (b), and Key Curve (c) of the axially orientated beltline weld.

investigated weld materials: the SINTAP-based screening procedure, and the multimodal master curve approach. While both beltline weld materials failed the initial SINTAP screening for homogeneity, the RPVH weld material passed narrowly. Interestingly, the RPVH material exhibited a larger deviation in its multimodal master curve screening compared to the beltline materials that have an MLNH of 6.83 with a 98.2 % confidence level in its identification. Based on these observations, it is recommended that multimodal evaluation be implemented for all datasets, regardless of the SINTAP screening results, to ensure a better-informed identification of potential inhomogeneity. Furthermore, the analysis of the multimodal master curve deviations revealed a significantly smaller deviation for the axially oriented beltline weld compared to the other materials, indicating a lower level of inhomogeneity. Also, the multimodal reference temperature was higher in the circumferential weld compared to the axial weld. While the wide confidence bounds associated with these values suggest that the materials potentially originate from the same distribution and may render any conclusive rationale solely based on T_m in a position of not being appropriate.

3.2. Initiation sites and inclusion morphology

The fractographical characterization was performed for all tested brittle miniature C(T) specimens to investigate the features in the primary initiation site area. The primary initiation sites were identified by following the river patterns typical for cleavage fracture; see Fig. 7a, 8a,

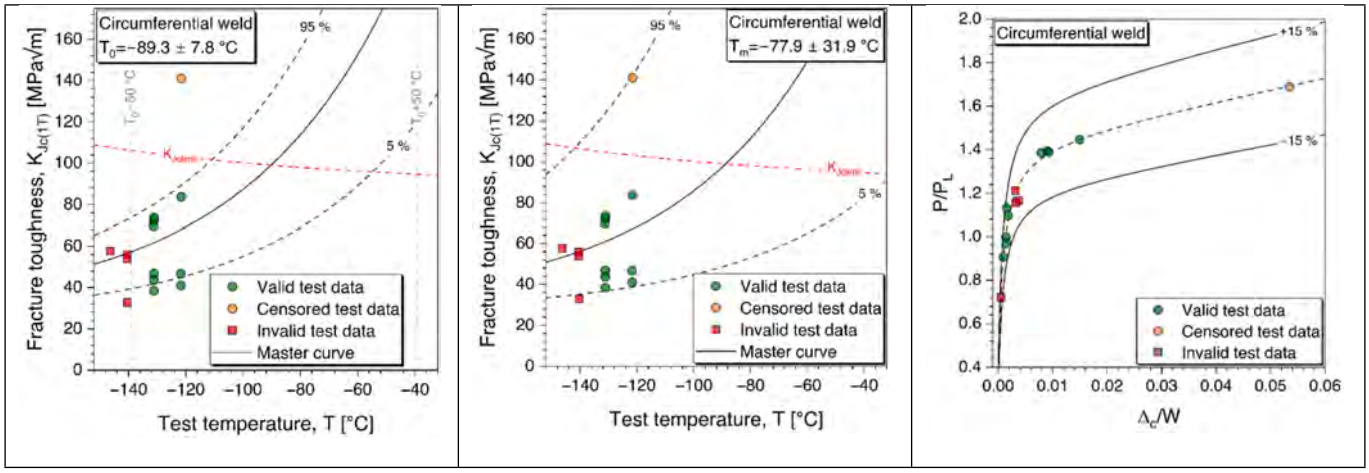

Fig. 6. T_0 (a), multimodal T_m (b), and Key Curve (c) of the circumferentially orientated beltline weld.

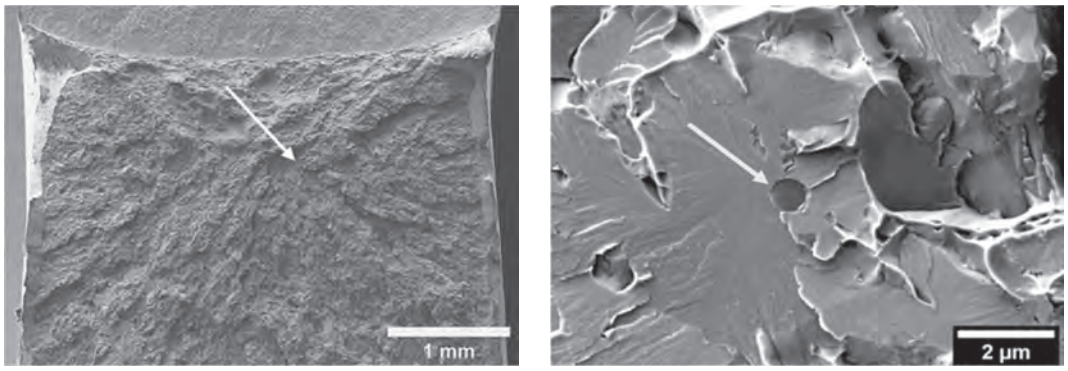

Fig. 7. A) fracture surface and b) nucleating particle of the rpvh weld miniature c(t) specimen.

and 9a. The main fracture type was cleavage fracture in all specimens, although in some irradiated specimens, minor areas of intergranular cracking were found near the initiation site. For most specimens, the fracture occurred in the center of the fracture surface.

It was observed that the brittle fracture initiation site always involves an inclusion. Two types of inclusions at the primary initiation site have been observed. In all specimens of the RPVH weld (see Fig. 7), the inclusion at the initiation was a nonmetallic roundish oxide with a diameter of approximately 0.3 µm –1.8 µm. The initiation site in the circumferentially orientated beltline weld (see Fig. 8) was relatively similar to the RPVH. In the axially orientated beltline weld (see Fig. 9), almost all of the inclusions at the initiation sites were irregularly shaped inclusions and only two of the typical oxide-type. The actual size of the irregularly shaped inclusions was challenging to determine, but the estimated size is approximately 1 µm –2 µm.

In Figs. 7–9, typical primary initiation sites are shown for the

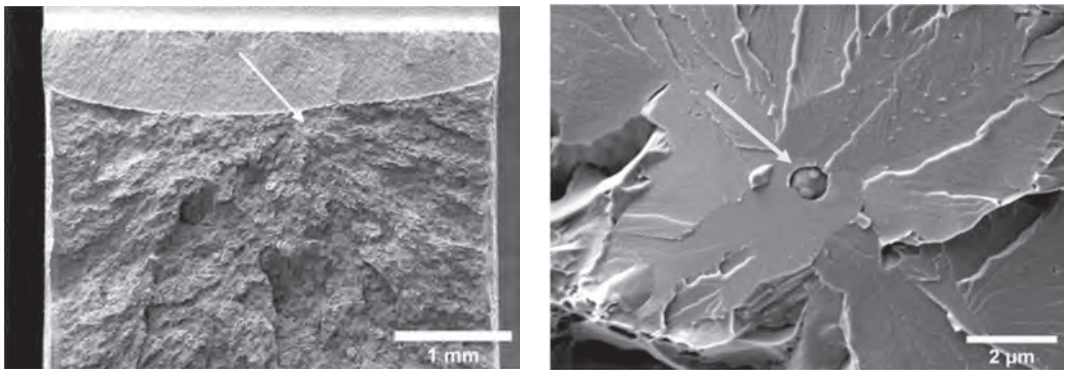

Fig. 8. A) fracture surface and b) nucleating particle of the circumferentially orientated beltline weld miniature c(t) specimen.

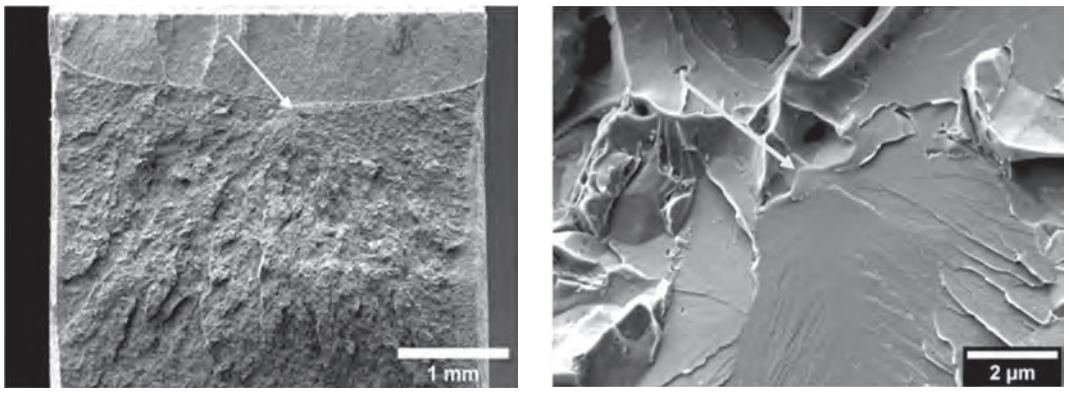

Fig. 9. A) fracture surface and b) nucleating particle of the axially orientated beltline weld miniature C(T) specimen.

investigated RPV welds. An arrow points to the primary initiation site (a) and the inclusion at the initiation site (b). In Fig. 7, the roundish oxide inclusion is broken in half, and the other half can be found on the mating fracture surface. It is assumed that in this type of case, the crack has initiated within the relatively large brittle inclusion and propagated through the weld matrix. In Fig. 8, the oxide inclusion is intact but slightly debonded from the metal matrix, indicating that the brittle fracture has initiated at the interface between the inclusion and the weld matrix.

In Fig. 9, the inclusion morphology and the initiation site are different from those in Figs. 7 and 8. The inclusion is irregularly shaped and more difficult to distinguish from the matrix. The inclusion is most likely at a grain boundary and cleavage fracture propagates only to one side of the inclusion. The inclusion is also broken, but it is also debonded from the matrix on the side opposite the cleavage fracture, hence it is unsure whether the crack initiates primarily within the inclusion or at the interface. Additionally, slightly more plastic deformation can be observed in the surroundings of this type of inclusion initiation site indicating that the oxide inclusions retain less toughness than the irregularly shaped metallic inclusions.

Some correlations between the inclusion size and impact toughness were observed for the RPVH weld [19], but a linear correlation for the fracture toughness testing has not been made. This may be an indication of the inhomogeneity of the material and result from testing inhomogeneous weld metal with miniature C(T) specimens. Comparing the homogeneity of the primary initiation site and mechanical testing results, the observations depend on the perspective. Regarding the initiation site's appearance and inclusion morphology, the axially orientated beltline weld metal in fact shows a lot of variation in the initiation mechanism, whereas second most inhomogeneity is found in the circumferentially orientated weld and the least inhomogeneity was in the RPVH weld. In axially orientated weld metal, most of the inclusions are irregularly shaped and there is some intergranular cracking evident. In the RPVH weld and circumferential beltline weld, all initiation sites are more or less similar with an oxide inclusion. The microstructure of the welds has been thoroughly investigated through the RPV wall thickness and found to be of very good quality [20].

Mild correlations to irradiation effect have been made in terms of the amount of intergranular cracking as more of it has been observed in the beltline weld than in the RPVH weld. However, the RPVH weld and the circumferentially orientated weld show overall more similarities in properties compared to the axially orientated beltline weld, while the axially orientated weld has been subjected to the highest amount of neutron fluence. It is believed that the orientation of the weld and the heat treatment during the welding process have caused a more pronounced effect on the material's performance [20]. Further investigations of the fractography and inclusions are reported separately.

4. Conclusions

This work studies the applicability of miniature C(T) specimens by using thermally aged and irradiated weld materials harvested from a decommissioned NPP after 28 years of operation. The study consists of fracture mechanics experimental testing in a hot cell environment, homogeneous reference temperature determination, a homogeneity screening, and an inhomogeneity assessment. Fractographical characterization was also conducted to gain insights into brittle crack initiation sites. The following conclusions are made:

- The reference temperature, T_0, values were determined by means of miniature C(T) specimens for the three investigated welds, and those were − 113.5 °C for the RPVH weld, −104.4 °C for the axially orientated beltline weld, and − 89.3 °C for the circumferentially orientated beltline weld, respectively. The results indicate that the region with the highest neutron fluence was not the most brittle one, and though the trend in miniature C(T) specimen results was slightly different compared to CVN T_0 estimation results, all defined T_0 temperatures were inside the margin of error.
- The multimodal inhomogeneity assessment method, for obtaining the multimodal reference temperature, T_m, was also used. The deviation of the T_m values was smallest in the axially orientated beltline weld, and this verifies that the inhomogeneity is also smallest in the axially orientated beltline region.
- In all three RPV welds investigated in this study, the primary fracture mechanism was cleavage fracture. An intergranular fracture was more prominent for irradiated beltline welds compared to the thermally aged RPVH weld. While the initiating particle in all three materials was an inclusion, the irradiated axial beltline weld exhibited some difference in the primary initiation mechanism compared to the irradiated circumferential weld and the thermally aged RPVH weld. The difference in inclusion type in the axial weld seems to correlate with the reference temperature.

CRediT authorship contribution statement

Laura Sirkiä: Writing – review & editing, Writing – original draft, Visualization, Validation, Investigation, Formal analysis, Data curation, Conceptualization. **Siddharth Suman:** Writing – review & editing, Visualization, Validation, Methodology, Investigation, Formal analysis, Data curation. **Pentti Arffman:** Writing – review & editing, Visualization, Validation, Software, Resources, Project administration, Methodology, Investigation, Funding acquisition, Formal analysis, Conceptualization. **Noora Hytönen:** Writing – review & editing, Visualization, Investigation. **Iikka Virkkunen:** Writing – review & editing, Supervision.

Declaration of competing interest

The authors declare that they have no known competing financial interests or personal relationships that could have appeared to influence the work reported in this paper.

Data availability

The data that support the findings of this study is available from the corresponding author upon reasonable request.

Acknowledgements

The authors express their gratitude to the SAFIR2022 BRUTE project (Barsebäck RPV material used for true evaluation of embrittlement) funded by VYR (Nuclear Waste Management Fund in Finland), VTT Technical Research Centre of Finland and NKS (Nordisk Kärnsäkerhet). The authors thank the BREDA program (Barsebäck Research & Development Arena) for providing the utilized research material. The supporting activities of J. Leporanta, J. Lukin and J. Saarinen are acknowledged. The contribution and discussions with P. Efsing from VATTENFALL are highly appreciated. Supervision and review of Dr. Z. Que and Dr. T. Saario, and review of Dr. O. Cronvall, are warmly acknowledged by the main author PhD Candidate L. Sirkiä.

References

[1] F. Naziris, C. Versteylen, F. Frith, M. Bregman, M. Kolluri, Development of Mini-Compact Tension specimen fabrication and test methods in hot cell for post-irradiation examination of Reactor Pressure Vessel steels, in: Proceedings of the ASME 2021 Pressure Vessel & Piping Conference PVP2021, July 13-15, 2021, Virtual, Online, 2021, pp. 1–6, https://doi.org/10.1115/PVP2021-61027.

[2] S. Cicero, M. Lambrecht, H. Swan, P. Arffman, E. Altstadt, T. Petit, et al., Fracture mechanics testing of irradiated RPV steels by means of sub-sized specimens: FRACTESUS project, Procedia Struct. Integrity 28 (2020) 61–66, https://doi.org/10.1016/j.prostr.2020.10.008.

[3] Y. Ha, T. Tobita, H. Takamizawa, Y. Nishiyama, Fracture toughness evaluation of neutron-irradiated reactor pressure vessel steel using miniature-C(T) specimens, in: Proceedings of the ASME 2017 Pressure Vessels and Piping Conference, PVP2017, July 16-20, 2017, Waikoloa, Hawaii, USA, PVP2017-65568, 2017, pp. 1–5, https://doi.org/10.1115/PVP2017-65568.

[4] T. Sugihara, T. Hirota, H. Sakamoto, K. Yoshimoto, K. Tsutsumi, T. Murakami, Applicability of miniature c(t) specimen to fracture toughness evaluation for the irradiated Japanese pressure vessel steel, in: Proceedings of the ASME 2017 Pressure Vessels and Piping Conference, PVP2017, July 16-20, 2017, Waikoloa, Hawaii, USA, 2017, pp. 1–8, https://doi.org/10.1115/PVP2017-66206.

[5] M. Lambrecht, R. Chaouadi, I. Uytdenhouwen, R. Gérard, Fracture toughness characterization in the transition and ductile regime of an a508 type weld metal with the mini-ct geometry before and after irradiation, in: Proceedings of the ASME 2020 Pressure Vessel & Piping Conference PVP2020, August 3, 2020, Virtual, Online, 2020, pp. 1–7, https://doi.org/10.1115/PVP2020-21515.

[6] P. Arffman, J. Lydman, N. Hytönen, Z. Que, S. Lindqvist, P. Efsing, Brute, Evaluation of mechanical properties of true reactor pressure vessel material from Barsebäck 2, in: Proceedings of the ASME 2022 Pressure Vessel & Piping Conference PVP2022 July 17-22, 2022, Las Vegas, Nevada, USA, 2022, pp. 1–7, https://doi.org/10.1115/PVP2022-83819.

[7] A. Das, P. Chekhonin, M. Houska, F. Obermeier, E. Altstadt, Master curve testing of RPV steels using mini-C(T) specimens – Irradiation effects and censoring statistics, Nuclear Materials and Energy 34 (2023) 101395, https://doi.org/10.1016/j.nme.2023.101395.

[8] U. Zerbst, R.A. Ainsworth, H.T. Beier, H. Pisarski, Z.L. Zhang, K. Nikbin, et al., Review on fracture and crack propagation in weldments - A fracture mechanics perspective, Eng Fract Mech 132 (2014) 200–276, https://doi.org/10.1016/j.engfracmech.2014.05.012.

[9] T. Jutla, Caterpillar Inc. Fatigue and fracture control of weldments, in: ASM Handbook, ASM International, 1996, pp. 434–449.

[10] ASTM E185-16. Standard Practice for Design of Surveillance Programs for Light-Water Moderated Nuclear Power Reactor Vessels. vol. 01. 2016. Doi: 10.1520/E0185-16.Copyright.

[11] ASTM E1921-20. Standard Test Method for Determination of Reference Temperature,T0, for Ferritic Steels in the Transition Range. 2020. Doi: 10.1520/E1921-20.2.

[12] K. Wallin, Inhomogeneity screening criterion for the ASTM E1921 to estimate based on the SINTAP lower-tail methodology, J Test Eval (2012) 40, https://doi.org/10.1520/JTE104241.

[13] J.A. Joyce, R. Tregoning, Evaluation of a method to characterize material inhomogeneity in ferritic steels within the ductile-to-brittle transition regime, Eng Fract Mech 78 (2011) 2870–2884, https://doi.org/10.1016/j.engfracmech.2011.08.001.

[14] K. Wallin, Assessment of master curve material inhomogeneity using small data sets. american society of mechanical engineers, Pressure Vessels and Piping Division (publication) PVP (2018) 1–10, https://doi.org/10.1115/PVP201884297, 1A–2018.

[15] K. Wallin, Fracture toughness of engineering materials_estimation and application, EMAS Publishing, UK, 2011.

[16] Z. Que, M. Lindroos, J. Lydman, N. Hytönen, S. Lindqvist, P. Efsing, et al., Brittle fracture initiation in decommissioned boiling water reactor pressure vessel head weld, J. Nucl. Mater. (2022) 569, https://doi.org/10.1016/j.jnucmat.2022.153925.

[17] N. Hytönen, P. Arffman, J. Lydman, S. Lindqvist, Z. Que, P. Efsing, Comparison of weld microstructure and brittle fracture initiation of reactor pressure vessel head weld and beltline axial weld, in: FONTEVRAUD 10 Conference September 19–22, Avignon France, 2022, pp. 1–8.

[18] J. May, J. Rouden, P. Efsing, M. Valo, H. Hein, Extended mechanical testing of RPV surveillance materials using reconstitution technique for small sized specimen to assist long term operation, in: M. Sokolov, E. Lucon (Eds.), Small Specimen Test Techniques: 6th Volume, ASTM International, USA, 2015, pp. 88–109, 10.1520/STP157620130189.

[19] N. Hytönen, Z. Que, P. Arffman, J. Lydman, P. Nevasmaa, U. Ehrnstén, et al., Effect of weld microstructure on brittle fracture initiation in the thermally aged boiling water reactor pressure vessel head weld metal, Int. J. Miner. Metall. Mater. 28 (2021) 867–876, https://doi.org/10.1007/s12613-020-2226-6.

[20] S. Lindqvist, A. Norrgård, P. Arffman, N. Hytönen, J. Lydman, P. Efsing, et al., Mechanical behavior of high-Ni/high-Mn Barsebäck 2 reactor pressure vessel welds after 28 years of operation, J. Nucl. Mater. (2023) 581, https://doi.org/10.1016/j.jnucmat.2023.154447.

Scripta Materialia 258 (2025) 116497

Contents lists available at ScienceDirect

Scripta Materialia

journal homepage: www.journals.elsevier.com/scripta-materialia

Irradiation-induced clustering in a high-Ni, high-Mn, low-Cu boiling water reactor pressure vessel weld after 28 full power years

David Mayweg [a,*], Kristina Lindgren [a,d], Pål Efsing [b,c], Mattias Thuvander [a]

[a] Chalmers University of Technology, Department of Physics, Göteborg SE-412 96, Sweden
[b] Department of Solid Mechanics, Royal Institute of Technology (KTH), Stockholm SE-100 44, Sweden
[c] Ringhals AB, Väröbacka SE-430 22, Sweden
[d] Now at RISE, Mölndal SE-431 53, Sweden

ARTICLE INFO

Keywords:
Irradiation-induced clustering
Atom probe tomography
Reactor pressure vessel steel
Boiling water reactor

ABSTRACT

High-Ni, high-Mn welds are the life-time determining components in reactor pressure vessels (RPVs) of Nordic reactors at desired operating times of pressurized water reactors (PWR) of 60 or even 80 years due to embrittlement that is caused by pronounced clustering of Ni, Mn and Si. To understand early stages of clustering we performed atom probe tomography (APT) measurements on an axial weld of the boiling water RPV from Barsebäck Unit 2 decommissioned after 28 years of operation. Contrary to our previous work on the same weldment, here we report observation of clustering. The cluster number densities vary significantly between individual APT measurements, which we attribute to variations in local Ni and Mn concentrations, a trend even seen within single grains. Based on comparison with high fluence samples containing more and larger clusters we propose that NiMnSi cluster formation and growth is an irradiation-induced continuous process without a relevant threshold dose.

Nuclear reactor pressure vessels (RPVs) are manufactured from ferritic low alloy steels [1]. Such steels exhibit a pronounced ductile to brittle transition (DBT) [2–4]. The DBT temperature (DBTT) is adversely affected by thermal ageing combined with neutron irradiation [5]. The ageing effects can be divided into non-hardening – mostly P segregation to grain boundaries (GBs) – and hardening effects, which are related to irradiation-induced defects from fast neutrons that facilitate diffusion and clustering or precipitation of solutes (Cu, Ni, Mn, Si, P) [3,4,6–8]. These mechanisms have been characterize by X-ray techniques [9,10], positron annihilation spectroscopy [11], and APT investigations [6, 12–23]. Early investigations of RPVs revealed that Cu plays a key role in embrittlement [2] due to formation of coherent Cu-rich precipitates [6, 14,15,24], which is accelerated by radiation enhanced diffusion [3]. The independent role of Ni in low-Cu (<0.05 at%) steels was only noticed some decades later [25,26] and it was proposed that NiMnSi clusters with negligible Cu fraction forming in such materials are subject to an incubation period [3,27]. Based on this assessment there is an ongoing debate with respect to the nature of these solute clusters in low-Cu steels, namely, if they are or can become separate phases at later stages, i.e., whether their formation is thermodynamically favored and accelerated by radiation enhanced diffusion [28,29] or they are stabilized by irradiation-induced point defects (vacancies and self-interstitial atoms) [30–32]. Following the model laid out by Castin et al. [31] we believe that, simply put, clusters in the low-Cu RPV welds that we are concerned with ([20] and this work) are mainly defect stabilized. The form via radiation induced segregation of solutes to point defects. Phase separation does not occur at relevant time scales (low-Cu, high-Ni material was the only alloy in a wide range of compositions where no evidence for G-phase formation was reported [10]).

Prediction of changes in the mechanical properties and assessment of the operative limits of RPVs is conducted in surveillance programs (e.g., [22,33]). In the case of the Nordic RPVs the welds are critical parts of the structure. At the time they were manufactured it was already known that Cu strongly enhances the irradiation embrittlement [24] and, hence, weld metal with low levels of Cu [33] and some 1.5 wt% Ni and Mn was used. For the RPVs of Ringhals Unit 3 and 4 an R&D program to support long term operation has been undertaken [17,18,20,21,34]. To understand the full microstructure evolution starting at low damage levels materials were harvested from the decommissioned boiling water reactor (BWR) Barsebäck Unit 2 RPV [35]. This material has been subjected to mechanical and microstructural characterization [36,37] and atom probe tomography (APT) [38]. The current study is an extension of

* Corresponding author.
E-mail addresses: david.mayweg@chalmers.se, david.mayweg@gmail.com (D. Mayweg).

https://doi.org/10.1016/j.scriptamat.2024.116497
Received 26 October 2024; Received in revised form 5 December 2024; Accepted 6 December 2024
Available online 12 December 2024

Table 1
Chemical composition determined by optical emission spectroscopy (from [37]).

	Ni	Mn	Si	Mo	C	Cu	Cr	Co	P	Al	S	Fe
at%	1.58	1.45	0.32	0.26	0.25	0.06	0.03	0.02	0.02	0.004	0.009	bal.
wt%	1.66	1.43	0.16	0.44	0.054	0.07	0.03	0.02	0.01	0.02	0.005	bal.

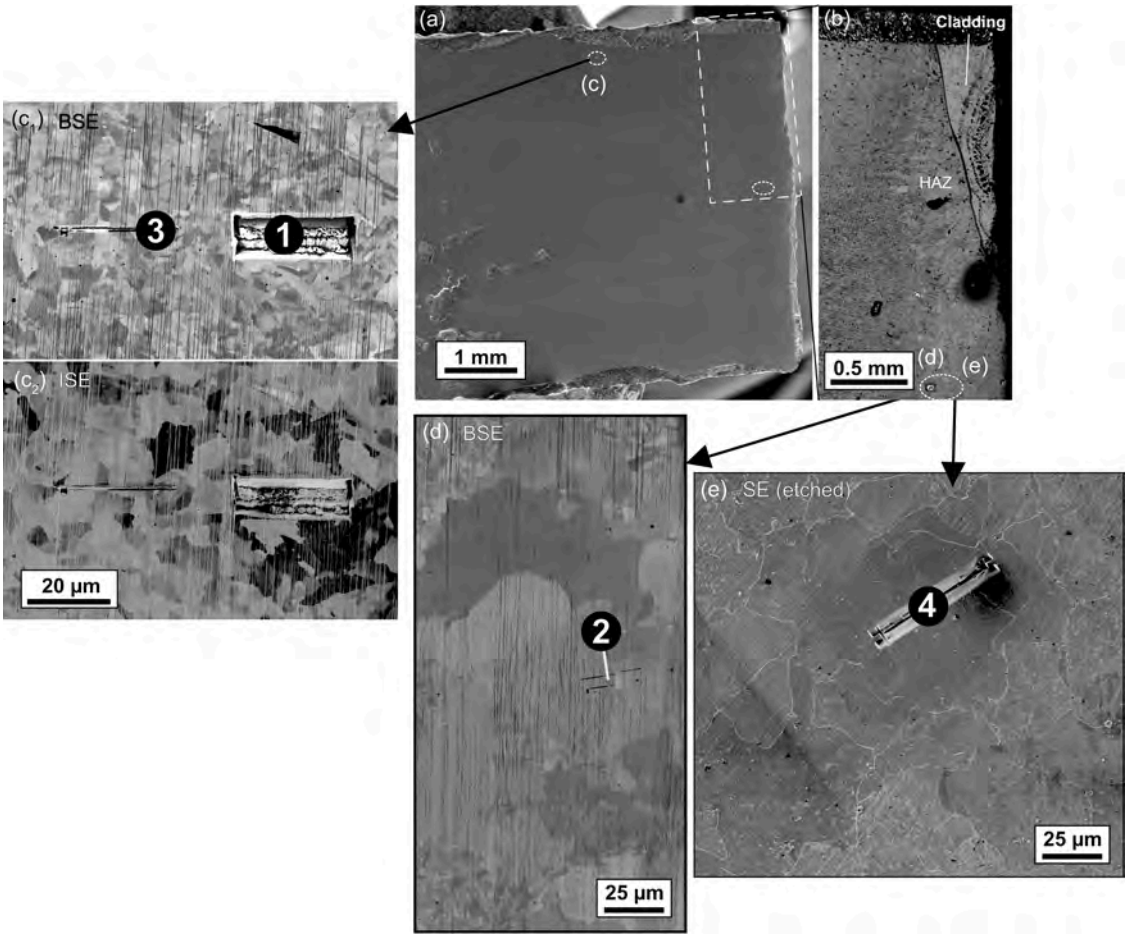

Fig. 1. Electron images of a sample from an axial weld of the Barsebäck 2 RPV weld close to the cladding. (a) Overview secondary electron (SE) image, (b) backscatter electron (BSE) image highlighting the cladding and the HAZ. (c_1) and (c_2) are BSE and ion-induced secondary electron images (ISE) of APT lift-out locations from the normal weld microstructure (position 1 from [38]). (d) and (e) are BSE and SE images of the lift-out location in the HAZ adjacent to the cladding.

the work in [38] and features more APT measurements to understand the early-in-life behavior of NiMnSi clusters formed during reactor operation.

We investigated an axial beltline weld (bulk composition, see Table 1) from the Barsebäck 2 RPV reaching a nominal fast neutron fluence of 7.9×10^{21} n/m^2 (28 full power years). The DBTT was not affected [37] (Yuya et al. [39] reported a DBTT shift of +26 °C for a BWR RPV with a fluence of 1.5×10^{22} n/m^2 containing 1.48 wt% Mn, 0.56 wt % Ni and 0.09 wt% Cu). APT specimen preparation was performed using an FEI Versa3D focused ion beam using standard procedures [40] (final annular milling: nominal 30 or 50 pA at 30 kV with mask inner diameter 100 nm, final cleaning at 2 kV and 28 pA for 30 s).

APT experiments were conducted in a Cameca LEAP 6000XR (detection efficiency 52 %, laser wavelength 257.5 nm). Experimental parameters are provided in a table in the supplementary material. In voltage pulsing APT the number of collected ions often was relatively small (typically 1–3 $\times$ 10^6 ions) so we additionally used laser pulsing APT, which is less well-suited for characterizing cluster size and

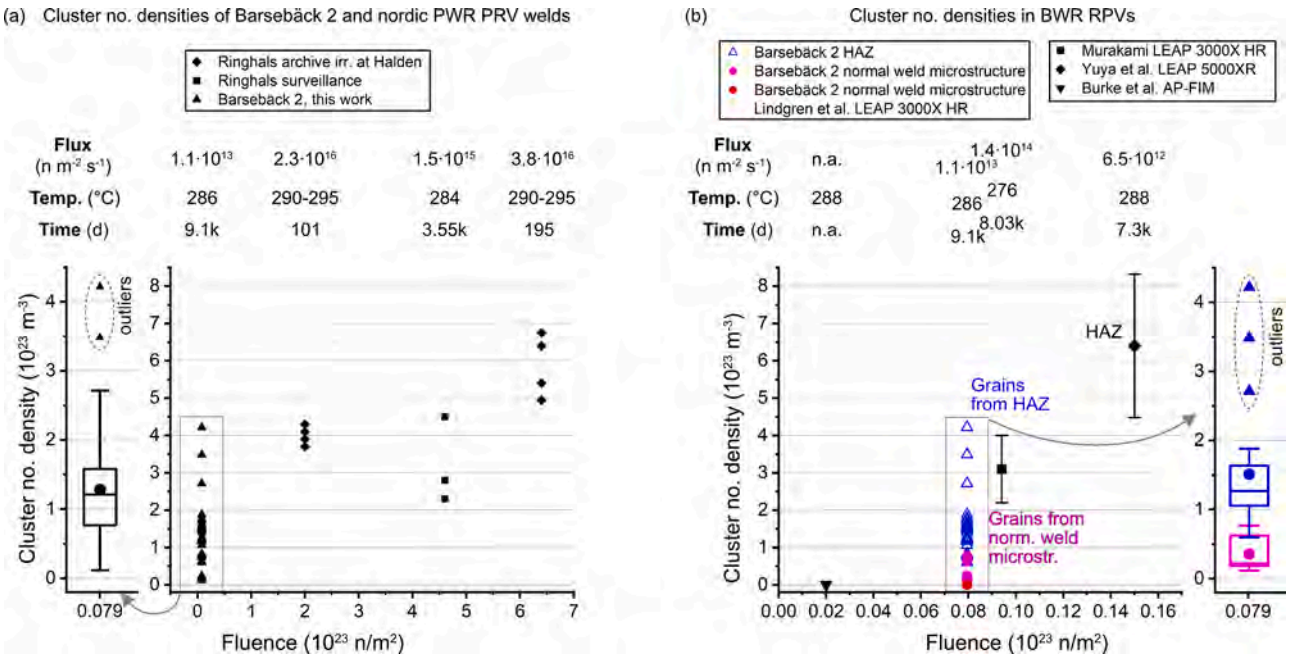

Fig. 2. Cluster number density vs. fast neutron fluence (> 1 MeV), with flux, irradiation temperature and time given above the plots. In (a) the data obtained in this work (that are additionally represented as a box plot) are compared to high fluence data from Nordic (high-Ni, high-Mn, low-Cu) RPV steel from [20]. In (b) our data (colored, see text) are presented in comparison to low fluence literature values from BWR RPVs [14,38,39,49]. Again, the data from the present work are additionally represented in box plots. Note that Burke et al. [14] used AP-FIM and did not detect any clusters at all, likely due to the small captured volumes.

Table 2
Statistics of the cluster number densities (10^{23} clusters/m^3) from our APT experiments.

	All data from this work combined	Normal weld microstructure	Heat-affected zone (HAZ)	Yuya [39] (HAZ)	Murakami [49]
N (no. of APT datasets)	31	6	25	41	–
Mean	1.3	0.4	1.5	6.4	3.1
Standard deviation	0.9	0.3	0.8	1.6	0.9
Median	1.2	0.2	1.3	–	–
Maximum	4.2	0.8	4.2	–	–
Minimum	0.2	0.2	0.6	–	–

composition as it is leading to significant surface diffusion of Si, P and Cu [41]. But since laser pulsing allows for the collection of much larger datasets (> 10^7 ions) we used it to capture larger volumes increasing the confidence in the cluster number density determination. All datasets were crystallographically calibrated [42,43]. Compositions were calculated using the built-in peak decomposition in AP Suite 6.3. In voltage pulsing Mn and Cu are systematically underestimated [41] (see supplementary material, Appendix A). Cluster analysis was performed using the version of the maximum separation method [44] implemented in AP Suite 6.3. For voltage pulsing datasets we included Ni, Mn and Si

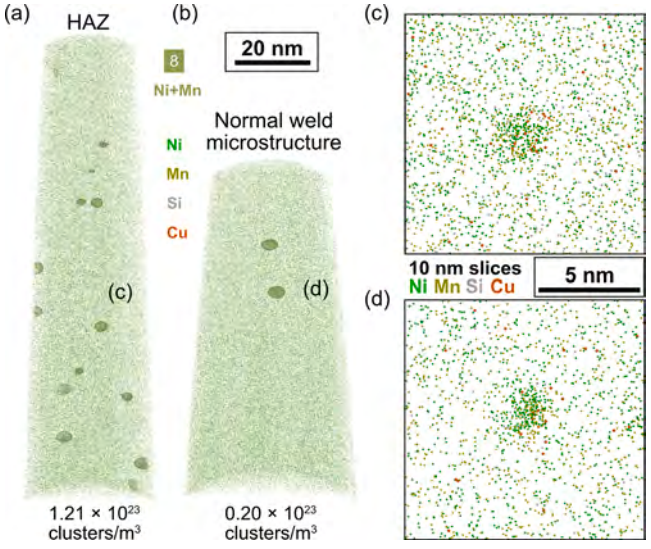

Fig. 3. (a) and (b) are 3D atom maps from APT reconstructions displaying Ni, Mn, Si and Cu from the HAZ (50 K, 15 pJ) and the normal weld microstructure (50 K, 20 pJ), respectively. 6 at% Ni+Mn ICSs highlight larger clusters. The views in (c) and (d) depict 10 nm slices including a single cluster from (a) and (b).

Table 3
Comparison of compositions of the specimens in Fig. 3 (50 K base temperature and 20 and 15 pJ LPE).

	Normal weld microstructure		HAZ	
Clusters/m^3	0.20×10^{23}		1.21×10^{23}	
	Composition (at%)			
	Full dataset	6 at% Ni+Mn ICS removed	Full dataset	6 at% Ni+Mn ICS removed
Ni	1.40	1.39	1.47	1.44
Mn	1.19	1.18	1.37	1.35
Si	0.20	0.20	0.29	0.28
Cu	0.04	0.04	0.04	0.04

ions, for laser pulsing datasets only Ni and Mn were used. P and Cu are only present in small amounts and were therefore not included in the cluster search. For every dataset we performed a sweep of the maximum separation distance (d_{max}) and chose this parameter from the plateau region between 0.4 and 0.55 nm (see Figure S1). If no clear plateau was present, we chose the value with the lowest slope between 0.4 and 0.6 nm. Clusters with 25 or more detected solute atoms were considered for analysis. The cluster numbers obtained for each dataset agree well with isoconcentration-surface-(ICS)-based cluster identification (typically 10–20 % difference, see Figure S2). Radial concentration profiles were created based on the cluster dimensions of the identified solutes in AP Suite. Most of the clusters found in the here presented work have radii smaller than ~ 1 nm (~ 350 atoms) for which compositions cannot be reliably determined by APT [45]. Since large clusters (> 3000 atoms) from comparable high fluence material [20] did contain Fe, we included it in the cluster composition analysis although it is most likely significantly overestimated. Because we cannot quantify the lateral resolution and the evaporation field differences we are not able to determine the real Fe fraction inside clusters [46].

Fig. 1 comprises electron images of the bulk specimen from which the lift-outs for APT analyses were taken: (a) is an overview marking the approximate positions of the lift-outs by dashed ellipses and (b) is a magnified view of the dashed rectangle in (a) highlighting the cladding in the upper right and the coarse-grained heat affected zone (HAZ). The grain morphology is shown in (c) – (e): The same region from the normal weld microstructure is depicted in (c_1) and (c_2) as a backscatter electron and an ion-induced secondary electron image, respectively, both showing the typical weld morphology. (d) shows the transition region, where weld morphology is visible in direct vicinity of grains that extend over more than 100 μm. Finally, (e) is depicting a region in the HAZ where only coarse grains are present.

Fig. 2(a) is a plot comparing cluster number densities obtained in the present work with high fluence (high flux) data from Nordic RPV welds: a surveillance specimen from Ringhals Unit 4 and its archive material irradiated in the Halden research reactor [20] (note that the cluster sizes are significantly different). The data from the present work are additionally presented as a box plot. Fig. 2(b) is a comparison of the present results with low fluence (low flux) literature data (note that cluster analysis results strongly depend on the parameter choice [47,48]) from BWRs including earlier work from the same weldment where no clusters of any kind were found in 10 needle specimens ([38] see lift-out location 1 in Figure 1 (c)). The data from the Barsebäck 2 RPV weld are represented in magenta for the normal weld microstructure, blue for the HAZ and red (from [38]), while the literature values are shown in black. The box plots of the data from this work provide a better visualization of the number density statistics that are provided in Table 2 alongside literature values for comparison (note the different Cu levels: Murakami [49] 0.24 wt%; Yuya et al. [39] 0.09 wt% Cu).

The plots in Fig. 2 clearly show that comparatively higher cluster number densities are found in coarse grains of the HAZ. Also noteworthy is the large scatter with the highest values on the level of that seen in the Ringhals 4 material.

Fig. 3 allows for visual comparison of two APT specimens from the HAZ and the normal weld microstructure (coarse- and fine-grained regions), respectively. Clusters are scarce but recognizable by visual inspection. The reconstruction depicted in Fig. 3(a) and (c) is from lift-out position 2 (Fig. 1(d)), while that shown in Fig. 3(b) and (d) is from lift-out position 3 (Fig. 1(c)). The cluster number density of the dataset from HAZ is six times larger than that of the fine-grained region, which is associated with an 0.25 at% higher Ni+Mn fraction as listed in Table 3.

The table includes measured fractions (clusters included vs. removed) of Ni and Mn in the two APT specimens in Fig. 3. Similar experimental parameters ensure comparability. Because of the low volume fraction of the clusters the difference is not due to the presence of clusters but the larger total concentration of these elements.

Fig. 4(a) shows an secondary electron (SE) image of the HAZ with a very large grain (Grain 1). We performed a lift-out targeting a total of three grains, including a GB and a region spanning roughly 20 μm inside Grain 1. The positions of the individual specimens are marked by color-coded circles. Figure 4 (b) depicts a plot of cluster number density over the Ni+Mn fraction for the individual APT measurements. Only laser pulsing datasets were included in the linear fit ($R^2 = 0.74$, $p = 0.002$) because of underestimation of Mn in voltage pulsing (arrows indicate their positions 'corrected' by 0.25 at%). The GB was captured in one measurement and a reconstruction of this dataset is presented in Figure 4 (c). There appears to be a cluster denuded zone with a width of approximately 50 nm next to the GB; the Ni, Mn and Si fractions are nearly identical in this region compared to the volume in which clusters are present. This observation can be rationalized by GBs acting as sinks for point defects [50,51]. Assuming their presence is a precondition for cluster formation [31] the absence of clusters indicates a relevant reduction in the number of point defects. The plot in Figure 4 (b) shows that cluster number densities are varying by a factor as large as five with the fraction of Ni and Mn even within a single grain (Grain 1). Figure 4 (d) shows two plots of the Ni- and Mn-fraction (balance almost exclusively Fe) in the clusters from measurements #6 and #8 highlighted in Figure 4 (b) by a triangle and a diamond symbol, respectively. Cluster size (number of atoms per cluster) and composition show similar distributions.

This assessment is confirmed quantitatively in Table 4. The 0.5 at% larger Ni+Mn fraction is associated with a five times higher cluster number density, while average cluster composition and number of atoms per cluster are similar. A possible conclusion is that cluster formation is more enhanced by the larger solute fractions than the degree of acceleration in growth of individual clusters.

From an assessment of all laser pulsing datasets (Table 5, see respective plots in Figure S3) a significant correlation of cluster number

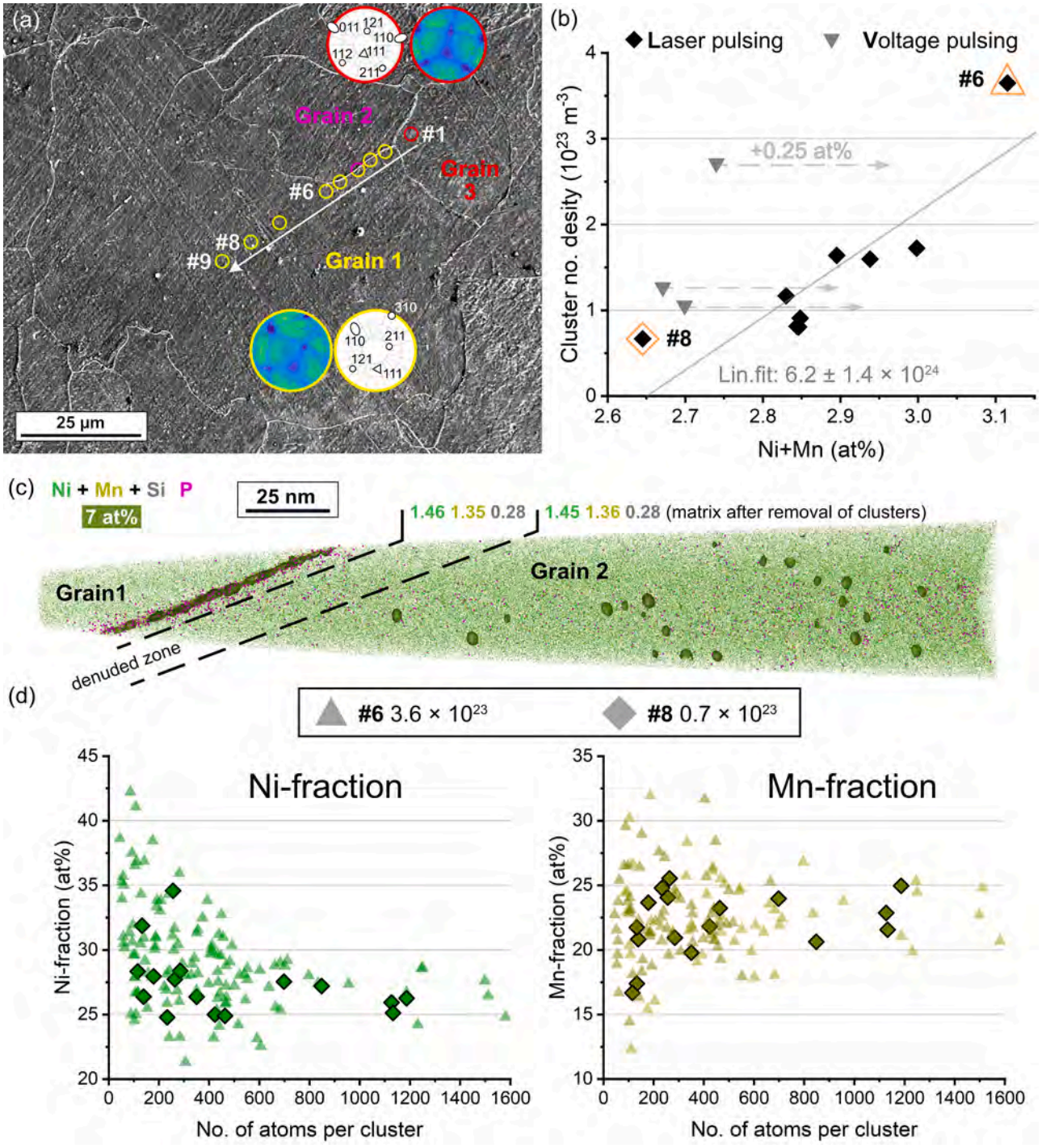

Fig. 4. Clustering in the HAZ near the cladding. (a) is an SE image after etching with 5 % Nital; the positions of the individual APT specimens are marked by circles and color-coded for grains 1, 2, and 3 (identified based on their crystallographic orientation, see insets obtained with code from [43]). (b) shows plots of cluster number density vs. the Ni+Mn fraction (fitting the data from laser pulsing datasets yields $R^2 = 0.74$, $p = 0.003$). The open triangles are the voltage pulsing datasets with (c) a reconstruction from lift-out position 4 (magenta circle segment) including a GB, showing a potentially cluster denuded zone (the composition of the volumes separated by dashed lines ins given in the same color coding as the ions). (d) comparison of Ni and Mn fraction in the clusters of APT specimens #6 and #8 from Grain 1 (marked extreme cases in (b) by a triangle and a diamond).

Table 4
Cluster statistics of the two APT datasets shown in Fig. 4(d) from specimens #6 and #8. Cluster analysis parameters: $d_{max} = 0.42$ nm, $N_{min} = 25$, $L = e = 0.25$ nm). The value given after the ± sign is the standard deviation.

	Specimen	
	#6	#8
No. of clusters	123	18
Cluster no. density (10^{23} m^{-3})	3.6	0.7
Volume (10^{-23} m^3)	33.7	26.9
No. of ions per cluster incl. Fe	271 ± 177	234 ± 196
No. ions per cluster excl. Fe	140 ± 91	120 ± 100
Ni in clusters (at%)	29.2 ± 3.9	27.0 ± 3.9
Mn in clusters (at%)	22.5 ± 3.2	22.8 ± 4.2
Ni in full spectrum (at%)	1.62	1.33
Mn in full spectrum (at%)	1.50	1.31

Table 5
Results from linear regression of the composition and cluster number density data points from all laser pulsing datasets from this work.

	Ni	Mn	Si	Cu	P	C
Slope (10^{24} clusters m^{-3}/at %)	1.08 ±0.15	1.13 ±0.17	2.73 ±0.93	3.21 ±2.36	10.79 ±6.25	−0.28 ±1.07
R^2	0.71	0.68	0.29	0.08	0.13	0.003
p	4E-7	1.2E-6	> 0.01	0.19	0.10	0.80

density and solute fraction was confirmed for Ni, Mn, Si but not for Cu, P and C.

Fig. 5 is a comparison of solute clustering in the Barsebäck 2 (B2) RPV weld and a Ringhals 4 (R4) surveillance sample of nominally 58 times higher fluence [20]. The two specimens were measured with similar APT parameters (70/50 K, 20 % pulse fraction, detection rate 0.5 %, LEAP 6000XR and LEAP 3000X HR). The overall difference in cluster size and their different compositions are highlighted by the atom maps in Fig. 5(a) and (b). The 6 at% (Ni+Mn+Si) ICSs in Figure 5 (a) highlight the difference in cluster volume and number density. The clusters in the two materials are however more similar than they visually appear as Figure 5 (c) demonstrates (see also Figure S4). It comprises plots of radial concentration profiles for Ni and Mn where clusters are divided in size groups (calculated including Fe, clusters > 2000 atoms/cluster are excluded since those are not present in the B2 specimen; they are depicted in Figure S5). While the R4 clusters exhibit slightly higher concentrations near the center (see also Figure S6), the profiles for the two specimens are strikingly similar despite the significant difference in fluence. Table 6 includes a comparison of the matrix fractions of Ni and Mn in the specimens shown in Fig. 5. It is apparent that in both cases clustering leads to depletion of the matrix although due to the small volume fraction of the clusters this is not very pronounced in the B2 material. What is interesting to note is that Ni and Mn fractions are lower in the matrix of the R4 specimen, i.e., the continued irradiation leads to successive removal of Ni and Mn from the matrix.

According to the model in [31] nuclei (as small as two solutes segregated to a point defect cluster) continuously form and grow by addition of further solute/point defect pairs; dissolution by emission of vacancy solute pairs can also occur. Therefore, clusters are expected to have different size as function of flux, time, temperature and (local) composition. The assumption that irradiation-induced clustering took place in the here presented materials is supported by the lack of comparable NiMnSi clusters after purely thermal annealing of similar welds [52]. There, exclusively precipitates with Cu-rich cores and NiMnSi-shells were found near dislocations. This finding is particularly meaningful due to the comparatively large amount of data that was collected from 19 electropolished wire specimens. Additional support for this interpretation is a post irradiation annealing (PIA) study of Nordic RPV welds by Lindgren et al. [53] that indicates low stability of NiMnSi clusters found in these materials: while they disappeared after 24 h at 410 °C, Cu-rich clusters near dislocations similar to those in the purely thermally annealed weld in [52] remained. Even as this line of reasoning appears to be consistent, there remains room for debate. It is for example not clear why the clusters shown in Fig. 4(d) have similar (measured) compositions although the local Ni+Mn fraction varies by 0.5 at%. These differences in matrix composition should be reflected in the cluster composition [32]. In addition, there is evidence for similar low-Cu, high-Ni model alloys indicating a much higher stability of NiMnSi clusters. For example, PIA studies by Almirall et al. [29,54] showed that some large clusters persisted after up to more than one year at 425 °C. Based on the available information in [20,29,52–54] we do not see any obvious explanation for this discrepancy.

In conclusion we would like to summarize the findings from our APT results obtained from a low fluence, low flux BWR RPV weld as follows.

Cluster number densities between individual APT measurements vary by a factor of up to 36 between the smallest and the highest value. The significant variation in cluster number density across many APT specimens is correlated with – and likely caused by – the local Ni and Mn concentrations as was shown to be the case even within a single grain (Fig. 4 and Figure S3). One APT measurement capturing a GB can be construed as showing a cluster denuded zone, which might be explained by the GB constituting a sink for point defects.

The key finding from our work is that there appears to be no fundamental difference between clusters in the low fluence Barsebäck 2 and the high fluence Ringhals surveillance weld material. We have shown that NiMnSi clustering in *Nordic RPV steel weldments* takes place already at low fluence. These clusters are similar to those in high fluence weldments and differ from others found after thermal annealing [52, 55]. We therefore propose that their existence comes about by a continuous process of defect-mediated cluster formation that is accompanied by the growth of already existing clusters.

A final note on our previous study [38]: We do not have a good explanation why we did not find clusters in the previous APT experiments. The matrix of specimens from the present work shows slightly higher probability of Ni-Ni (Ni-Mn, Ni-Si, Ni-Cu) neighborhood in a very similar manner as shown in [38], indicating early clustering that eludes recognition due to limitations of the technique [48]. In conclusion we can hence only emphasize again, that APT studies are prone to insufficient sample sizes limiting the statistical power.

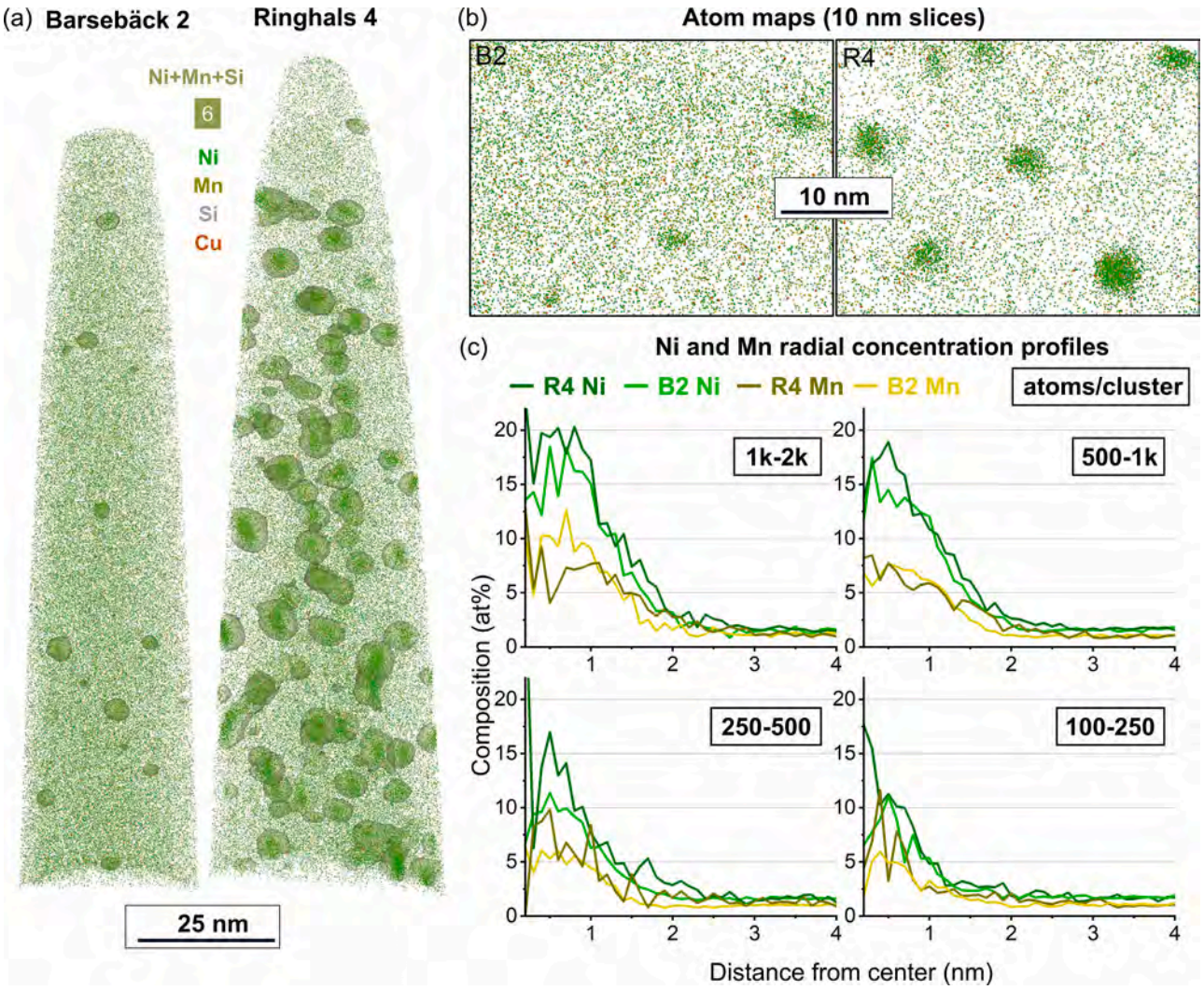

Fig. 5. Comparison of APT data from Barsebäck 2 (B2) RPV (70 K, 20 % PF) and from Ringhals 4 surveillance material (R4) from Lindgren et al. [20] (50 K, 20 % PF). (a) Atom maps of voltage pulsing datasets with clusters highlighted by 6 at% Ni+Mn+Si ICSs. Note that this value does not appear to be a well-suited descriptor for the R4 specimen, but was chosen for the purpose of comparison. (b) Atom maps of 10 nm thick volumes highlighting the appearance of individual clusters. (c) Radial concentration profiles for Ni and Mn cluster size classes (clusters > 2000 atoms were only present in the R4 specimen and are not included here; plots are available in the supplementary material).

Table 6
Volume fraction of clusters and composition (in at%) of the matrix after removal of the clusters from the datasets in Fig. 5.

	B2	R4
Volume fraction (%)	0.15	2.11
Total Ni	1.37	1.73
Ni matrix	1.35	1.21
Total Mn	1.13	1.27
Mn matrix	1.11	1.00

CRediT authorship contribution statement

David Mayweg: Writing – review & editing, Writing – original draft, Visualization, Methodology, Investigation, Formal analysis, Conceptualization. **Kristina Lindgren:** Writing – review & editing, Investigation, Funding acquisition. **Pål Efsing:** Writing – review & editing, Writing – original draft, Funding acquisition, Conceptualization. **Mattias Thuvander:** Writing – review & editing, Supervision, Funding acquisition, Conceptualization.

Declaration of competing interest

The authors declare that they have no known competing financial interests or personal relationships that could have appeared to influence the work reported in this paper.

Acknowledgments

This research was funded by the Nordic Nuclear Safety (NKS) projects BREDA and REPoUSSES, and by the Euratom research and training programme 2019-2020; European Database for Multiscale Modelling of Radiation Damage (ENTENTE), Grant agreement No. 900018. The authors want to thank Jenny Roudén and Johan Blomström (Ringhals AB) who provided valuable information about the specimen history. DM is thankful for fruitful discussions with Milan Konstantinović and Nicolas Castin. This work was carried out at Chalmers Materials Analysis Laboratory (CMAL).

Supplementary materials

Supplementary material associated with this article can be found, in

the online version, at doi:10.1016/j.scriptamat.2024.116497.

References

[1] T. Allen, J. Busby, M. Meyer, D. Petti, Materials challenges for nuclear systems, Mater. Today 13 (12) (2010) 14–23.
[2] L.E. Steele, Status of USA Nuclear Reactor Pressure Vessel Surveillance for Radiation Effects, ASTM International, West Conshohocken, PA, 1983.
[3] G.R. Odette, G.E. Lucas, Recent progress in understanding reactor pressure vessel steel embrittlement, Radiat. Effects Defects Solids 144 (1–4) (1998) 189–231.
[4] K. Fukuya, Current understanding of radiation-induced degradation in light water reactor structural materials, J. Nucl. Sci. Technol. 50 (3) (2013) 213–254.
[5] Integrity of reactor pressure vessels in nuclear power plants: assessment of irradiation embrittlement effects in reactor pressure vessel steels, International Atomic Energy Agency, Vienna, 2009.
[6] M.K. Miller, M.G. Burke, An atom probe field ion microscopy study of neutron-irradiated pressure vessel steels, J. Nucl. Mater. 195 (1) (1992) 68–82.
[7] W.J. Phythian, C.A. English, Microstructural evolution in reactor pressure vessel steels, J. Nucl. Mater. 205 (1993) 162–177.
[8] J.T. Buswell, W.J. Phythian, R.J. McElroy, S. Dumbill, P.H.N. Ray, J. Mace, R. N. Sinclair, Irradiation-induced microstructural changes, and hardening mechanisms, in model PWR reactor pressure vessel steels, J. Nucl. Mater. 225 (1995) 196–214.
[9] F. Bergner, M. Lambrecht, A. Ulbricht, A. Almazouzi, Comparative small-angle neutron scattering study of neutron-irradiated Fe, Fe-based alloys and a pressure vessel steel, J. Nucl. Mater. 399 (2–3) (2010) 129–136.
[10] D.J. Sprouster, J. Sinsheimer, E. Dooryhee, S.K. Ghose, P. Wells, T. Stan, N. Almirall, G.R. Odette, L.E. Ecker, Structural characterization of nanoscale intermetallic precipitates in highly neutron irradiated reactor pressure vessel steels, Scr. Mater. 113 (2016) 18–22.
[11] M.J. Konstantinović, I. Uytdenhouwen, G. Bonny, N. Castin, L. Malerba, P. Efsing, Radiation induced solute clustering in high-Ni reactor pressure vessel steel, Acta Mater. 179 (2019) 183–189.
[12] M.K. Miller, K.F. Russell, Embrittlement of RPV steels: an atom probe tomography perspective, J. Nucl. Mater. 371 (1) (2007) 145–160.
[13] M.K. Miller, M.A. Sokolov, R.K. Nanstad, K.F. Russell, APT characterization of high nickel RPV steels, J. Nucl. Mater. 351 (1) (2006) 187–196.
[14] M.G. Burke, S.P. Grant, M.K. Miller, APFIM investigations of solute clusterig and precipitation in irradiated RPV steels, in: 4th International Conference in Nuclear Power Systems - Water Reactors, Jekyll Island, GA, USA, 1989.
[15] M.K. Miller, M.G. Hetherington, M.G. Burke, Atom probe field-ion microscopy: a technique for microstructural characterization of irradiated materials on the atomic scale, Metall. Trans. A 20 (12) (1989) 2651–2661.
[16] E. Meslin, B. Radiguet, P. Pareige, A. Barbu, Kinetic of solute clustering in neutron irradiated ferritic model alloys and a French pressure vessel steel investigated by atom probe tomography, J. Nucl. Mater. 399 (2) (2010) 137–145.
[17] M.K. Miller, K.A. Powers, R.K. Nanstad, P. Efsing, Atom probe tomography characterizations of high nickel, low copper surveillance RPV welds irradiated to high fluences, J. Nucl. Mater. 437 (1) (2013) 107–115.
[18] P.D. Styman, J.M. Hyde, D. Parfitt, K. Wilford, M.G. Burke, C.A. English, P. Efsing, Post-irradiation annealing of Ni–Mn–Si-enriched clusters in a neutron-irradiated RPV steel weld using Atom Probe Tomography, J. Nucl. Mater. 459 (2015) 127–134.
[19] P.D. Edmondson, M.K. Miller, K.A. Powers, R.K. Nanstad, Atom probe tomography characterization of neutron irradiated surveillance samples from the R. E. Ginna reactor pressure vessel, J. Nucl. Mater. 470 (2016) 147–154.
[20] K. Lindgren, M. Boåsen, K. Stiller, P. Efsing, M. Thuvander, Evolution of precipitation in reactor pressure vessel steel welds under neutron irradiation, J. Nucl. Mater. 488 (2017) 222–230.
[21] K. Lindgren, K. Stiller, P. Efsing, M. Thuvander, On the analysis of clustering in an irradiated low alloy reactor pressure vessel steel weld, Microsc. Microanal.: Off. J. Microsc. Soc. America, Microbeam Anal. Soc., Microsc. Soc. Canada 23 (2) (2017) 376–384.
[22] B.M. Jenkins, J.O. Douglas, N. Almirall, N. Riddle, P.A.J. Bagot, J.M. Hyde, G. R. Odette, M.P. Moody, The effect of composition variations on the response of steels subjected to high fluence neutron irradiation, Materialia (Oxf) 11 (2020).
[23] N. Almirall, P.B. Wells, T. Yamamoto, K. Wilford, T. Williams, N. Riddle, G. R. Odette, Precipitation and hardening in irradiated low alloy steels with a wide range of Ni and Mn compositions, Acta Mater. 179 (2019) 119–128.
[24] G.R. Odette, On the dominant mechanism of irradiation embrittlement of reactor pressure vessel steels, Scr. Metall. 17 (10) (1983) 1183–1188.
[25] M.M. Ghoneim, F.H. Hammad, Pressure vessel steels: influence of chemical composition on irradiation sensitivity, Int. J. Pressure Vessels Piping 74 (3) (1997) 189–198.
[26] C. Guionnet, B. Houssin, D. Brasseur, A. Lefort, D. Gros, R. Perdreau, Radiation embrittlement of PWR reactor vessel weld metals: nickel and copper synergism effects, in: J.S. Perrin (Ed.), Effects of Radiation on Materials, ASTM International, West Conshohocken, PA, pp. 392–411.
[27] G.R. Odette, T. Yamamoto, T.J. Williams, R.K. Nanstad, C.A. English, On the history and status of reactor pressure vessel steel ductile to brittle transition temperature shift prediction models, J. Nucl. Mater. 526 (2019).
[28] H. Ke, P. Wells, P.D. Edmondson, N. Almirall, L. Barnard, G.R. Odette, D. Morgan, Thermodynamic and kinetic modeling of Mn-Ni-Si precipitates in low-Cu reactor pressure vessel steels, Acta Mater. 138 (2017) 10–26.
[29] N. Almirall, P.B. Wells, H. Ke, P. Edmondson, D. Morgan, T. Yamamoto, G. R. Odette, On the elevated temperature thermal stability of nanoscale Mn-Ni-Si precipitates formed at lower temperature in highly irradiated reactor pressure vessel steels, Sci. Rep. 9 (1) (2019) 9587.
[30] G. Bonny, D. Terentyev, A. Bakaev, E.E. Zhurkin, M. Hou, D. Van Neck, L. Malerba, On the thermal stability of late blooming phases in reactor pressure vessel steels: an atomistic study, J. Nucl. Mater. 442 (1–3) (2013) 282–291.
[31] N. Castin, G. Bonny, A. Bakaev, F. Bergner, C. Domain, J.M. Hyde, L. Messina, B. Radiguet, L. Malerba, The dominant mechanisms for the formation of solute-rich clusters in low-Cu steels under irradiation, Mater. Today Energy 17 (2020).
[32] N. Castin, G. Bonny, M.J. Konstantinović, A. Bakaev, F. Bergner, C. Courilleau, C. Domain, B. Gómez-Ferrer, J.M. Hyde, L. Messina, G. Monnet, M.I. Pascuet, B. Radiguet, M. Serrano, L. Malerba, Multiscale modelling in nuclear ferritic steels: from nano-sized defects to embrittlement, Mater. Today Phys. 27 (2022) 100802.
[33] P. Efsing, P. Ekström, Swedish RPV surveillance programs, in: W.L. Server, M. Brumovský (Eds.), International Review of Nuclear Reactor Pressure Vessel Surveillance Programs, ASTM International, West Conshohocken, PA, 2018, pp. 219–231.
[34] P. Efsing, C. Jansson, T. Mager, G. Embring, Analysis of the ductile-to-brittle transition temperature shift in a commercial power plant with high nickel containing weld material, in: J.T. Busby (Ed.), Effects of Radiation on Materials: 23rd International Symposium, ASTM International, West Conshohocken, PA, 2008, pp. 44–55.
[35] P. Efsing, M. Boåsen, D. Klein, P. Arffman, N. Hytönen, S. Lindqvist, M. Thuvander, K. Lindgren, J. Roudén, Barsebäck as a research and development platform, extraction and analysis of service-aged and irradiated reactor pressure vessel material, Roskilde, 2022.
[36] N. Hytönen, Z. Que, P. Arffman, J. Lydman, P. Nevasmaa, U. Ehrnstén, P. Efsing, Effect of weld microstructure on brittle fracture initiation in the thermally- aged boiling water reactor pressure vessel head weld metal, Int. J. Miner., Metall. Mater. 28 (5) (2021) 867.
[37] S. Lindqvist, A. Norrgård, P. Arffman, N. Hytönen, J. Lydman, P. Efsing, S. Suman, P. Nevasmaa, Mechanical behavior of high-Ni/high-Mn Barsebäck 2 reactor pressure vessel welds after 28 years of operation, J. Nucl. Mater. 581 (2023) 154447.
[38] K. Lindgren, P. Efsing, M. Thuvander, Elemental distribution in a decommissioned high Ni and Mn reactor pressure vessel weld metal from a boiling water reactor, Nucl. Mater. Energy 36 (2023).
[39] H. Yuya, K. Yabuuchi, A. Kimura, Radiation embrittlement of clad-HAZ of RPV of a decommissioned BWR plant, J. Nucl. Mater. 557 (2021).
[40] K. Thompson, D. Lawrence, D.J. Larson, J.D. Olson, T.F. Kelly, B. Gorman, In situ site-specific specimen preparation for atom probe tomography, Ultramicroscopy. 107 (2–3) (2007) 131–139.
[41] J.M. Hyde, M.G. Burke, B. Gault, D.W. Saxey, P. Styman, K.B. Wilford, T. J. Williams, Atom probe tomography of reactor pressure vessel steels: an analysis of data integrity, Ultramicroscopy. 111 (6) (2011) 676–682.
[42] B. Gault, M.P. Moody, F. de Geuser, G. Tsafnat, A. La Fontaine, L.T. Stephenson, D. Haley, S.P. Ringer, Advances in the calibration of atom probe tomographic reconstruction, J. Appl. Phys. 105 (3) (2009).
[43] A.J. Breen, A.C. Day, B. Lim, W.J. Davids, S.P. Ringer, Revealing latent pole and zone line information in atom probe detector maps using crystallographically correlated metrics, Ultramicroscopy. 243 (2023) 113640.
[44] J.M. Hyde, A. Cerezo, T.J. Williams, Statistical analysis of atom probe data: detecting the early stages of solute clustering and/or co-segregation, Ultramicroscopy. 109 (5) (2009) 502–509.
[45] F. De Geuser, B. Gault, Metrology of small particles and solute clusters by atom probe tomography, Acta Mater. 188 (2020) 406–415.
[46] B.M. Jenkins, A. Zakirov, F. Vurpillot, A. Etienne, C. Pareige, P. Pareige, B. Radiguet, On the iron content of Mn-Ni-Si-rich clusters that form in reactor pressure vessel steels during exposure to neutron irradiation, Acta Mater. 281 (2024).
[47] Y. Dong, A. Etienne, A. Frolov, S. Fedotova, K. Fujii, K. Fukuya, C. Hatzoglou, E. Kuleshova, K. Lindgren, A. London, A. Lopez, S. Lozano-Perez, Y. Miyahara, Y. Nagai, K. Nishida, B. Radiguet, D.K. Schreiber, N. Soneda, M. Thuvander, T. Toyama, J. Wang, F. Sefta, P. Chou, E.A. Marquis, Atom probe tomography interlaboratory study on clustering analysis in experimental data using the

maximum separation distance approach, Microsc. Microanal.: Off. J. Microsc. Soc. America, Microbeam Anal. Soc., Microscop. Soc. Canada 25 (2) (2019) 356–366.
[48] N. Castin, P. Klupś, M. Konstantinovic, G. Bonny, M.I. Pascuet, M. Moody, L. Malerba, How precisely are solute clusters in RPV steels characterized by atom probe experiments? J. Nucl. Mater. (2024) 155412.
[49] K. Murakami, Influence of copper precipitates on clustering behavior of alloying elements observed in Japanese reactor pressure vessel surveillance materials using atom probe tomography, J. Nucl. Mater. 542 (2020).
[50] Y. Sekio, S. Yamashita, N. Sakaguchi, H. Takahashi, Void denuded zone formation for Fe–15Cr–15Ni steel and PNC316 stainless steel under neutron and electron irradiations, J. Nucl. Mater. 458 (2015) 355–360.
[51] B.N. Singh, Effect of grain size on void formation during high-energy electron irradiation of austenitic stainless steel, Philos. Mag.: J. Theoret. Exp. Appl. Phys. 29 (1) (1974) 25–42.
[52] K. Lindgren, M. Boåsen, K. Stiller, P. Efsing, M. Thuvander, Cluster formation in in-service thermally aged pressurizer welds, J. Nucl. Mater. 504 (2018) 23–28.
[53] K. Lindgren, M. Boåsen, Z. Que, K. Stiller, P. Efsing, M. Thuvander, Post-irradiation annealing of high flux irradiated and surveillance material reactor pressure vessel weld metal, J. Nucl. Mater. 562 (2022).
[54] N. Almirall, P.B. Wells, S. Pal, P.D. Edmondson, T. Yamamoto, K. Murakami, G. R. Odette, The mechanistic implications of the high temperature, long time thermal stability of nanoscale Mn-Ni-Si precipitates in irradiated reactor pressure vessel steels, Scr. Mater. 181 (2020) 134–139.
[55] B.M. Jenkins, P.D. Styman, N. Riddle, P.A.J. Bagot, M.P. Moody, G.D.W. Smith, J. M. Hyde, Observation of Mn-Ni-Si-rich features in thermally-aged model reactor pressure vessel steels, Scr. Mater. 191 (2021) 126–130.

Journal of Nuclear Materials 603 (2025) 155423

Contents lists available at ScienceDirect

Journal of Nuclear Materials

journal homepage: www.elsevier.com/locate/jnucmat

Microscopic characterisation of brittle fracture initiation in irradiated and thermally aged low-alloy steel welds of a decommissioned reactor pressure vessel

N. Hytönen [a,*], S. Lindqvist [a], J. Lydman [a], Y. Ge [a], Z. Que [a], P. Efsing [b,c]

[a] VTT Technical Research Centre of Finland, Kivimiehentie 3, FI-002044 VTT, Finland
[b] Ringhals AB, Väröbacka 43585, Sweden
[c] Department of Solid Mechanics, Royal Institute of Technology (KTH), Stockholm SE-10044, Sweden

HIGHLIGHTS

- Systematic fractography on total of 101 brittle specimens.
- Characterisation on decommissioned RPV welds and surveillance material.
- Two types of initiators identified as weakest links.
- Fracture initiation in impact toughness testing and fracture toughness testing.

ARTICLE INFO

Keywords:
Reactor pressure vessel steel
Brittle fracture
Initiation
Weld metal
Inclusion

ABSTRACT

Microstructure has a significant effect on material's integrity and in a heterogeneous weld microstructure the discontinuities affect the brittle fracture initiation and propagation and determine the fracture toughness. The knowledge of brittle fracture initiation mechanisms in high-Mn/high-Ni welds is limited. The brittle fracture initiation behaviour of the decommissioned Barsebäck Unit 2 reactor pressure vessel (RPV) welds of high-Mn/high-Ni weld metal from three different locations, the RPV head and the beltline regions, were investigated and compared with specimens from the surveillance program with high fluence. Systematic fractography has been performed on impact and fracture toughness specimens and the main features of the brittle fracture initiation in the component weld are presented and discussed. Two main types of initiators are identified as the weakest links to initiate the cleavage fracture and the initiation mechanism is found independent from the operation condition. The high-fluence surveillance specimens have a larger amount of intergranular cracking. The cleavage fracture initiation appears to be independent of the operation conditions but dependent on the welding process and metallurgical features. The findings aid in the development of improved material-property correlations which will result in better computational tools for predicting aging of welds based on microstructure.

1. Introduction

Multi-scale characterisation of reactor pressure vessel (RPV) microstructural features and mechanical properties throughout its lifetime is important to get a comprehensive understanding of the causes and effects on embrittlement and to assist the evaluation of long-term operation. Ferritic metals and welds with body-centred cubic crystal structure experience embrittlement through neutron irradiation and thermal ageing during operation. The radiation-induced embrittlement increases the ductile to brittle transition temperature (DBTT), which is monitored in respect to the lowest possible temperature in the RPV operation to avoid a catastrophic event due to loss of structural integrity [1]. The material embrittlement is monitored through a surveillance programme, in which representative RPV materials are placed in the reactor and irradiated at a higher dose rate and tested periodically to predict the RPV behaviour during operation. The most pronounced thermal ageing

* Corresponding author.
E-mail address: noora.hytonen@vtt.fi (N. Hytönen).

https://doi.org/10.1016/j.jnucmat.2024.155423
Received 24 July 2024; Received in revised form 11 September 2024; Accepted 20 September 2024
Available online 21 September 2024

effect in the RPV welds are elemental segregation to grain boundaries, precipitation and carbides coarsening, hence temper embrittlement [2,3].

In RPV materials the radiation damages the matrix, causing vacancies and interstitials, increasing hardness, and inducing phosphorus segregation to the grain boundaries [4,5]. The hardening is primarily caused by elemental clustering of alloying elements, specifically Mn, Ni, and Si, which pin dislocations and impede deformation [6,7]. On the other hand, phosphorus segregation at the prior austenite grain boundaries (PAGB) diminishes the integrity and increases the susceptibility of intergranular cracking [4]. In terms of thermal ageing effect, additional to the phosphorus segregation, carbide precipitation increases the embrittling effect in low alloy steels (LAS) [8–10].

Irradiation and thermal ageing effects on the microstructure are mainly studied on a nanoscale or in terms of mechanical properties. On the embrittlement and brittle fracture initiation, the common understanding is that the cleavage fracture initiates at secondary-phase particles in LASs [11]. In bainitic base material, the weakest link is typically a carbide or a precipitate whereas in welds it is more often a non-metallic inclusion [12–15]. However, a systematic fractographic investigation on tested specimens has rarely been made for a specific material or the studies may not be conclusive. Weld metals have a heterogeneous microstructure with specific features from nano- to macroscale, which form during subsequent solidification and heat treatment during weld passes and result in formation of microstructurally and mechanically different zones. However, the effects of the different microstructures, the weld procedure, and the weld passes on fracture toughness are not well understood, whether radiation and thermal ageing affect brittle fracture initiation, and what factors affect brittle fracture. Combining the mechanical behaviour with metallurgical features from macroscopic scale to microscopic scale enables further understanding of the factors affecting brittle fracture initiation and crack propagation.

The multi-pass LAS weld metal consists of multiple weld beads with specific fan-shaped columnar microstructure and equiaxed reheated regions. The grains include relatively large amounts of non-metallic inclusions. In terms of structural integrity and the occurrence of weld defects, weld metals are often considered more critical than base materials due to the higher density of inclusions and higher level of solute elements segregation to grain boundaries [16]. All these features, multi-pass weld microstructure and inclusions, influence the structural integrity, but the combined micromechanical effect remains unclear. In terms of microstructure and thermal history, component welds are inherently heterogeneous and require a comprehensive understanding of the material homogeneity. In the integrity assessment of material in long-term operation, the homogeneity assessment is a significant part of an extensive study, and a large database is needed to support the ageing management.

In this study, different welds from the same decommissioned RPV are investigated and compared. The Barsebäck Unit 2 (B2) RPV was in operation for 23 effective full power years. The weld metal in the B2 RPV is relevant to the other Nordic operating boiling water reactor (BWR) nuclear power plants (NPP), which are manufactured utilizing the same materials and manufacturer. A high-Ni and high-Mn weld metal has been studied earlier from other reactors [17,18], however, in the current study, a unique opportunity to study both thermally aged and irradiated component welds and surveillance material was created. An extensive investigation has been conducted on the decommissioned B2 materials, including experimental work from macro- to nanoscale. Lindqvist et al. studied the mechanical properties of the decommissioned component weld in comparison to the surveillance data [19], finding difference in toughness properties between the axial beltline weld compared to the RPV head and circumferential beltline welds and to the surveillance welds. According to the study, the differences in mechanical properties possibly originate from variations in post weld heat treatment (PWHT) temperature and time. Additionally, the study concluded that no thermal embrittlement is identified based on the DBTT curve. The microstructure and fractography of the RPV head weld have been reported in relation to the impact toughness properties and fracture toughness properties, concluding the primary initiation occurs from a non-metallic inclusion [20,21]. Additionally, the brittle fracture initiation was assessed using crystal plasticity modelling. Preliminary characterisation and mechanical properties of the B2 non-aged baseline surveillance material have also been investigated and reported by Sirkiä et al. [22]. Lindgren et al. conducted study for the same weld metal by atom probe tomography (APT) to analyse the MnNiSi clustering [23]. Tendencies as early-stage clustering was observed of Ni, Mn, Si, and Cu, and further investigation on the clusters is ongoing. Additionally, weakest link modelling has been developed in conjunction with the brittle fracture studies [24,25]. This paper aims to summarize the microstructural characterisation and systematic fracture surface analysis of all studied welds for concluding the effect of microstructure and the effect of operation conditions to the brittle fracture initiation in a RPV weld.

Specimens from three different RPV weld seams of the decommissioned B2 reactor, one from the RPV head and two from the beltline region, were extracted and investigated for structural integrity, and compared to two surveillance chain materials. The RPV head weld is considered non-irradiated but thermally aged and the two beltline welds, axial and circumferential, are considered both irradiated and thermally aged, where the axial weld has been subjected to a higher dose, being closer to the maximum fluence area from the core, than the circumferential weld. The two surveillance chains are from the dedicated and representative surveillance program. The first surveillance chain represents a dose close to the axial beltline weld at the time of the shut-down of the reactor, and the second chain represents an accelerated irradiated state of at least 60 years of operation. Unirradiated and non-aged baseline material has been characterised earlier as well [22]. All welds are post-weld heat treated and the documentations were reviewed. In this paper, the main microscopic features of the brittle fracture initiation properties in decommissioned component weld are presented, discussed, and compared to the surveillance specimens.

2. Experimental methods and materials

2.1. Materials

The investigated material is from the decommissioned B2 NPP. The base material is plate SA533 Gr. B Cl. 1, and the LAS welds are manufactured using submerged arc welding with weld wire containing high Mn and Ni and low Cu alloying. The RPV welds are double U-groove welds with root weld removed, and in the RPV head only the ~16 mm of the outermost build-up was welded using manual metal arc welding technique due to the component geometry. The welds have been subjected to a PWHT; after welding a direct treatment at 575 °C for minimum of 15 min, and a final PWHT at 620 ± 15 °C for 5.5 h. The B2 specific surveillance material is submerged arc welded using the same weld wire as the RPV welds and manufactured at the same time, however, the weld PWHT at approximately 610 °C is as long as ~10 h.

Material from three weld locations was obtained in the form of trepan cuts and the inner wall side cladding was removed. The specimens for mechanical testing and fractography were extracted from ¼T of the wall thickness and the metallographic microstructure was studied through wall thickness. The locations are an RPV head weld (RPVHW), an axial beltline weld (ABLW), and a circumferential beltline weld (CBLW). The chemical composition of the welds was measured using optical emission spectroscopy technique, shown in Table 1.

The conditions of the different investigated weld metals and the number of analysed fracture specimens are specified in Table 2. The RPVHW is considered as thermally aged (TA), being subjected to temperature of ~288 °C. The two welds at the beltline region studied are irradiated (IR) at slightly below ~270 °C, where the ABLW is located at

Table 1
Chemical composition of the three component welds in wt.-%.

Weld	C	Mn	Ni	Si	Mo	Cr	S	P	Cu	Al	Ti	Co
RPVHW	0.057	1.43	1.48	0.15	0.41	0.03	0.007	0.008	0.060	0.024	0.003	0.020
CBLW	0.083	1.45	1.54	0.17	0.45	0.04	0.006	0.008	0.087	0.086	0.002	0.018
ABLW	0.075	1.43	1.63	0.17	0.44	0.03	0.007	0.010	0.091	0.025	0.001	0.018

Table 2
List of studied welds and their conditions, reference transition temperatures, and number of investigated brittle fracture test specimens for fractography per weld.

	RPVHW	CBLW	ABLW	SCW	SGW
Condition	TA	IR	IR	IR	IR (accel.)
Neutron fluence [n/cm^2]	–	2.9 × 10^{16}	7.9 × 10^{17}	1.02×10^{18}	5.87×10^{19}
Reference temperature T41J [°C]	−75	−70	−95	–	–
Reference temperature T0 [°C]	−115	−92	−102	−113	81
Number of tested specimens	9 CVN 20 mini-C(T)	9 CVN 15 mini-C (T)	9 CVN 12 mini-C (T)	- 12 mini-C (T)	- 12 mini-C (T)
Number of tested specimens	9 CVN 20 mini-C(T)	9 CVN 15 mini-C (T)	9 CVN 12 mini-C (T)	- 12 mini-C (T)	- 12 mini-C (T)

the level of the reactor core centre line and was subjected to the maximum fluence, which is approximately 8 × 10^{17} n/cm^2. The laboratory-measured activity of the ABLW is 40.8 MBq. The CBLW is located a little higher from the reactor core and was subjected to lower fluence of 2.9 × 10^{16} n/cm^2.

Weld specimens from two different surveillance chains have been studied in comparison to the component welds. The surveillance chain C weld (SCW) was subjected to average neutron fluence ($E > 1$ MeV) of 1.02×10^{18} n/cm^2 and the surveillance chain G weld (SGW) represents an accelerated irradiation state at average neutron fluence of 5.87×10^{19} n/cm^2. The subjected fluences can be estimated that 7 × 10^{20} n/cm^2 is approximately 1 dpa, therefore, the component welds are in the scale of 1 mdpa, and the surveillance welds in the scale of 0.01 dpa and 0.1 dpa [26].

2.2. Experimental methods

The metallography specimens were polished and etched with 3 % Nital solution and the microstructure analysed using Zeiss Axio Observer 7 inverted light optical microscope (LOM). For more detailed weld solidification microstructure analysis, the specimen was repolished using the Buehler MiniMet 1000 and MasterMet 2 colloidal silica suspension. The microstructural analysis was done using Zeiss Crossbeam 540 scanning electron microscope (SEM) equipped with EDAX Hikari Plus electron backscatter detector (EBSD) to obtain the inverse polar figure (IPF) map with TSL OIM Analysis 8 software. The fracture surfaces were imaged using the SEM and the local elemental composition analysed using EDAX Octane Plus energy dispersive X-ray spectroscopy (EDS). The hardness measurements HV10 and HV1 were measured using a Struers DuraScan-80 device. The general inclusion analysis was done on the SEM-EDS using Genesis software, and the further investigation was done using FEI Talos F200x transmission electron microscope (TEM) with Super-X EDS system.

The fractography was performed on fracture mechanical specimens that were tested for impact toughness and fracture toughness. The impact toughness properties were tested using Charpy V-notch (CVN) specimens according to EN ISO 148 [27] and ISO 14,556 [28] standards. The fracture toughness properties were examined using the Master curve method on miniature compact tension (mini-C(T)) specimens of 0.16T according to ASTM 1921 [29]. The testing is done according to the effective version of the standard and previous analyses are updated accordingly. The studied CVN specimens were from the lower transition region of the DBTT curve below 41 J in temperature range of –120 °C to –75 °C, which is a total of 9 specimens per tested component weld, i.e., the three conditions totalling 27 CVN specimens. Of all five conditions, the mini-C(T) specimens were tested in the brittle region, which is total of 12–20 specimens per tested weld, hence a total of 74 mini-C(T) studied specimens. The fracture toughness testing for the component welds was performed in a temperature range from –146 °C to –114 °C, for SCW in a range of –100 °C to –130 °C, and for SGW of 27 °C to 120 °C. The reference T_{41J} temperatures and T_0 for the investigated materials are presented in Table 2, while further details about the testing have been reported by Lindqvist et al. [19].

3. Results

3.1. Microstructural characterisation

The microstructure of the multi-pass weld metal can be divided into at least four major macrostructures, i.e., as-welded and reheated regions, multiple times reheated regions, and remelted regions. The most evident regions are the as-welded and the reheated regions. The as-welded region has columnar dendritic microstructure growing in the direction of the weld pass solidification forming the fan shape. The columnar grains consist of acicular ferrite and intercolumnar grain boundary ferrite. When subsequent weld passes solidify, the remelting and reheating cause part of the previous weld bead microstructure to recrystallise forming equiaxed grains of polygonal ferrite. In Fig. 1, the microstructure of the ABLW close to the inner wall side is shown. Fig. 1 (a) shows multiple weld passes, and one as-welded and reheated zone is shown in Fig. 1(b). One weld bead is in a size of ~2.3–4 mm. In Fig. 1(c, d), the as-welded microstructure with a small sub-grain structure of acicular ferrite and larger empty grains of grain boundary ferrite are indicated, and in Fig. 1(e, f), the reheated microstructure with polygonal ferrite and acicular ferrite are indicated. In Fig. 2, the EBSD map represents the as-welded microstructure separating the different columnar grains by colour codes based on grain orientation. The fine complex structure of acicular ferrite appears evidently among the long empty grains adjacent to the columns which are grain boundary or polygonal ferrite. The dominating microstructure is acicular ferrite and is desired due to its high toughness properties.

The macrohardness profiles were measured for the RPV component welds through the wall thickness from the inner wall side to the outer wall side. As shown in Fig. 3, the hardness trends appear relatively homogeneous and only a mild increase in the trend can be seen at the intersection of weld deposition directions. The level of hardness remains within the accepted range for the LAS weld metal, but it is considerable how the hardness differs between the three investigated welds. The average hardness values with standard deviation are given in Table 3. The effect of weld bead structure was investigated, dividing the indentations based on as-welded and reheated regions, however, the microstructural features showed no significant effect on hardness. The microhardness was measured using HV1 for all welds, including the surveillance mini-C(T) specimens side surfaces. The microhardness

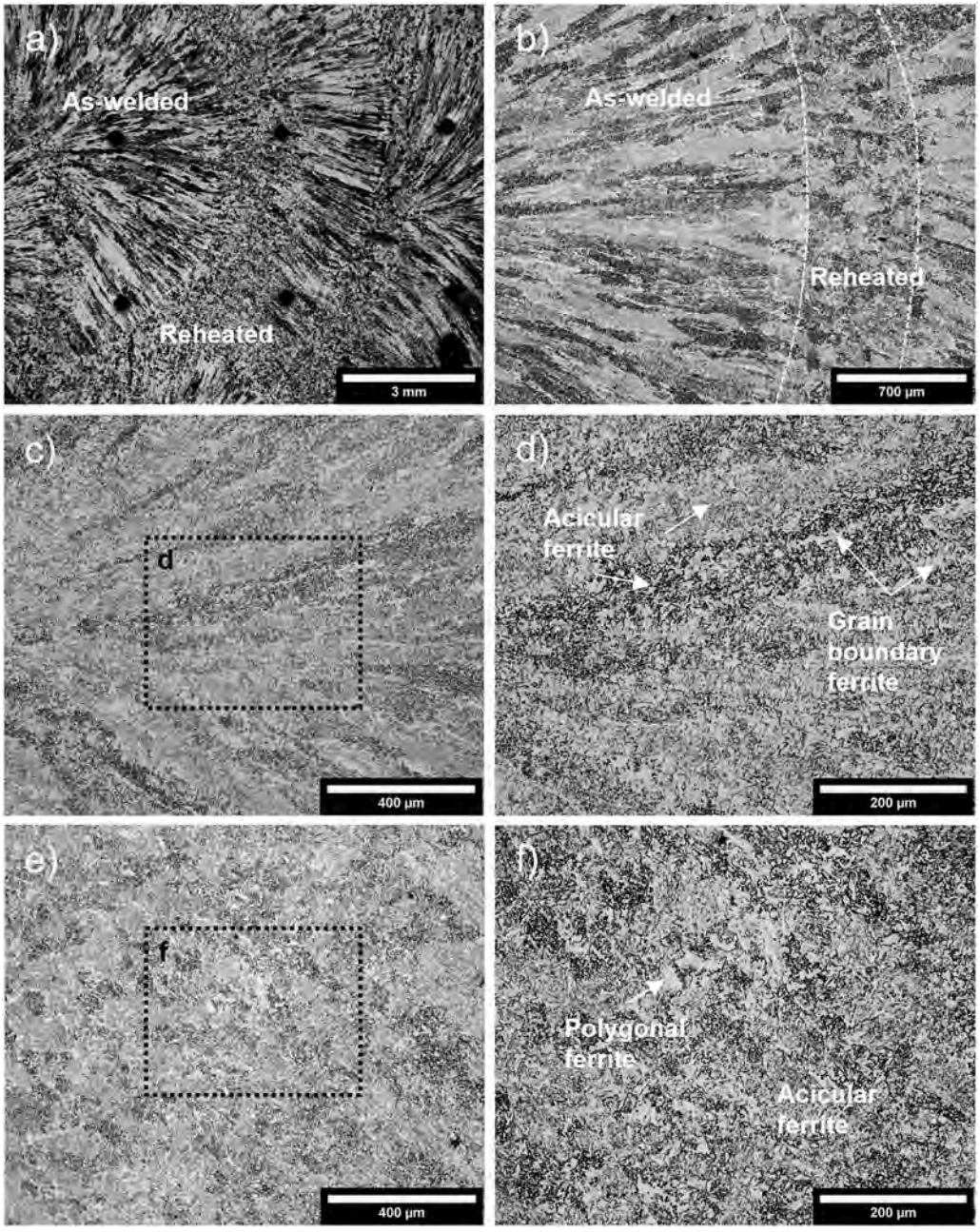

Fig. 1. Metallographic microstructure of the multi-pass weld of ABLW, showing the as-welded and reheated regions and the ferrite structure.

levels follow the trend of the macrohardness and expectedly the SGW gives the highest hardness of 297 ± 5 HV1 while the SCW hardness is lower at 217 ± 5 HV1 and more comparable to the component welds.

3.2. Fractography

The fracture surfaces of all brittle specimens were investigated systematically, as both mating surfaces of each broken specimen were analysed. The amount of analysed fracture surfaces in this complete investigation gives a relatively quantitative perspective of the brittle fracture initiation in the heterogeneous welds. As shown in Table 2, from each three RPV component welds there are sets of brittle CVN and mini-C(T) specimens and two sets of surveillance weld mini-C(T) specimens, totalling 101 brittle fracture specimens that have been analysed.

The primary initiation site can be found by following the river patterns typical for cleavage fracture. In general, the macro patterns lead to the primary initiation area, and on closer imaging, the micro patterns can be used to track the primary initiation site. In LAS weld metal, typically an inclusion is found at the primary cleavage fracture initiation site. Once the primary initiation site is identified and imaged, the local chemical composition is analysed using EDS point analysis and mapping to obtain further information on the inclusion and the features in the fracture initiation area. In most cases, the interaction volume is slightly larger than the inclusions, which affects mainly the point analysis performed on the inclusion. Mapping the initiation area, other adjacent inclusions and features could be observed with improved clarity. The summary of the number of specimens and primary initiation site inclusion analysis results are given in Table 4. The table includes a description of specimen type and number of brittle specimens in fractography. The inclusion types are indicated based on the main chemical elements of the inclusion, and the occurrence is the number of all analysed specimens per inclusion type. The inclusion size is an approximate

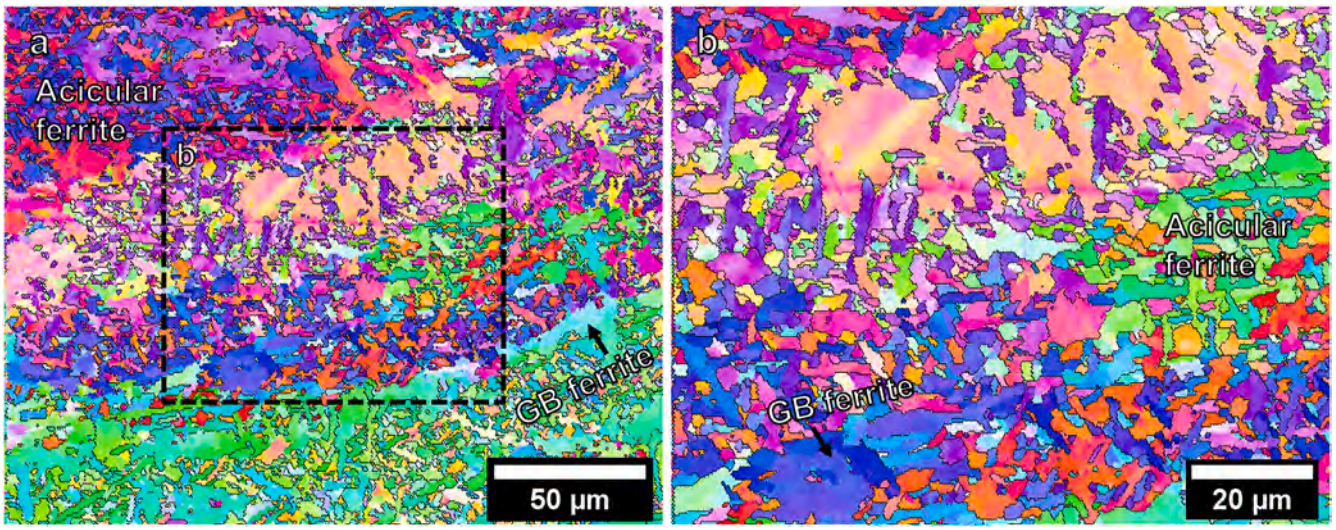

Fig. 2. EBSD analysis of the as-welded microstructure of the ABLW, demonstrating the complex grain structure in the weld. Areas with acicular ferrite and grain boundary (GB) ferrite are indicated in the figures.

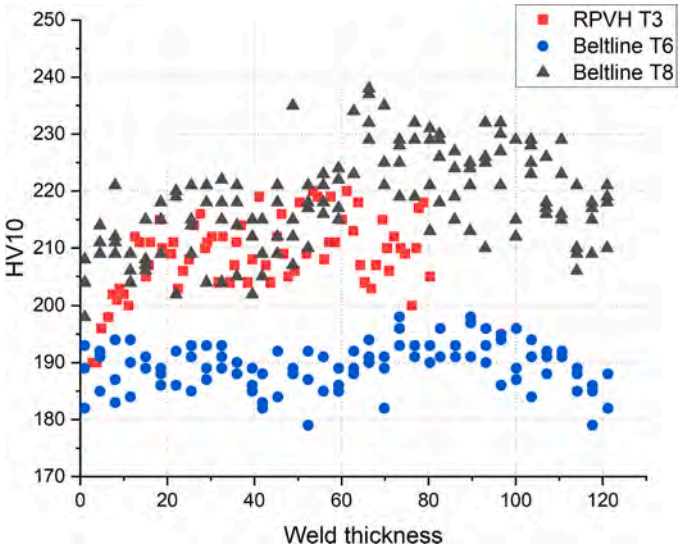

Fig. 3. Macrohardness HV10 through the wall thickness of the three component welds, where the 0-mm is the inner wall side.

Table 3
Measured hardness HV10 and HV1 averages and standard deviations of the welds.

Weld	HV10	HV1
RPVHW	211 ± 5	227 ± 5
CBLW	218 ± 9	234 ± 8
ABLW	190 ± 4	199 ± 5
SCW		217 ± 5
SGW		297 ± 5

diameter, and the integrity of the initiation site or the inclusion is described as broken or debonded. For nearly all specimens the dominating fracture mode was an inclusion-initiating cleavage fracture except in the high-fluence SGW five specimens, which had intergranular (IG) cracking as dominating fracture mode and no primary initiators were identified.

In the investigated weld fracture surfaces, two types of particles are found at the initiation sites. In most of the specimens, the initiators are roundish multiphase oxide inclusions with a chemical composition including mainly Al, Si and Mn and sometimes with small amounts of Ti, S, or Mo. The inclusion itself can be either broken, when the primary crack has initiated within the inclusion, or intact and debonded from the metal matrix, where the primary crack has initiated from breaking the inclusion-matrix interface. On the intact debonded oxide inclusions, some surface pattern is observed, and the inclusion remains on one half of the specimen while the mating surface only has a dent at the location of the inclusion. On the broken oxide inclusions, layered and/or internal structure can be observed, and the inclusion halves are on both mating surfaces of the specimen. In the irradiated material, some of the oxide inclusions appeared to be somewhat deformed and elongated as well.

The second particle type found are Mn-rich particles with small amounts of S and Mo based on SEM-EDS analysis with mild peak of C in the spectrum and relatively significant amount of Fe. The SEM-EDS spectrum indicates that the composition of the Mn-rich particle could be a Mn-Mo-containing carbide, where the Mn replaces the Fe. Further analyses are required to fully study these particles, also due to their relatively large size. A preliminary TEM-EDS analysis showed indications of nitride and no carbon, and only nanoparticles of S and Mo are found, however, further confirmation is required using TEM. Due to the uncertainty, these particles are referred to as Mn-rich particles. The morphology of these particles differs from the oxide type, as the Mn-rich particles have an irregular shape and are always broken, and they can be found on both mating surfaces. The crack plane is smooth, and no internal structure is observed. In all primary initiation sites with a Mn-rich particle, the main fracture type is cleavage fracture, however, a small amount of IG fracture surface adjacent to the initiation site is observed.

In the case of the Mn-rich particles EDS spectra, there is a strong peak at 2.3–2.5 keV where the Mo and S overlap. The overlap is also in the EDS map which needs to be considered, as there may be an error in the intensity of one of the elements. The Mo-content was confirmed using high acceleration voltage on EDS to acquire the K-line at ~17.4 keV, but the presence of S was more challenging to determine. Wavelength dispersive X-ray spectroscopy (WDS) was used, and an indication of S was found, although the concentration is relatively low. The low concentration of S indicates, however, that the Mn-rich particles is not a sulphide. The EDS chemical composition result is semi-quantitative, and the interaction volume is larger than the inclusion giving some background error to the result. The EDS analysis still gives a good indication of the elements present in the inclusion and initiation site. Further investigation using TEM will be made to determine the full composition and complexity of these particles.

Table 4
Summary of brittle fracture initiation types for the studied 101 specimens of the different welds.

Weld	Specimen type	Number of specimens	Initiator type and occurrence		Size range (μm)	Initiation site integrity and occurrence	
RPVHW	CVN	9	AlSiMnO	9/9	0.5–2.2	Debonded Broken	7/9 2/9
	mini-C(T)	20	AlSiMnO	20/20	0.3–1.8	Debonded Broken	13/20 7/20
CBLW	CVN	9	AlSiMnO	9/9	0.7–2.5	Debonded Broken	3/9 6/9
	mini-C(T)	15	AlSiMnO	15/15	0.8–2.2	Debonded Broken	4/15 10/15
ABLW	CVN	9	AlSiMnO Mn-rich	7/9 2/9	1.0–2.3 ~1–2	Debonded Broken	3/9 4/9
	mini-C(T)	15	AlSiMnO Mn-rich	3/15 11/15	0.2–1.0 ~0.5–2	Debonded Broken	3/15 10/15
SCW	mini-C(T)	12	AlSiMnO Mn-rich	2/12 10/12	1.2 ~0.5–2	Debonded Broken	2/12 10/12
SGW	mini-C(T)	12	Mn-rich 5 IG	7/12	~0.5–2	Debonded Broken	0 7/12

For the RPVHW and CBLW, on both CVN and mini-C(T) specimens, the only primary initiation site inclusion type is the AlSiMn-oxide inclusions. In Fig. 4, a fracture surface and a typical non-metallic oxide inclusion at an RPVHW mini-C(T) specimen initiation site are shown. The inclusion is debonded from the metal matrix and the inclusion appears intact. Near the initiation area, some interdendritic (ID) -like fracture surface is observed in addition to the dominating cleavage fracture. The ID-like fracture surface presumably correlates with the as-welded dendritic microstructure.

For the ABLW, in seven out of nine CVN specimens, the fracture

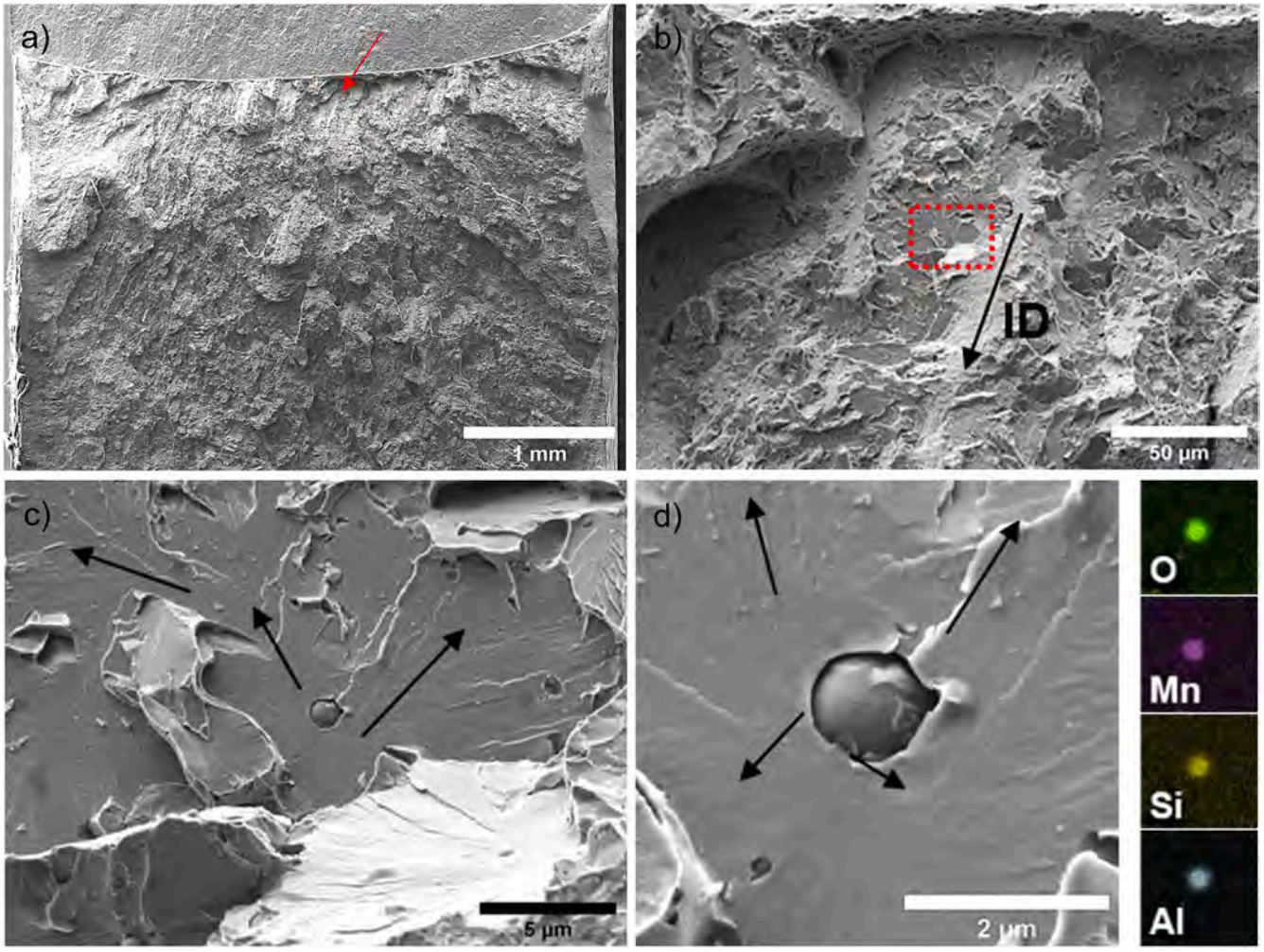

Fig. 4. Fracture surface analysis and a typical primary initiation site of a mini-C(T) specimen which is seen in RPVHW and CBLW with a non-metallic oxide inclusion with main elements of Mn, Si, Al, and O.

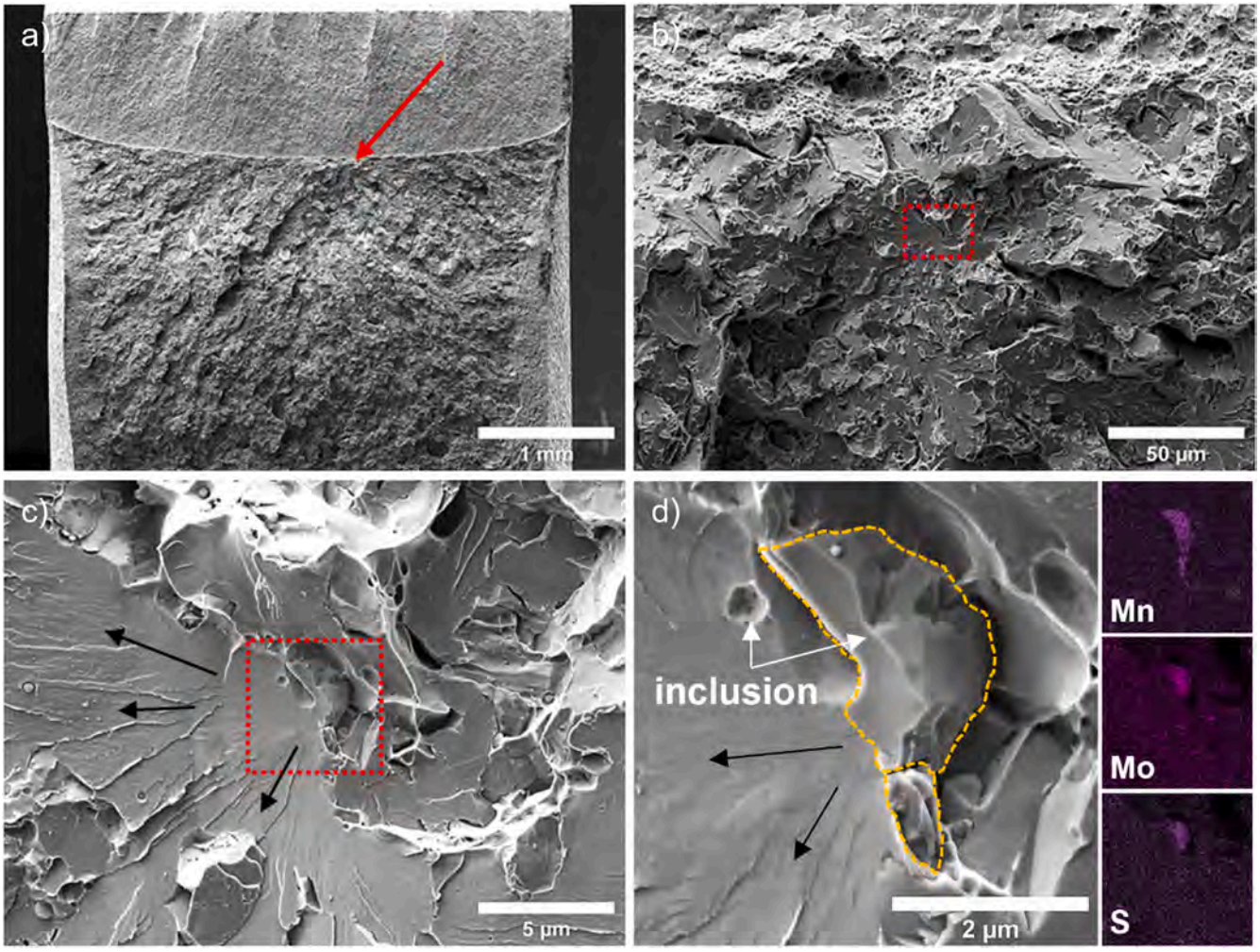

Fig. 5. Fracture surface analysis and a typical primary initiation site of a mini-C(T) specimen in ABLW with a Mn-rich particle. On SEM-EDS, also indications of Mo and S were detected.

initiated from an oxide inclusion and additionally two from Mn-rich particles, and in mini-C(T) specimens eleven out of fifteen initiated from Mn-rich particles and only three from an oxide inclusion. For one mini-C(T) specimen, an inclusion at the primary initiation site could not be conclusively identified but it is suspected to also be a Mn-rich particle, however, it remains uncertain. In Fig. 5, a typical Mn-rich irregular-shaped particle at an ABLW specimen is indicated and the broken inclusion is outlined in yellow to highlight the inclusion from the matrix. The inclusion crack surface appears very smooth, and part of the inclusion grows into the matrix. In the EDS maps, the Mo and S appear in a large area, however, at the 15 kV acceleration voltage their signals overlap, and the amount of both elements need to be critically considered.

Comparing the brittle fracture initiation in the component welds to the surveillance specimens, the surveillance specimens show similar primary initiation sites but with more complexity and variety. On the surveillance weld mini-C(T) specimens, only two of twelve SCW specimens initiated from an oxide and ten from a Mn-rich particle, and the seven SGW specimens with cleavage fracture initiated from a Mn-rich particle. In the SCW, most of the primary initiation sites have a Mn-rich particle as an initiator and only two debonded oxide-inclusions are found. In the SGW, all specimens with a cleavage fracture initiation have a Mn-rich particle, but for five specimens the main fracture mechanism is IG cracking, and no primary initiation site could be determined. In total from the surveillance specimens, there are seven specimens, where there are both Mn-rich particles and AlSiMn-oxide inclusions adjacent to each other at the initiation site. However, the cleavage fracture river patterns lead to the Mn-rich particle, indicating it got fractured prior to the oxide. Fig. 6 shows an example of such an initiation site with both types of particles at the initiation site adjacent to each other. In the figure, the irregular-shaped Mn-rich particle is outlined in yellow and the round oxide inclusion is in orange. There are also smaller inclusions of both types very close to the initiation site, which are also highlighted, and they appear in the EDS maps, yet their influence on the brittle fracture initiation is not confirmed. The EDS spectra in Fig. 6(e) shows the elemental peaks at the indicated locations, i.e., the spot 1 is for the oxide and the spot 2 is for the Mn-rich particle.

In Fig. 7(a), the overall fracture surface of one of the high-fluence SGW specimen is shown. The red arrow indicates the primary cleavage fracture initiation area, and the white arrows indicate the ID crack propagation which presumably aligns with the as-welded dendritic microstructure. The primary initiation area is shown in Fig. 7(b–d), where a transgranular (TG) cleavage fracture initiates from a yellow-outlined Mn-rich -type particle but adjacent to it open large IG areas, which are outlined in yellow.

A typical size of the inclusion at a primary initiation varies between the specimen type and tested weld. In CVN specimens in all welds, the most common oxide inclusions have a diameter of ~1 µm, whereas those in the mini-C(T) specimens the most common inclusion size is ~0.8 µm. Hence, the oxide inclusions at the primary initiation sites in CVN specimens are larger than those in the mini-C(T) specimens. Due to the irregular shape of the Mn-rich particles, their true size is difficult to

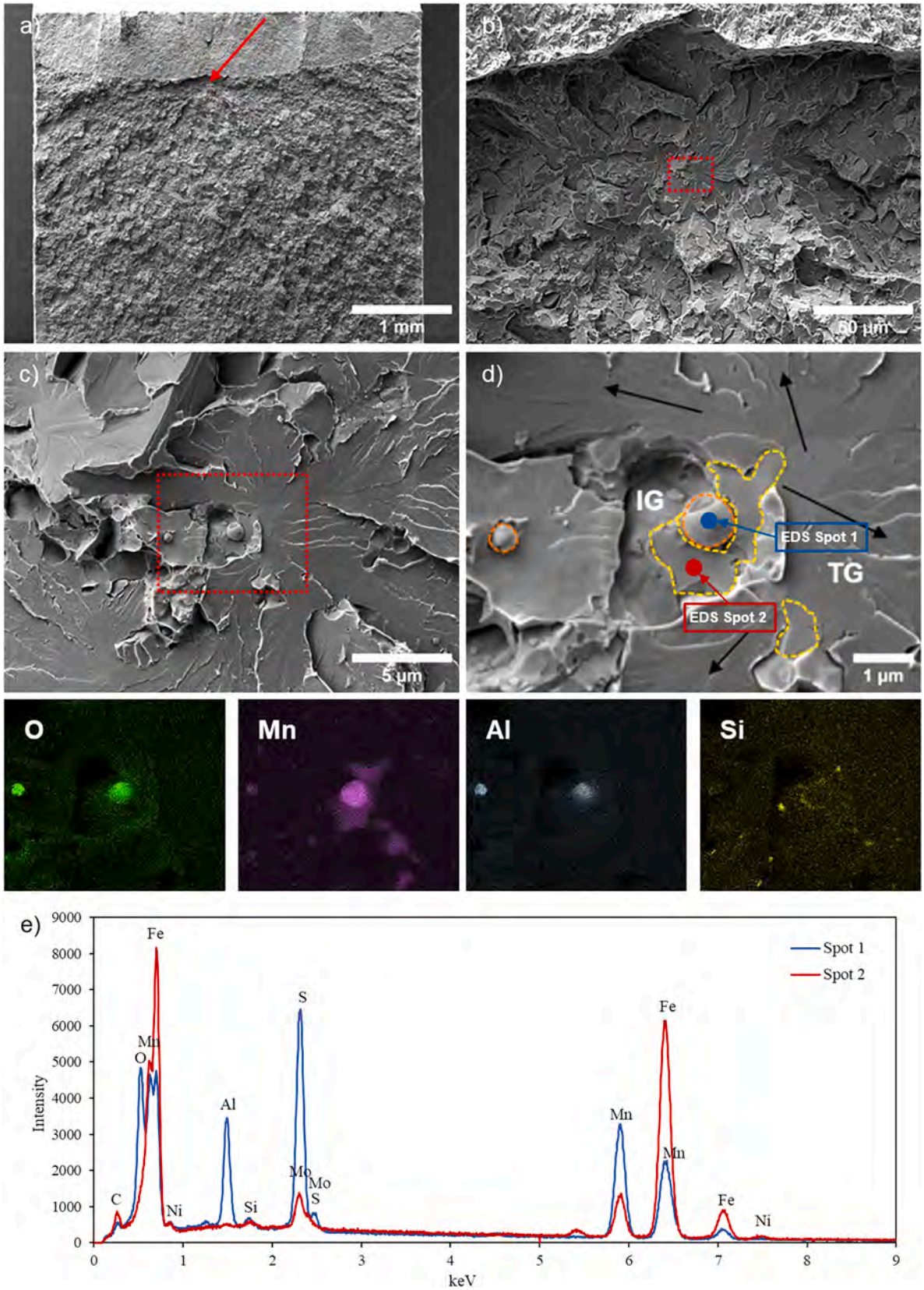

Fig. 6. Fracture surface and a typical primary initiation site of a mini-C(T) specimen in SCW with both oxide and Mn-rich particles with an EDS spectrum of both initiators. The cleavage fracture initiates from the Mn-rich inclusion. Another small oxide inclusion appears on the left of the EDS map.

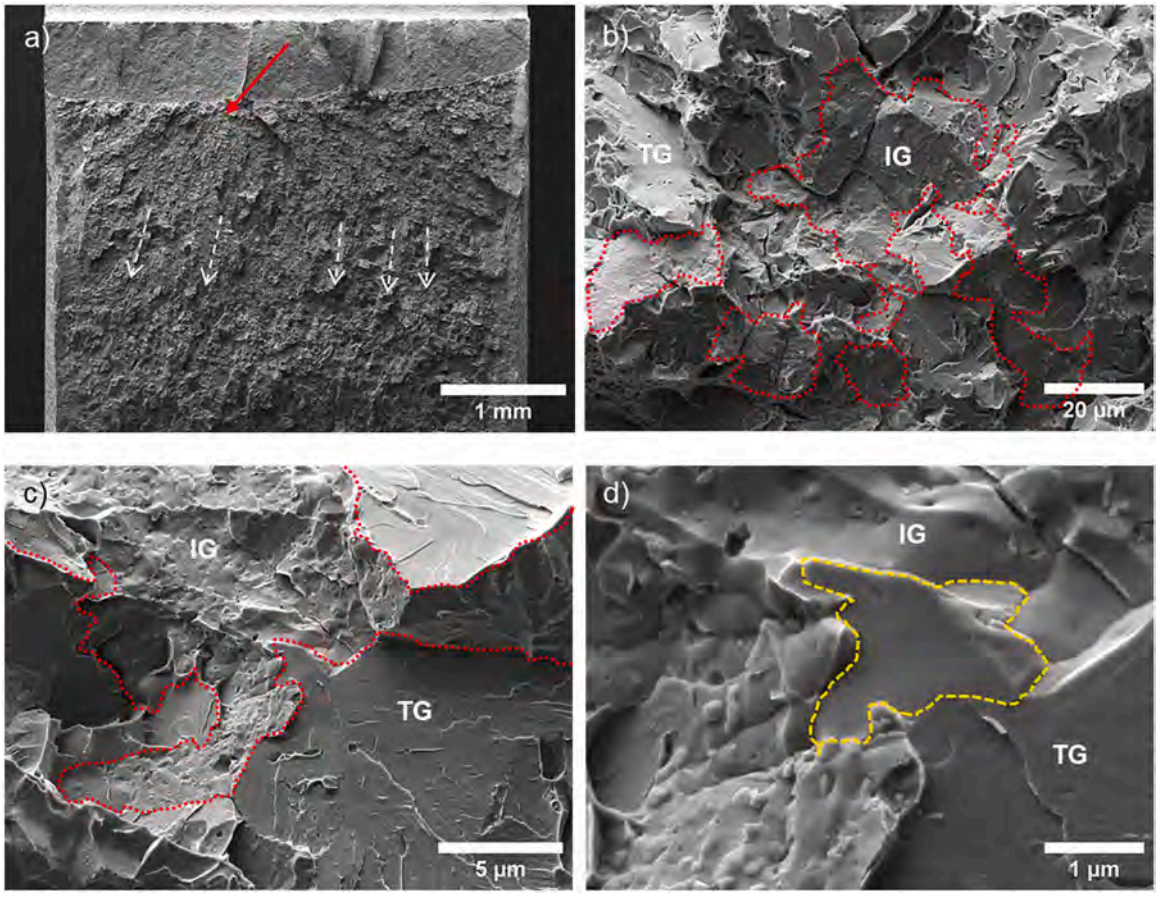

Fig. 7. Fracture surface and initiation site of a high-fluence SGW mini-C(T) specimen. (a) Primary initiation is indicated and further the as-welded columnar structure can be observed from the fracture appearance. (b, c) A large area of IG cracking is surrounded by TG cracking. (d) The cleavage fracture has initiated from a Mn-rich particle outlined in the figure.

determine and therefore the comparison to the oxide inclusions is only indicative. However, the approximate size of the irregular-shaped particles is determined in this paper by taking the width and height of the visible part and calculating the average. The visible size of the Mn-rich particles is in the range of ~0.5–2 µm.

3.3. Inclusion analysis

Since the inclusions appear to have a major influence on the microstructure and the brittle fracture initiation, a further inclusion analysis was performed to improve understanding of the size and distribution of the inclusions in the weld. An analysis was performed for the ABLW polished specimen using an SEM-EDS -based image analysis software. An area of 4 104 μm^2 on the magnification of 1 500× was analysed separately for the as-welded region, identifying 2 879 inclusions, and for the reheated region, identifying 1 709 inclusions. The result for the ABLW metal showed that the most probable non-metallic oxide inclusion is 0.15–0.20 µm in diameter and the identified composition is AlSiMn(S)O. The result is very similar to the analysis done for the RPVHW, for which the most probable size of an oxide inclusion was reported to be ~0.20–0.30 µm [20]. The method for the inclusion analysis is based on image contrast by secondary electrons. However, the analysis does not detect for example nitride inclusions due to the limitations of EDS technique, and therefore the inclusion size distribution result indicates only the density of oxide and sulphide inclusions. In the preliminary advanced analysis using TEM, a typical ~0.2-µm layered oxide inclusion in the weld metal was observed, shown in Fig. 8. Similar type of oxides are presumably found as brittle fracture initiators but in larger size. The detected inclusion has a MnS core with Si-Al-Ti-oxide layers on top. Nano-sized Mo-precipitates appear on the outer layer and a small Mn-N precipitate near the core is detected as well.

4. Discussion

4.1. Brittle fracture initiation

The multi-pass weld has a complex microstructure consisting of several different regions and features from macroscale to nanoscale. The few-millimetre sized fan-shaped weld beads consist of as-welded regions and reheated regions. The main microstructure in the as-welded region consists of columnar (dendritic) grains with acicular ferrite substructure with minor amounts of grain boundary ferrite, and in the reheated regions the polygonal ferrite dominates with some acicular ferrite, as seen in Fig. 1. In LAS, when the austenite cools down, ferrite nucleates at the grain boundaries and grows inward [30]. At a lower temperature in the cooling, in the interior of the prior-austenite, acicular ferrite nucleates at the non-metallic inclusion particles and the growth of the short needle structure is competitive to the grain boundary ferrite. Acicular ferrite has good toughness properties and is the eligible microstructure for the weld [31,32]. The complex microstructure gives a high resistance to crack propagation while large areas of grain boundary ferrite may provide an easy crack propagation path. To obtain acicular ferrite microstructure, non-metallic inclusions are required for the acicular ferrite nucleation during weld solidification [33,34]. These oxide inclusions are typically multi-phase layered inclusions containing mainly elements Mn, Si, Al, and Ti, which all form oxides, hence act as deoxidants in the weld [35,30]. Additionally, Mn reacts readily with S

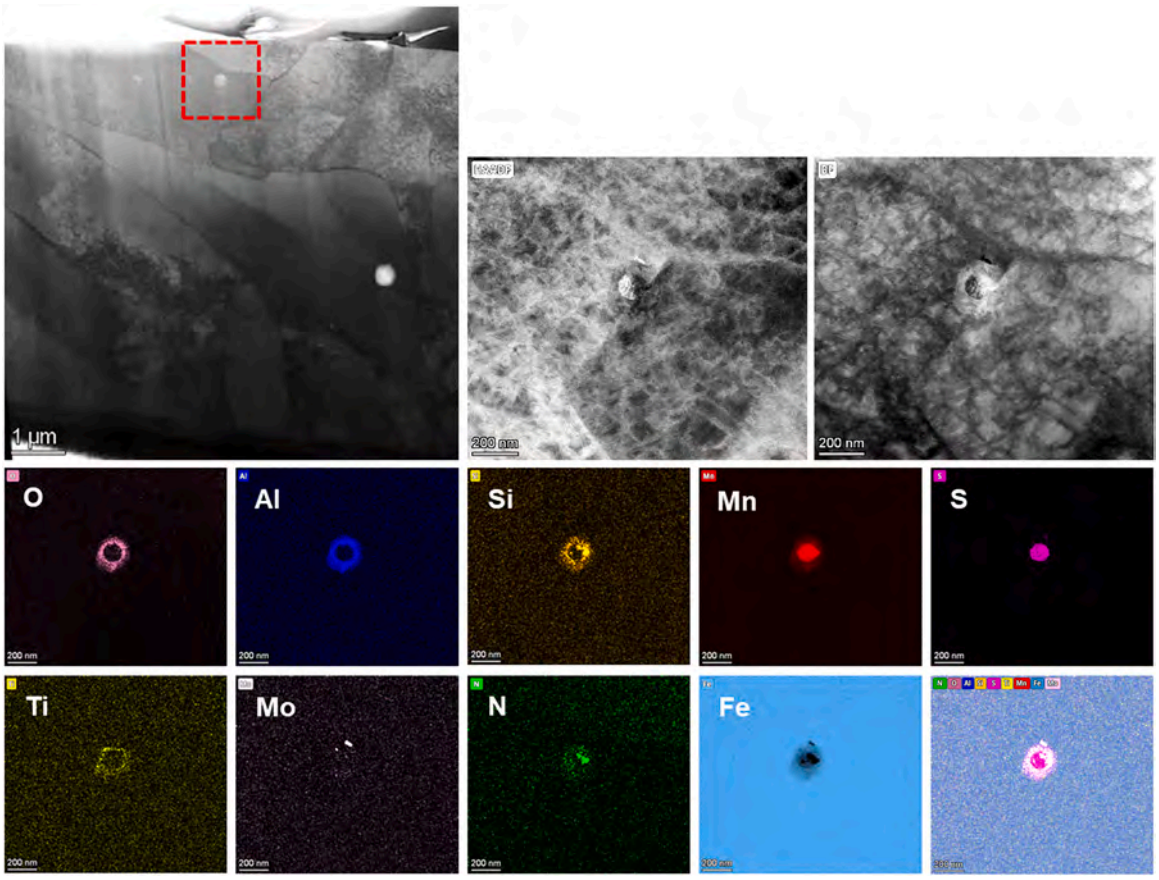

Fig. 8. TEM-EDS analysis of a typical non-metallic inclusion with layered structure of MnS-AlSiTi-O. The inclusion size is typical ~0.2 µm in diameter.

forming MnS acting as desulfurant in the weld. These inclusions, especially the oxides, are of utmost importance in nucleating acicular ferrite [31].

The general inclusion size-distribution analysis has been done for the RPVHW [20] and for the ABLW, where for the most probable size of an oxide inclusion is ~0.2 µm in diameter. The relatively large quantity of the oxide inclusions promotes the nucleation of acicular ferrite and Mn is metallurgically relevant improving the metals toughness properties. However, the large-sized (~0.5–2.5 µm) inclusions appear to act as weakest links for brittle crack initiation, as shown in Figs. 4 and 5. Two main types of inclusions have been identified at the primary initiation site and they are divided as i) a roundish multiphase oxide inclusion and ii) an irregular-shaped Mn-rich particle.

In the literature, brittle oxide inclusions are typically considered as weakest links in welds [11,13], and this is the case for all investigated specimens of the RPVHW and the CBLW. However, in the ABLW, SCW, and SGW, the Mn-rich particles are more frequently found at the initiation site. At both types of initiation locations, the main crack propagation type is cleavage fracture, although in the second case with a Mn-rich particles some grain boundary cracking is observed adjacent to the initiation site, and in the SGW relatively large amount of IG cracking is observed. However, since the oxide inclusions are typically related to the acicular ferrite nucleation, they are most probably found inside the prior austenite grains and do not readily involve IG cracks [36]. The Mn-rich particles on the other hand, might be located at the PAGBs, involving IG cracking on a higher probability, however, is yet to be confirmed. The PAGBs are known to be weak in terms of structural integrity and ageing increases the susceptibility [4,17].

In the SCW, in several specimens both an intact AlSiMn-oxide inclusions and Mn-rich particles were adjacent to the primary initiation site with small amount of IG fracture surface. The cleavage fracture river patterns lead to the Mn-rich particle. Therefore, at such a primary initiation location, the cleavage fracture is considered as the main crack propagation type and the Mn-rich particle is the primary initiator, because the IG area is relatively small, and the IG crack propagation area is outlined by ductile deformation. The small IG area adjacent to the inclusion is also observed to be on a different level from the main cleavage fracture plane. At these initiation sites, the two relatively large inclusions combined with the adjacent grain boundary is a weak location and promotes the brittle fracture initiation.

In almost all CVN specimens (only component welds), an oxide inclusion was identified as the primary initiator. The oxide inclusion is of a larger size than what has been determined as the average size of an inclusion. The oxide inclusion size distribution has been studied for the RPVHW in [20] and the ABLW, giving approximately 0.2 µm as the most probable inclusion size, while most of the oxide initiators are approximately ~1–2 µm in diameter. A mild difference in the initiator size is observed when the CVN specimens are compared to the mini-C(T) specimens, as the initiating particles in the mini-C(T)s are typically smaller. Comparing the ABLW and CBLW, which have a similar ageing history, the same test methods, and the same number of tested specimens, for the CVN specimens, all primary initiators are oxides except two in the ABLW, which are of Mn-rich type. However, for the mini-C(T) specimens in the CBLW all initiators are oxides but in the ABLW majority (11/15) are Mn-rich type of initiators and only three are oxides. In the ABLW mini-C(T) specimens, one primary initiator could not be identified due to very brittle fracture surface and a complex primary initiation area. Nevertheless, the common mechanism found in all specimens is that the brittle fracture initiation occurs at a location of a relatively large inclusion.

The variations between the specimen types could originate from the different stress states ahead of the crack and resulting differences in the

fracture mechanisms. A fracture toughness specimen has a sharp crack, and the loading is quasi-static whereas an impact toughness specimen has a blunt notch, and the loading is dynamic. Consequently, for fracture toughness specimens, the resulting stress profile ahead of the crack is steep with a high peak value [37]. At relatively low loads the peak stress exceeds the critical stress for brittle fracture nucleation enabled through decohesion and cracking of particles, but since the peak value is local, there is not enough energy to grow the microcrack and cause final initiation of brittle fracture. The load needs to be increased to exceed the critical stress over a large enough distance so that the microcrack has enough with energy to cross several grain boundaries and other discontinuities.

In contrary to fracture toughness specimens, the peak stress in impact toughness specimens is flatter and encompasses a larger distance but at low loads the stress does not exceed the critical stress for microcrack nucleation. Once the critical stress is reached, final failure occurs. The larger particles (for example particles of >1.5 μm) appear to be energetically more favourable for microcrack nucleation and for causing final initiation of brittle fracture in impact toughness specimens, but in fracture toughness specimens the larger particles could be deactivated due to high stresses at low loads. Future work using numerical modelling could be applied to quantify the effect of particle size on brittle fracture initiation for blunt notches and sharp cracks.

In Fig. 9, the fracture initiation is compared in terms of the two testing methods. Correlation between the impact toughness energy and the distance of the initiation site from the V-notch and the oxide inclusion size was evident in CVN specimens and, according to the expectation, larger inclusions required less impact energy and were closer to the V-notch per testing temperature [20]. Similarly, the distance of the cleavage crack initiation from the pre-fatigue crack increases with fracture toughness. The oxide inclusion size was plotted with the fracture toughness and there appears a limit at oxide inclusions >1 μm. For the fracture toughness plots the curves are incomplete and do not consider the large amount of the specimens which have a Mn-rich particle as a primary initiator as their size could not be objectively measured. This may explain the L-shaped distribution of the data and that the data population of higher fracture toughness with >1 μm inclusion are those with a Mn-rich primary initiator, meaning at that size the Mn-rich inclusions become critical.

Another note made of the initiation site integrity is whether the inclusion is debonded or broken. In Table 4, the occurrence of the inclusions' integrity is listed. As described in the Chapter 3.2, a debonded

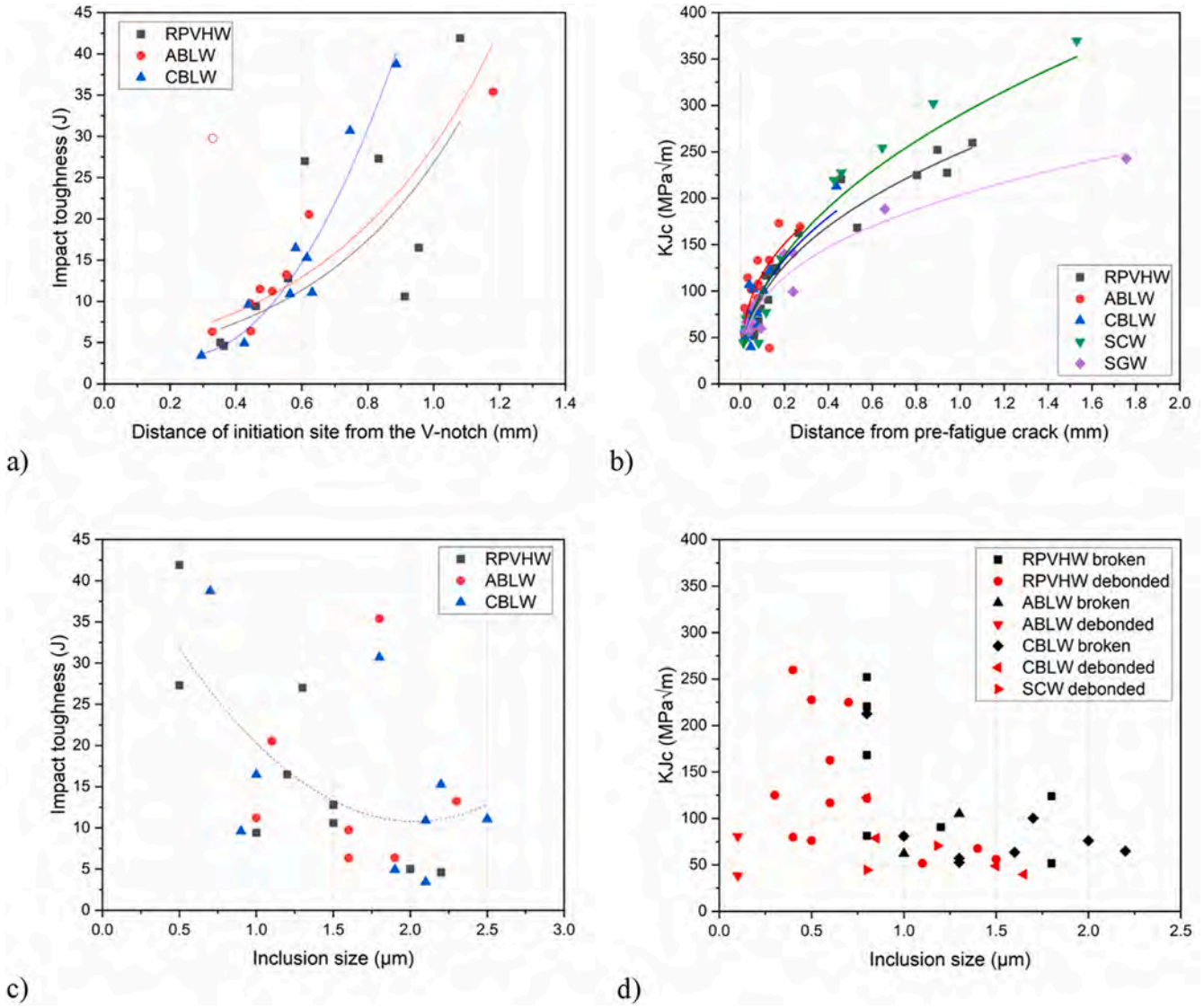

Fig. 9. Correlations of brittle fracture initiation and toughness properties for the impact and fracture toughness. The distance of fracture initiation increases with (a) impact toughness and (b) fracture toughness. (c) Small oxide inclusions require more impact energy to initiate a fracture. (d) Large oxide inclusions are more probably broken inclusions.

inclusion is intact and leaves a dent on the mating fracture surface, therefore the primary crack is assumed to initiate from the breakage of the inclusion-matrix interface. This sets a requirement that the inclusion would be relatively ductile compared to the interface. In some of the broken oxide inclusions, the crack plane could be imaged, and some internal structure was observed. Although in the SEM-EDS analysis the main elemental composition is similar for all oxide inclusions with at least Al, Si, Mn, and O, there might be some differences in the internal structure between the debonded and broken oxide inclusions. The typical layered inclusion in Fig. 8 shows a MnS core, which should be relatively ductile, however, in case the core consists of Al_2O_3 [31], this would make the oxide inclusion brittle and therefore cracking before the interface. The division in Fig. 9 shows that the broken inclusions are larger than the debonded inclusions, supporting the assumption that the debonded and broken inclusions may have different internal structures. However, further analysis of the structure of the inclusions would require high-resolution TEM analysis and is outside the scope of this paper.

In terms of the weld bead microstructure, the primary initiation site was correlated with as-welded and reheated regions for the component weld specimens. Que et al. concluded for the RPVHW that the crack initiation in the as-welded columnar-grained region often showed higher fracture toughness than in the reheated region [21]. For the RPVHW and some of the CBLW specimens, cross-sections of tested and analysed specimens were machined, mounted, and polished for microstructural analysis. The investigated brittle fracture specimens were cut as close to the initiation site as possible to determine the weld microstructure and see whether the fracture initiated in the as-welded or the reheated region. Fig. 10 shows a cross-section of the mating surface of the specimen as shown in Fig. 5, and the as-welded and the reheated regions are outlined and indicated. As pointed in Fig. 10, the primary initiation site is in the as-welded microstructure, however, most of the brittle fracture surface is in the reheated region. It is assumed that the orientation of the weld bead and the growth direction of the grains may affect the crack propagation, especially when the columnar grains are aligned with the crack propagation plane [25]. In the Fig. 10, the crack appears to propagate in the direction aligning the columnar grain until reaching a reheated region.

In some specimens, on the overall fracture appearance, larger regions of ID and IG could be observed, as mentioned in Chapter 3.2, which can be linked to the as-welded and reheated regions of the weld, respectively. The appearance can be relatively evident, especially in the CVN specimen below 41 J, and indicated in the mini-C(T) fracture surfaces in Figs. 4 and 7. When studying the fracture initiation within the weld metal, the crack location in terms of the microstructure is important to consider [25]. One weld bead size is similar to the size of the fracture surface, and most of the specimens, especially mini-C(T), were measuring fracture initiation in the as-welded microstructure, mainly due to the specimen preparation and the probability as there is more as-welded regions than reheated regions. However, since the grain size and phase morphology are different between as-welded and reheated regions, it can be assumed that there are differences in the integrity and the susceptibility for the fracture to propagate. For example, in the as-welded microstructure, the long dendritic grains and the grain boundary ferrite provide a relatively easy passage for a crack to propagate, while the acicular ferrite is considered the toughest microstructure of the present phases. On the other hand, the ratio of polygonal ferrite and acicular ferrite in the reheated region determines the toughness properties of that region. Additionally, the inclusion density may differ between the as-welded and the reheated microstructures.

4.2. Thermal ageing and neutron irradiation effect

The brittle fracture initiation in a multi-pass weld is a complex function of chemical composition, thermal history, and microstructural properties, and is significantly affected by thermal cycles and irradiation [35]. The ageing effect and embrittlement are typically realized as an increase in the hardness. The hardness profiles seen in Fig. 3 for the three component welds do not correlate with the subjected level of neutron fluence. The ABLW has been subjected to the highest dose but shows the lowest hardness, whereas the RPVHW is not considered irradiated, but the hardness is higher than that of the ABLW. The CBLW is also considered both irradiated and thermally aged and has higher hardness than the RPVHW, as expected. A similar trend has been seen in the mechanical test results [19]. The level of dose through the lifetime has been at such low doses (<0.01 dpa), the neutron irradiation effect on hardness is negligible. However, the trend between the component welds emphasises differences in the intrinsic properties of the welds. The increase in hardness appears in the surveillance welds and the comparison to the component welds can be made. As indicated in the Table 3, the ABLW shows the lowest HV1 microhardness, the SCW, RPVHW and CBLW show slightly higher microhardness in increasing order, respectively. A significantly higher microhardness is seen for the accelerated irradiated SGW, which proves the hardness increase due to the neutron irradiation.

This difference was further investigated, and there is a possibility that the PWHT and thermal history were different to ABLW compared to RPVHW and CBLW, as reported by Lindqvist et al. [19] where the

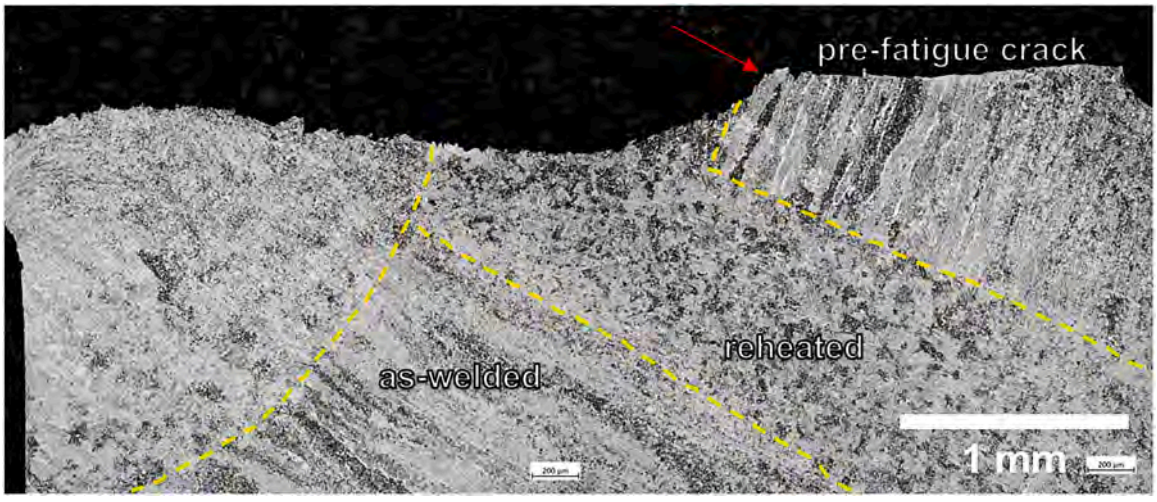

Fig. 10. Cross-section of a mini-C(T) specimen, which mating fracture surface shown in Fig. 5. The cross-section is cut as close to the initiation site which is indicated by the red arrow. The crack propagation direction is from right to left in the figure. The fracture initiated in the as-welded microstructure.

irradiation and ageing effect in mechanical behaviour were studied. A 30 °C difference in PWHT temperature can cause a change in hardness equal to the difference observed between the ABLW and the CBLW. Since the axial weld is welded before the circumferential weld, a possible local double heat treatment may be a reason for lower hardness, as the axial weld could have been subjected to a second PWHT while the adjacent circumferential weld was heat treated. The longer PWHT could cause certain post-weld reactions such as formation of precipitates and carbides as well as coarsening. A small extension in heat treatment and thermal loading compared to the hardness and embrittlement was also observed by Joly et al. [17]. The PWHT would explain the difference in hardness between ABLW to the RPVHW and CBLW, however, the fracture toughness and fracture initiation behaviour of the ABLW correlates with the SCW and, to some extent, with the SGW, which have reportedly longer PWHT.

Embrittlement is typically monitored and observed with a DBTT curve produced by impact toughness testing. According to the reported mechanical properties, the impact toughness between the component welds and non-irradiated baseline showed comparable results [22,19], indicating negligible thermal ageing or irradiation effect during the 23 years of operation, as the reference T_{41J} temperature for the baseline was similar to the RPVHW and CBLW at –75 °C. Therefore, the availability of the surveillance material and their higher state of irradiation are significantly important information to observe more of the long-term operation effect. The welding procedure of all compared welds is the same, however, the PWHT holding time of the surveillance material is almost two times longer than that of the component welds. In terms of brittle fracture initiation, comparing the RPV component welds to the surveillance material, the SCW is comparable to the ABLW as well as the SGW, although it also shows the high fluence irradiation and ageing effect in the vast amount of IG fracture. The SCW provides information on the comparability between the surveillance material and the component weld, and the SGW represents an extended life-time irradiation effect.

One of the main objectives of the study was to compare the behaviour of the welds after subjection to different conditions. The harvested component welds at thermally aged state and at irradiated state, and two irradiated surveillance welds, were to be compared by the operation effect on the weld microstructure, and its effect on the brittle fracture initiation. Overall, there are systematic heterogeneities between the brittle fracture initiation in the different weld metals. In all specimens with cleavage fracture initiation, a particle is observed at the primary initiation site, however, the type of the particle can be linked to certain investigated welds, but the evidence of the thermal and irradiation history is debatable, and the initiation type appears to be unaffected by the aged condition. The indications of thermal ageing and irradiation in the fractography are mainly observed in the amount of IG and ID cracking. However, the other differences seen between the welds, such as the different inclusions, might be more related to welding metallurgy and processing parameters and not related to the operation conditions. This could be for example process purity, PWHT, and overall homogeneity of the welds. The independency of the inclusion type from the irradiation state correlates with a study by Chekhonin et al. [38] where a systematic investigation of microstructure effect on brittle fracture initiation was done on SA508 base material, where carbides and grain boundaries are the main initiators of a brittle fracture, however, no correlation between the cleavage fracture initiation type and neutron irradiation exposure was made.

The ageing effects in an RPV can be divided into hardening effects, i.e., precipitation and cluster formation, and non-hardening effects, i.e., P segregation, which might result in different fracture mechanical behaviour and therefore in different fracture surface appearance [4,9,39]. The elemental segregation decreases resistivity to brittle fracture initiation and induces IG cracking. In the study of similar thermally aged pressurizer LAS components, IG cracking was observed as one main fracture mechanism after thermal ageing [40]. The IG cracking has been observed to occur typically at the PAGBs. In literature this is discussed typically as reversible temper embrittlement. In the study by Hsu et al., not only P segregated into PAGBs but also Mo, Mn, and Ni [41]. Comparing the different grain boundaries in a bainitic base material, most elemental segregation was observed to occur in the PAGBs. In the current study, the investigated weld metal has high contents of Mn and Ni, easing the brittle fracture propagation in the PAGBs after ageing. However, in the component welds, due to the relatively low fluence, negligible operation-induced embrittlement is seen, but the large Mn-rich particles located at or adjacent to the grain boundaries appeared to induce a minor amount of IG. The main microstructure of acicular ferrite nucleates from non-metallic inclusions inside the PAGBs, and although acicular ferrite itself has high toughness properties, the brittle oxide inclusions are weak links. Comparing the ageing conditions and the brittle fracture initiation investigated in this study, there is no evidence that the operational thermal ageing or irradiation would have affected the mechanism to initiate a cleavage fracture, except in the SGW where the higher fluence had sensitised the PAGBs inducing IG cracking.

5. Conclusions

The microstructure and fracture surfaces of the decommissioned Barsebäck Unit 2 RPV weld metal were studied extensively for thermally aged and irradiated weld metals and compared to the surveillance material. The investigation concluded a systematic brittle fracture analysis of total of 101 brittle CVN and mini-C(T) specimens. The study focuses on three RPV component welds, one from the RPV head and two from the beltline region, and two surveillance welds. All welds are manufactured using the same wire material, using submerged arc welding with high Mn and Ni and low Cu alloying contents. The RPV welds are double-U groove welds, and the surveillance welds are fully representative of the component welds. The main conclusions are drawn from the investigation.

- The multi-pass welds have a complex microstructure consisting of as-welded and reheated regions, with local differences in chemical composition, phase structure, and grain sizes, and thermal history, which affect the mechanical properties. The as-welded regions have high toughness with acicular ferrite, however, if the columnar weld bead is aligned with the crack propagation plane, it can provide easier fracture propagation.
- The weld includes a large number of non-metallic inclusions and second-phase particles. The inclusions are required in the weld solidification process to nucleate acicular ferrite microstructure. The average size of an oxide inclusion is ~0.2 μm in diameter.
- The brittle cleavage fracture initiates in all investigated specimens from a relatively large particle, which is defined as the weakest link. Two main types of inclusions at primary cleavage fracture initiation sites have been identified:
  i) Roundish non-metallic oxide inclusions, which are layered multi-phase particles consisting of Mn, Al, Si, Ti, O, and S. The size of such inclusion at a primary initiation site is ~0.5–2.5 μm. This type of inclusion is found as a primary initiator in all RPVHW and CBLW CVN and mini-C(T) specimens and in most of the ABLW CVN specimens and only few mini-C(T) specimens. The inclusion is either debonded from the matrix or broken in half, i.e., either the crack initiates from the inclusion-matrix interface or within the inclusion, respectively.
  ii) Irregular-shaped Mn-rich particles, which are likely carbides and of size approximately ~0.5–2 μm. The Mn-rich particles are assumed to locate closer to grain boundaries and the initiation site has a minor area of IG cracking adjacent to the cleavage fracture plane. This type of particle is found as a primary initiator in almost all ABLW, SCW, and SGW mini-C(T) specimens. All Mn-

rich inclusions are broken and can be found on both mating surfaces.

- The larger the oxide inclusion, the lower the impact energy is required to initiate a brittle fracture. The distance of the primary initiation site from the V-notch or from the pre-fatigue crack increases with impact and fracture toughness. Of all brittle initiation sites, the smaller range of the oxide inclusions are typically debonded and the larger range are typically broken.
- The cleavage fracture initiation appears to be unaffected by the operation induced aging condition. The main deviations in the cleavage fracture initiation derive from the complex weld microstructure and processing parameters instead of strong effect from thermal ageing or neutron irradiation damage. The two different initiator types are more dependent on the specimen type, i.e., testing method, PWHT, and the location of the pre-crack in the weld bead. However, the higher fluence causes larger IG fraction on the fracture surface.

CRediT authorship contribution statement

N. Hytönen: Conceptualization, Data curation, Formal analysis, Funding acquisition, Investigation, Methodology, Project administration, Writing – original draft, Writing – review & editing. **S. Lindqvist:** Writing – review & editing, Investigation, Conceptualization, Formal analysis. **J. Lydman:** Writing – review & editing, Methodology, Investigation, Formal analysis, Data curation. **Y. Ge:** Methodology, Investigation, Formal analysis, Data curation. **Z. Que:** Writing – review & editing, Supervision. **P. Efsing:** Writing – review & editing, Supervision, Resources, Funding acquisition, Conceptualization.

Declaration of competing interest

The authors declare that they have no known competing financial interests or personal relationships that could have appeared to influence the work reported in this paper.

Data availability

Data will be made available on request.

Acknowledgements

The funding for the research work is by the National Nuclear Waste Management (VYR) and VTT Technical Research Centre of Finalnd within the research programmes SAFIR2022 and SAFER2028 projects BRUTE (2022) and BRIGHT (2025). The authors want to thank and acknowledge BREDA (Barsebäck RPV Research&Development Arena) of the substantial in-kind contribution for providing the research material. The authors want to thank Ringhals for providing the field service of extracting the material and Jenny Roudén for the support. The Nordic nuclear safety research forum NKS is acknowledged for additional funding to support the Nordic collaboration in nuclear safety research. The EU NOMATEN project is acknowledged for the support with the publication work. The authors want to thank Ulla Ehrnstén for guidance and technical discussions.

References

[1] IAEA, Integrity of reactor pressure vessels in nuclear power plants: assessment of irradiation embrittlement effects in reactor pressure vessel steels, in: International Atomic Energy Agency Nuclear Energy Series, 11, IAEA, 2009. NP-T-3.
[2] Y. Shtrombakh, B. Gurovich, E. Kuleshova, D. Maltsev, S. Fedotova, A. Chernobaeva, Thermal ageing mechanisms of VVER-1000 reactor pressure vessel steels, J. Nucl. Mater. 452 (2014) 348–358.
[3] P. Haušild, C. Berdin, P. Bompard, Prediction of cleavage fracture for a low-alloy steel in the ductile-to-brittle transition temperature range, Mater. Sci. Eng. A 391 (1–2) (2005).
[4] S.G. Druce, G. Gage, G. Jordan, Effect of ageing on properties of pressure vessel steels, Acta Metall. 34 (4) (1986) 641–652.
[5] K. Lindgren, M. Boåsen, Z. Que, K. Stiller, P. Efsing, M. Thuvander, Post-irradiation annealing of high flux irradiated and surveillance material reactor pressure vessel weld metal, J. Nucl. Mater. 562 (2022).
[6] L. Liu, K. Nishida, K. Dohi, A. Nomoto, N. Soneda, K. Murakami, Z. Li, D. Chen, N. Sekimura, Effects of solute elements on hardening and microstructural evolution in neutron-irradiated and thermally-aged reactor pressure vessel model alloys, J. Nucl. Sci. Technol. 53 (10) (2016) 1546–1553.
[7] J. Hyde, G. Sha, E. Marquis, A. Morley, K. Wilford, T. Williams, A comparison of the structure of solute clusters formed during thermal ageing and irradiation, Ultramicroscopy 111 (2011) 664–671.
[8] R.M. Horn, R.O. Ritchie, Mechanisms of tempered martensite embrittlement in low alloy steels, Metall. Trans. A 9A (1978) 1039–1053.
[9] P. Bischler, R. Wild, A microstructural study of phosphorus segregation and intergranular fracture in neutron irradiated submerged-Arc welds, in: Proceedings of the Effects of Radiation on Materials: 17th International Symposium, ASTM STP 1270, 1996.
[10] Y.R. Im, Y.J. Oh, B.J. Lee, J.H. Hong, H.C. Lee, Effects of carbide precipitation on the strength and Charpy impact properties of low carbon Mn-Ni-Mo bainitic steels, J. Nucl. Mater. 297 (2001) 138–148.
[11] A. Griffith, The phenomena of rupture and flow in solids, Philos. Trans. R. Soc. Lond. 221 (1921) 163.
[12] W.J. Yang, B.S. Lee, Y.J. Oh, M.Y. Huh, J.H. Hong, Microstructural parameters governing cleavage fracture behaviors in the ductile-brittle transition region in reactor pressure vessel steels, Mater. Sci. Eng. A 379 (2004) 17–26.
[13] A. Pineau, A. Benzerga, T. Pardoen, Failure of metals I: brittle and ductile fracture, Acta Mater. 107 (2016) 424.
[14] C.J. McMahon, M. Cohen, Initiation of cleavage in polycrystalline iron, Acta Metall. 13 (6) (1965) 591–604.
[15] J. Tweed, J. Knott, Micromechanisms of failure in C Mn weld metals, Acta Metall. 35 (7) (1987) 1401–1414.
[16] U. Zerbst, R. Ainsworth, H.T. Beier, H. Pisarsk, Z. Zhang, K. Nikbin, T. Nitschke-Pagel, S. Münstermann, P. Kucharczyk, D. Klingbeil, Review on fracture and crack propagation in weldments–a fracture mechanics perspective, Eng. Fract. Mech. 132 (2014) 200–276.
[17] P. Joly, L. Sun, P. Efsing, J. Massoud, F. Somville, R. Gerard, Y. An, J. Bailey, Characterization of in-service thermal ageing effects in base materials and welds of the pressure vessel of a decommissioned PWR pressurizer, after 27 years of operation, in: Proceedings of the 19th International Conference on Environmental Degradation of Materials in Nuclear Power Systems-Water Reactors 2019, Boston, 2019.
[18] M. Boåsen, P. Efsing, U. Ehrnstén, On flux effects in a low alloy steel from a Swedish reactor pressure vessel, J. Nucl. Mater. 484 (2017) 110–119.
[19] S. Lindqvist, A. Norrgård, P. Arffman, N. Hytönen, J. Lydman, P. Efsing, S. Suman, P. Nevasmaa, Mechanical behavior of high-Ni/high-Mn Barsebäck 2 reactor pressure vessel welds after 28 years of operation, J. Nucl. Mater. 581 (2023).
[20] N. Hytönen, Z. Que, P. Arffman, J. Lydman, P. Nevasmaa, U. Ehrnstén, P. Efsing, Effect of weld microstructure on brittle fracture initiation in a thermally aged boiling water reactor pressure vessel head weld metal, Int. J. Miner. Metall. Mater. 28 (2021) 867–876.
[21] Z. Que, M. Lindroos, J. Lydman, N. Hytönen, S. Lindqvist, P. Efsing, P. Nevasmaa, P. Arffman, Brittle fracture initiation in decommissioned boiling water reactor pressure vessel head weld, J. Nucl. Mater. 569 (2022).
[22] L. Sirkiä, J. Lydman, U. Ehrnstén, S. Lindqvist, Determination of T0 with miniature C(T) specimens for a high-Ni weld metal used in a boiling water reactor pressure vessel, in: Proceedings of the Baltica XI, Helsinki, 2019.
[23] K. Lindgren, P. Efsing, M. Thuvander, Elemental distribution in a decommissioned high Ni and Mn reactor pressure vessel weld metal from a boiling water reactor, Nucl. Mater. Energy 36 (2023).
[24] M. Boåsen, C. Dahlberg, P. Efsing, J. Faleskog, A weakest link model for multiple mechanism brittle fracture-Model development and application, J. Mech. Phys. Solids 104224 (2021).
[25] D.V. Klein, J. Faleskog, Influence of heterogeneity due to toughness variations on weakest-link modeling for brittle failure, Eng. Fract. Mech. 292 (2023).
[26] J. Risner and A. Alpan, "Reactor Pressure Vessel Fluence, DPA, and Uncertainty Qualification in Extended Beltline Locations," Oak Ridge National Laboratory, 2021.
[27] "ISO 148-1:2016–metallic materials–Charpy pendulum impact test–Part 1: test method," 2024 [Online]. Available: https://www.iso.org/standard/63802.html.
[28] "ISO 14556:2023–metallic materials–Charpy V-notch pendulum impact test–instrumented test method," 2024.[Online]. Available: https://www.iso.org/standard/82164.html.
[29] "ASTM E1921-21, Standard test method for determination of reference temperature, T0, for ferritic steels in the transition range," 2021.
[30] S. Kou, Welding Metallurgy, John Wiley and Sons, New York, 1987.
[31] S.S. Babu, S.A. David, T. Debroy, Develoment od macro and microstructures of carbon-manganese low alloy steel welds: inclusion formation, Mater. Sci. Technol. 11 (1995) 186–199.
[32] S.S. Babu, The mechanism of acicular ferrite in weld deposits, Curr. Opin. Solid State Mater. Sci. 8 (2004) 267–278.
[33] G.M. Evans, N. Bailey, Metallurgy of Basic Weld Metal, Abington Publishing, Cambridge, England, 1997.
[34] D. Sarma, A. Karasev, P. Jönsson, On the role of non-metallic inclusions in the nucleation of acicular ferrite in steels, ISIJ Int. 49 (7) (2009) 1063.

[35] M.F. Mahony, "Investigation into the mechanism of acicular ferrite nucleation in steel weld metal," 1999.
[36] T.K. Lee, H.J. Kim, B.Y. Kang, S.K. Hwang, Effect of inclusion size on the nucleation of acicular ferrite in welds, ISIJ Int. 40 (12) (2000) 1260–1268.
[37] K. Wallin, Fracture Toughness of Engineering Materials: Estimation and Application, EMAS Publishing, 2011.
[38] P. Chekhonin, A. Das, F. Bergner, E. Altstadt, Microstructural characterisation of brittle fracture initiation sites in reactor pressure vessel steels, Nucl. Mater. Energy 37 (101511) (2023).
[39] B. Margolin, E. Yurchenko, A. Morozov, D. Chistyakov, Prediction of the effects of thermal ageing on the embrittlement of reactor pressure vessel steels, J. Nucl. Mater. 44 (2014) 107–114.
[40] M. Boåsen, Modeling of Structural Integrity of Aged Low Alloy Steels Using Non-Local Mechanics, KTH Royal Institute of Technology, Stockholm, Sweden, 2020.
[41] C.Y. Hsu, J. Stodolna, P. Todeschini, F. Delabrouille, F. Christien, Effect of bainitic or martensitic microstructure of a pressure vessel steel on grain boundary segregation induced by step cooling simulating thermal aging, J. Nucl. Mater. 584 (2023).

(1)

NuMat

VATTENFALL

(2)

KTH VETENSKAP OCH KONST

(3)

Advanced characterization of inclusions acting as brittle fracture initiators of miniature compact tension C(T) specimens from RPV welds of a decommissioned boiling water reactor

Pedro A. Ferreirós[1], Noora Hytönen[1], Jari Lydman[1], Yanling Ge[1], Zaiqing Que[1], Pål Efsing[2,3]

[1] *Advanced Materials for Nuclear Energy, VTT Technical Research Centre of Finland Ltd., Finland*

[2] *Ringhals AB, Väröbacka 43585, Sweden*

[3] *Department of Solid Mechanics, Royal Institute of Technology (KTH), Sweden*

15th October 2024

Introduction

Brittle fracture initiators

Material: Welds of RPV & surveillance chains → *Samples from:* Charpy V-notch Mini-C(T) → *Fractography:* SEM / EDS (Initiator site) → *Sectioning of initiator inclusions:* FIB → *Inclusion characterization:* TEM / STEM

- *Correlation between surveillance material and RPV*
- *Fracture through RPV wall thickness*

SEM-EDS fractography
> 100 specimens
(RPVH, Beltline, Surveillance)

Debonded or broken inclusions:
a) AlSiMnO (Roundish)
b) Mn-rich (Irregular-shaped)
c) AlSiMnO + Mn-rich

TEM in some of the inclusion initiator fracture
(RPVH, Beltline, Surveillance)

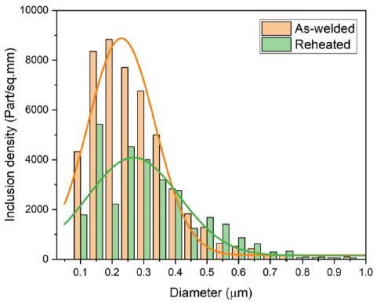

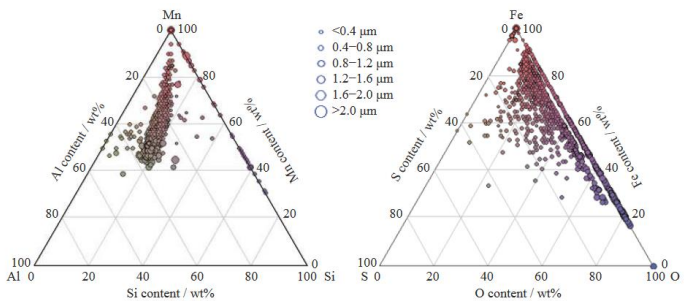

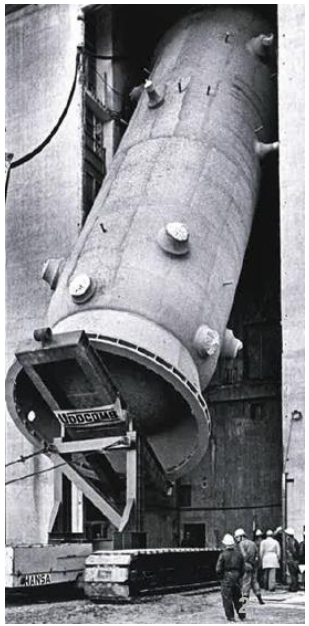

[1] N. Hytönen et al., Int J Miner Metall Mater 28 (2021) 867
[2] N. Hytönen et al., J Nucl Mat 603 (2025) 155423

Materials

- Decommissioned Barsebäck Unit 2, 600-MW boiling water reactor (1977-2005), Sweden
- 23 effective full power years at 288 °C.
- Specimens from RPV welds. Low-alloy steel with high Ni- and Mn-content, low Cu-content

RPV Head → thermal loading, non-irradiated
RPV Beltline → thermal loading & irradiated

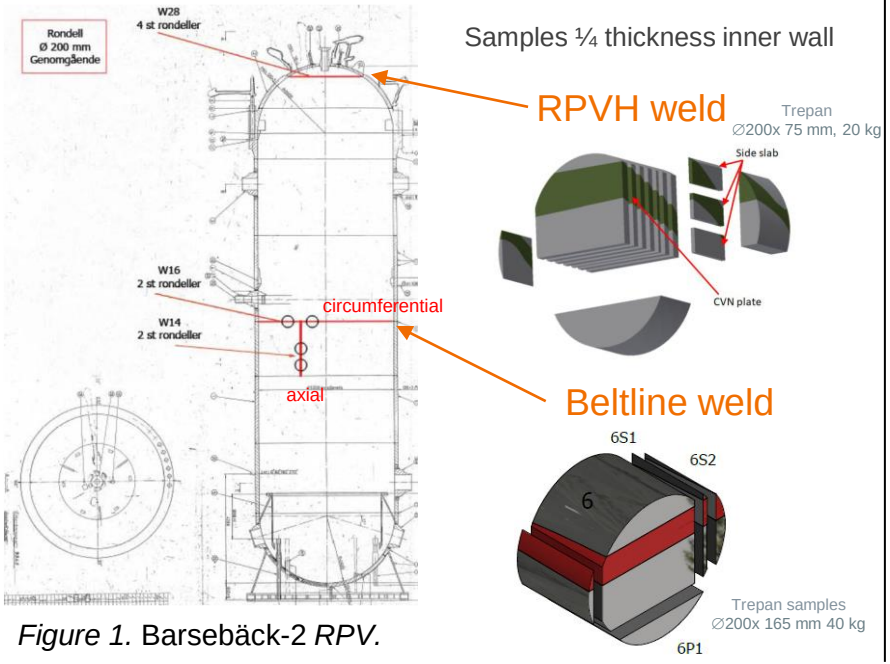

Figure 1. Barsebäck-2 *RPV.*

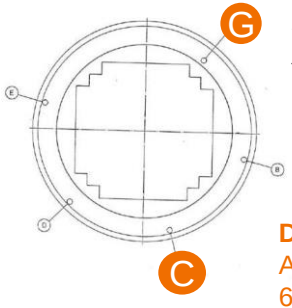

Figure 2. The positions of the surveillance chains in the RPV.

Dose equivalent:
Axial beltline RPV
60 years operation

Material	Fluence (E>1 MeV) n/cm²
Chain C	1.0×10^{18}
Chain G	5.9×10^{19}
ABLW	8.0×10^{17}
CBLW	2.9×10^{16}

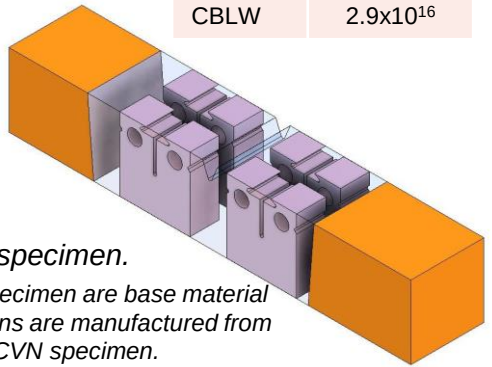

Figure 3. Miniature-C(T) specimens from the CVN specimen.

The orange ends of the CVN specimen are base material and the miniature C(T) specimens are manufactured from weld metal in the middle of the CVN specimen.

Mechanical testing

Tensile test

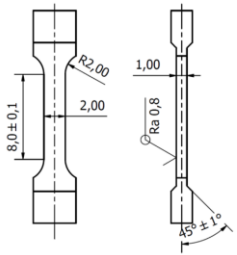

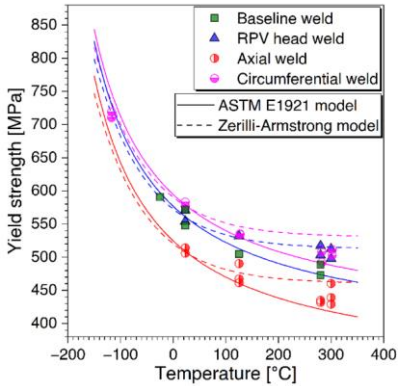

Charpy test

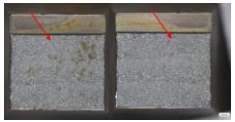

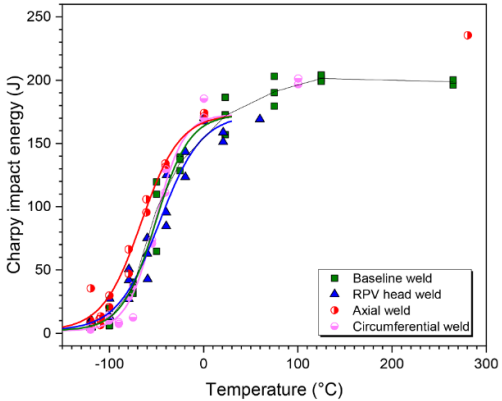

CVN fracture (Debonded oxide)

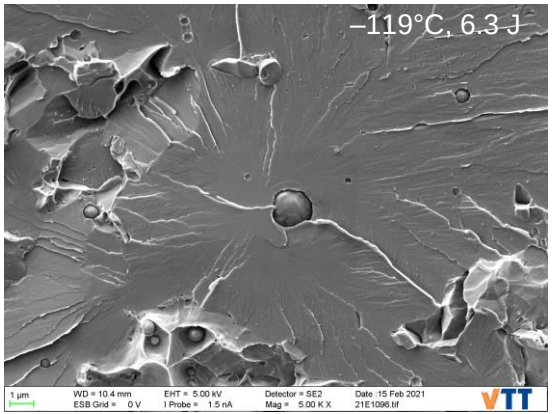

Miniature compact tension (mini-C(T))

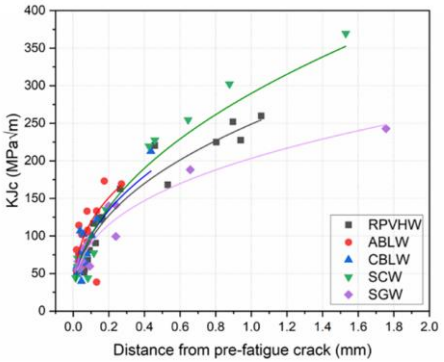

T=50°C, 57.1 MPa√m

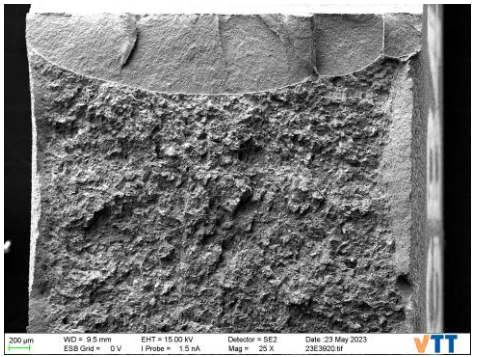

Fracture of mini-C(T)

RPVH specimen: 3B28-3B

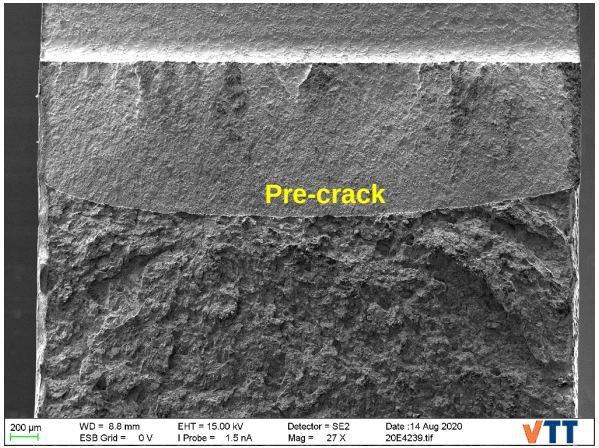

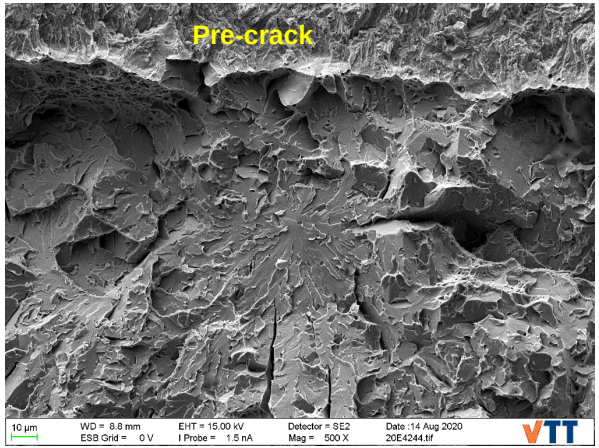

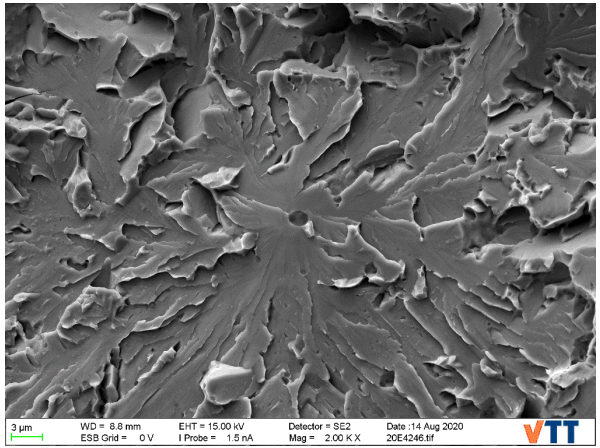

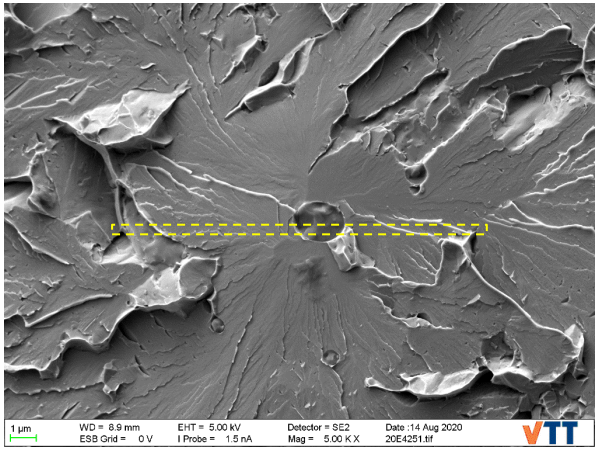

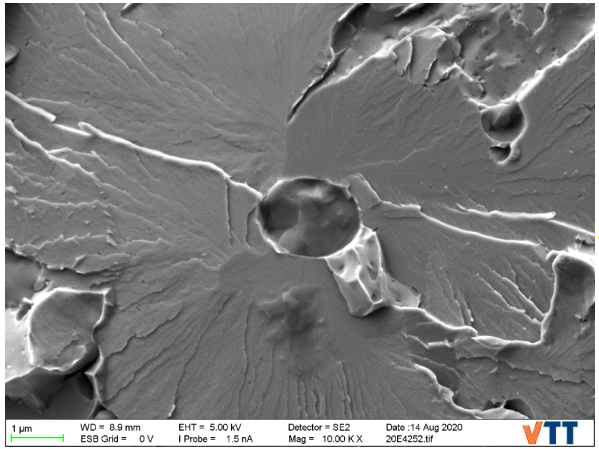

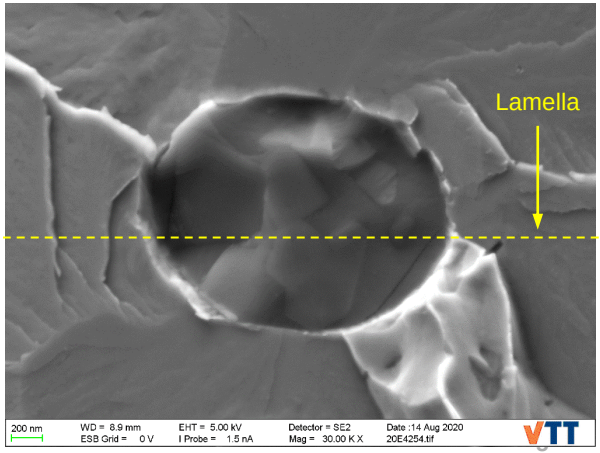

Fracture of mini C(T)

RPVH specimen: 3B28-3B

Side B

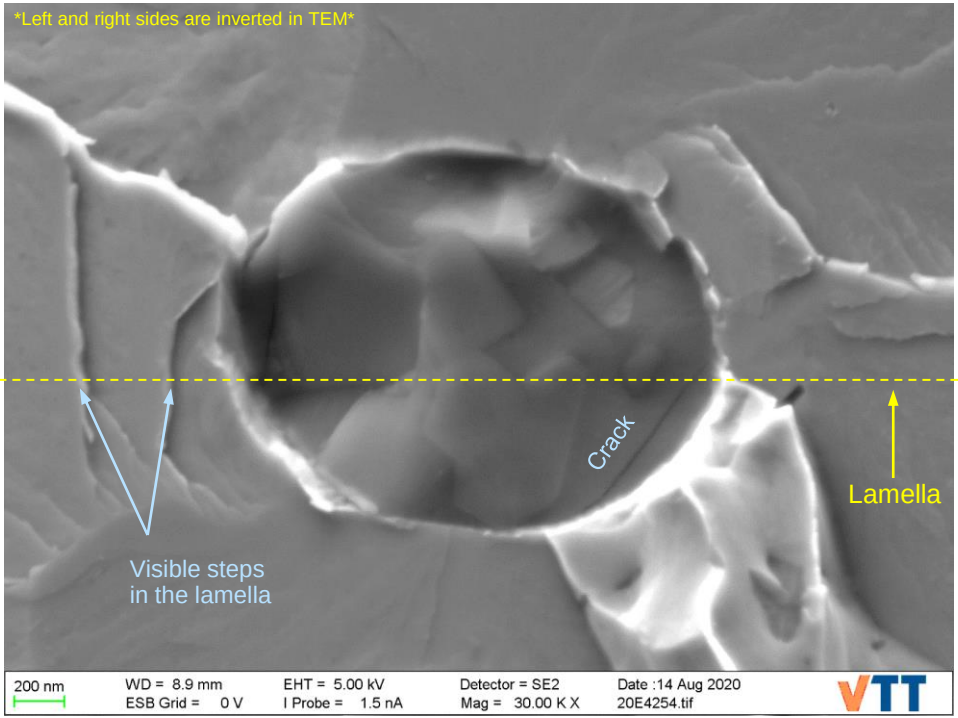

Side A

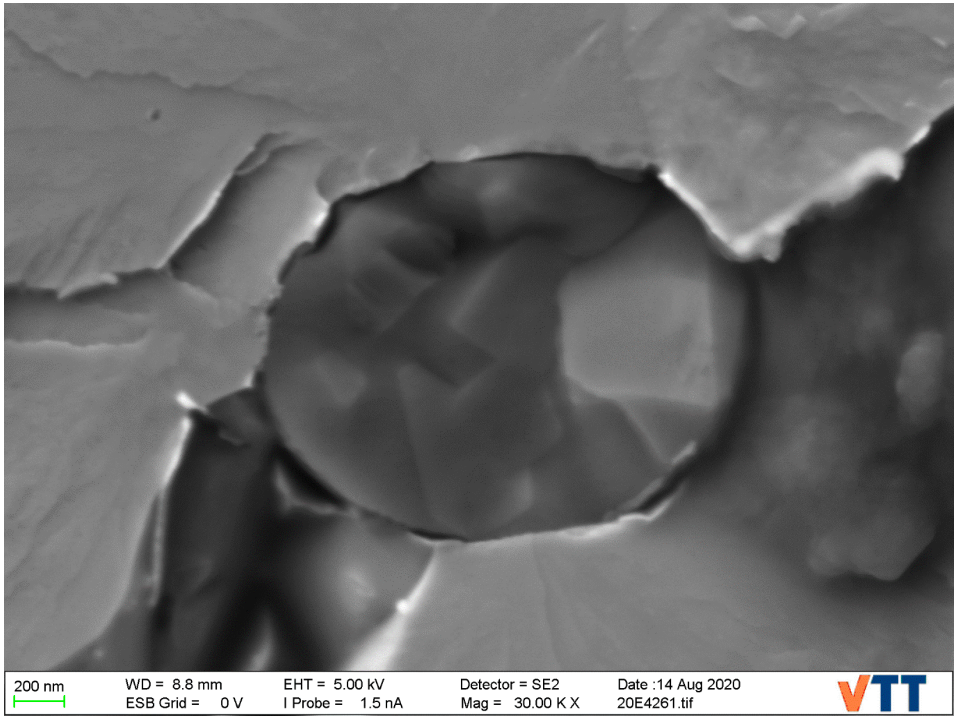

Liftout lamella

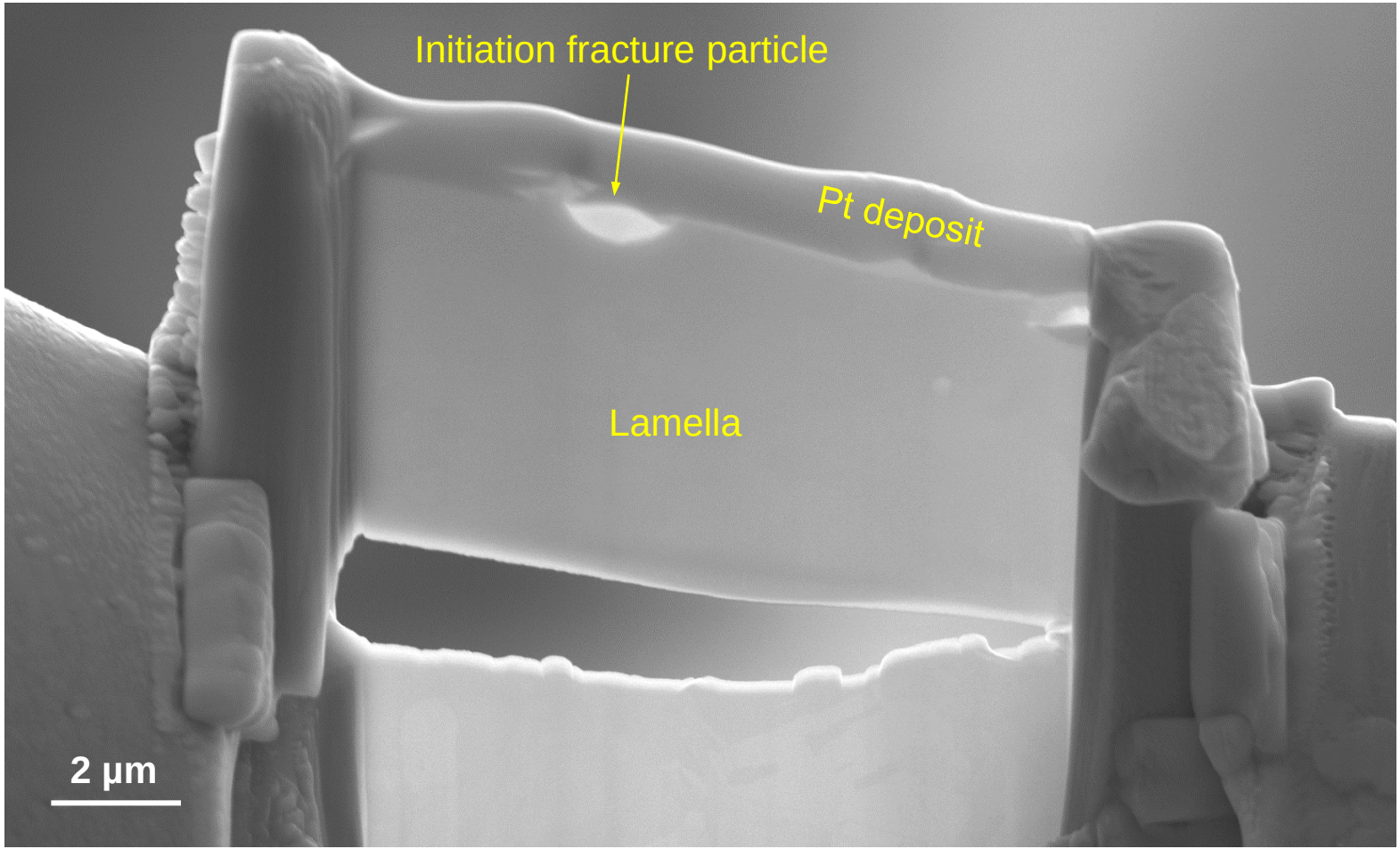

STEM

BF

Pt deposit: e^- beam Ion beam

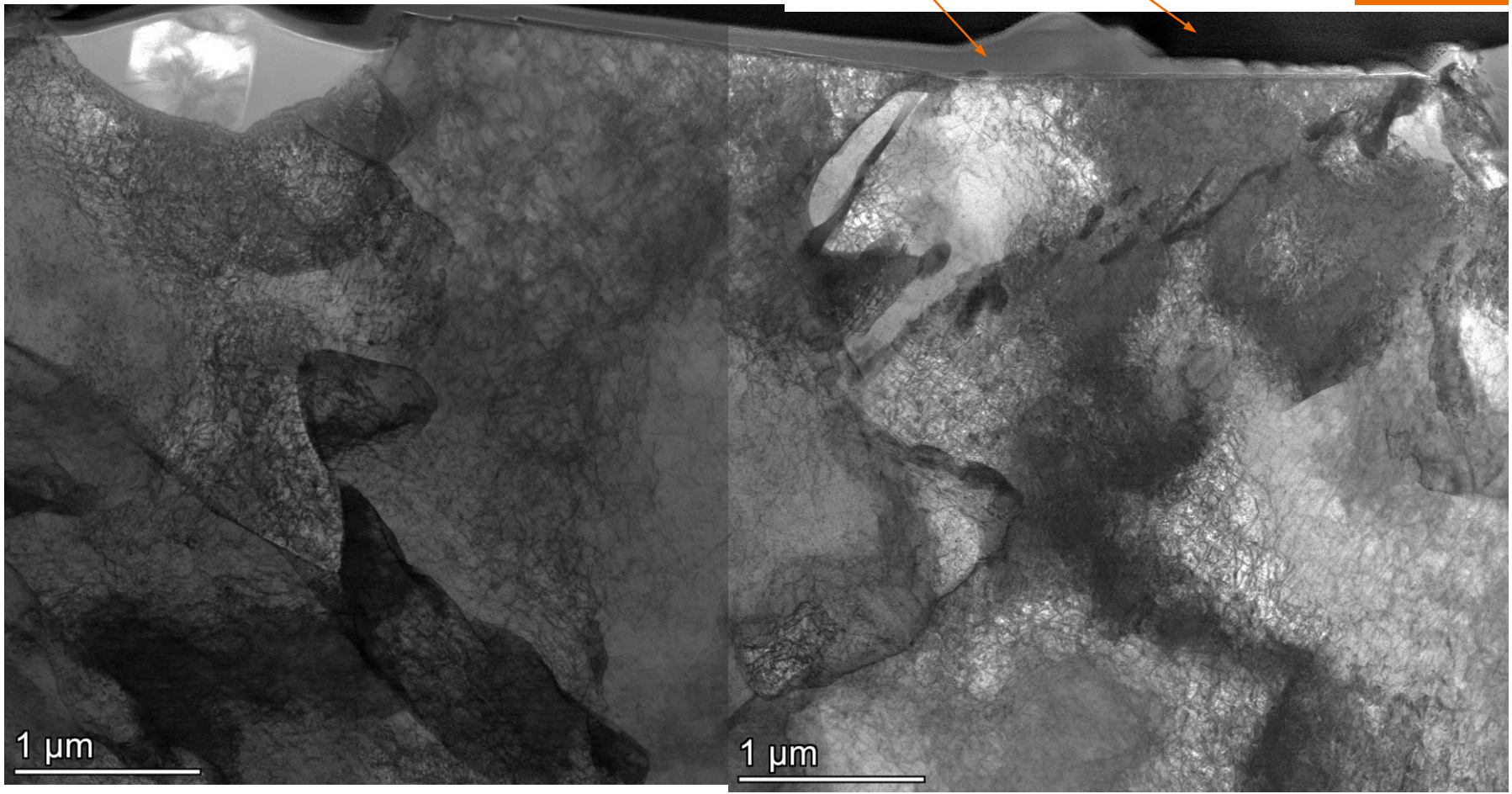

STEM-EDS

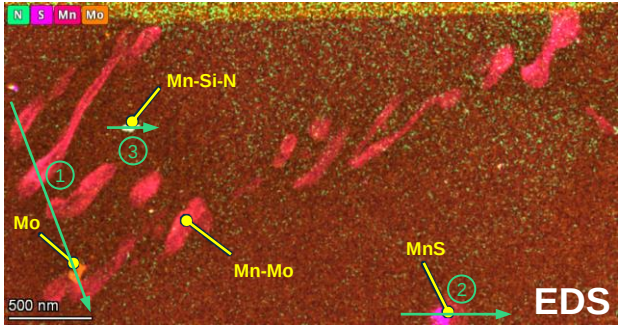

BF

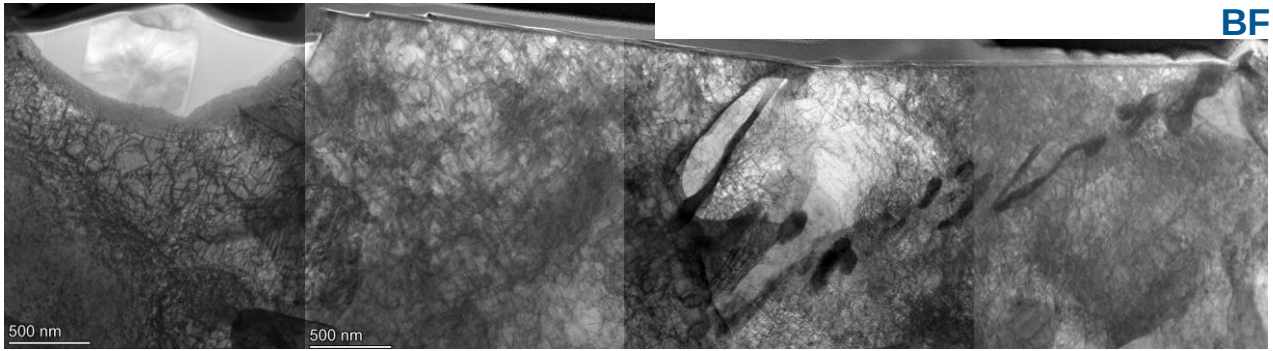

HAADF

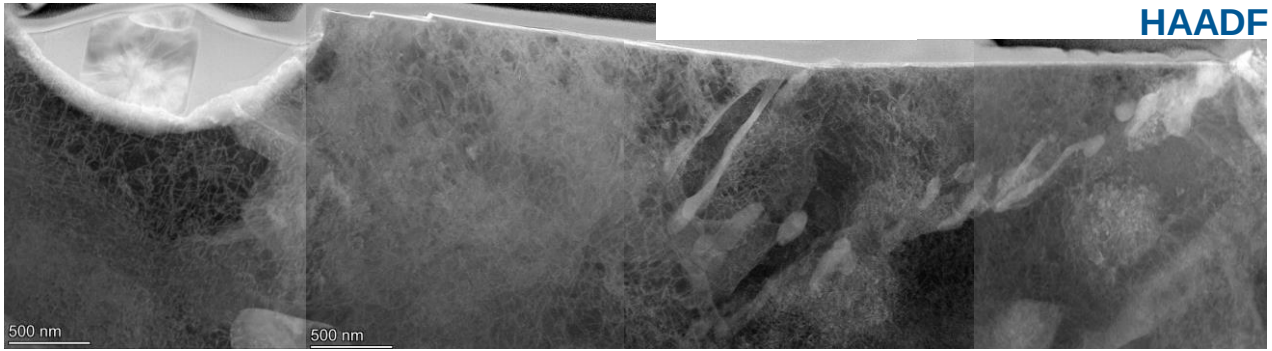

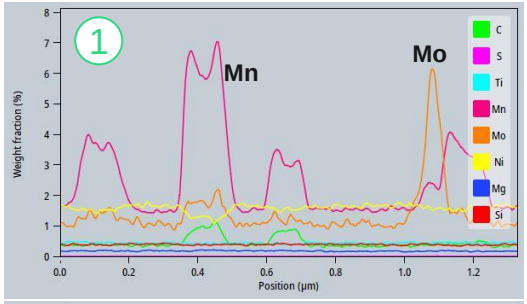

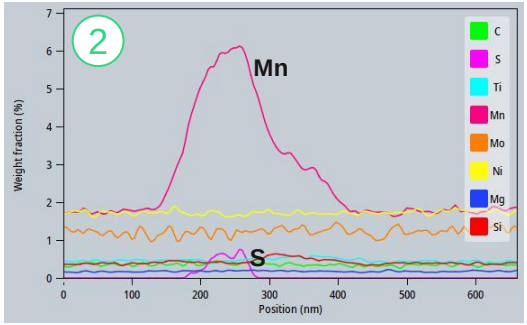

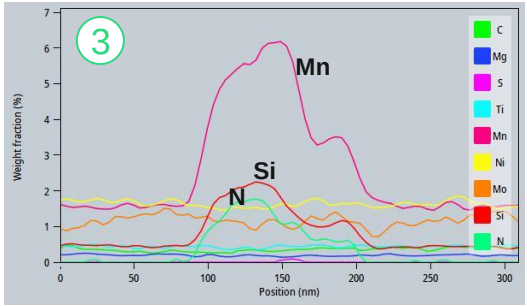

STEM

HAADF

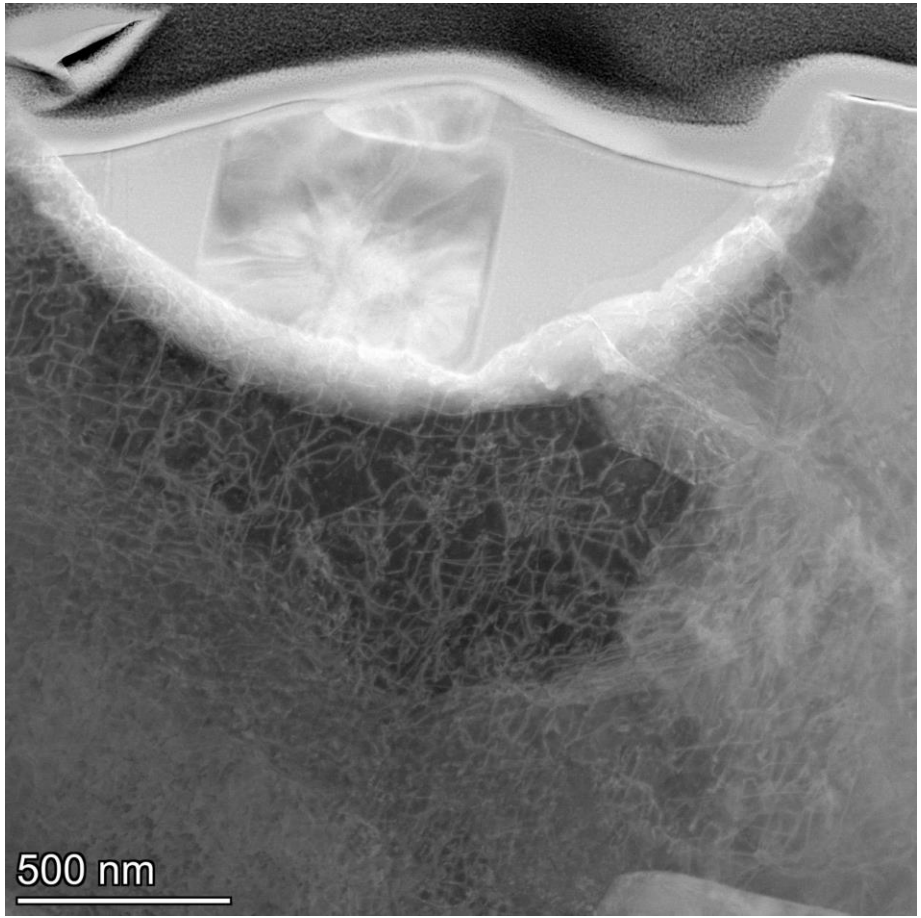

BF

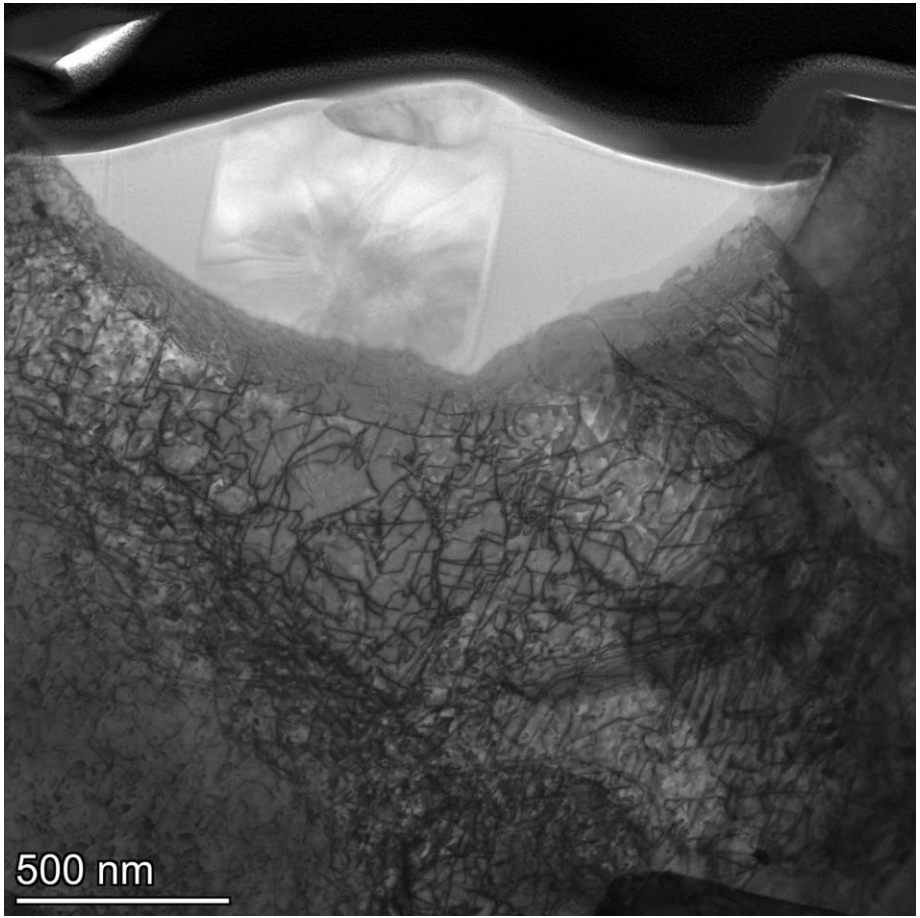

EDS STEM


HAADF
200 nm

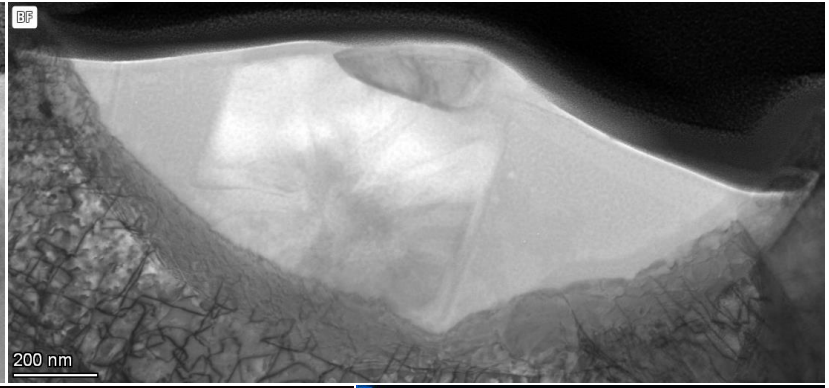
BF
200 nm

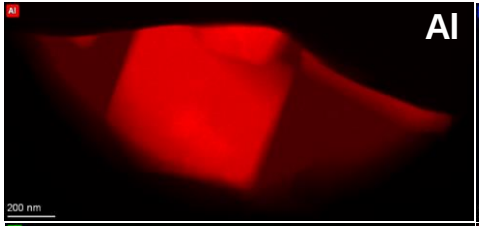
Al
200 nm

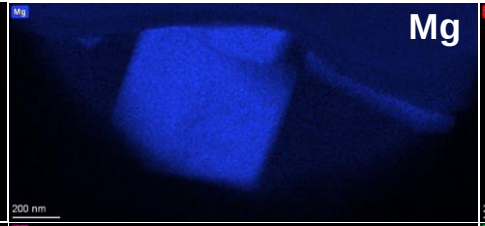
Mg
200 nm

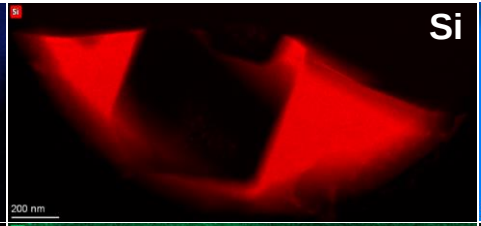
Si
200 nm

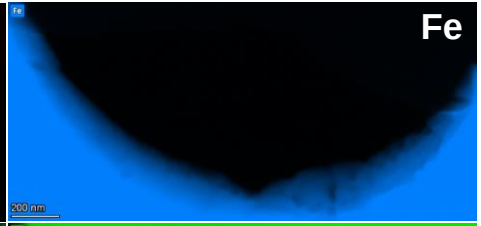
Fe
200 nm

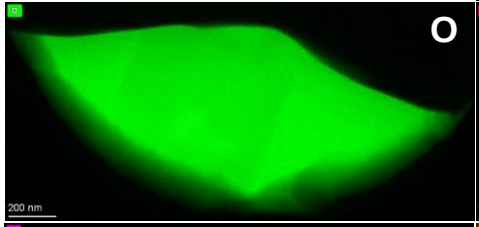
O
200 nm

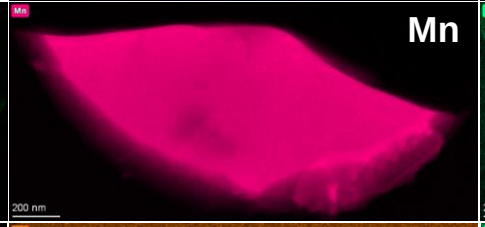
Mn
200 nm

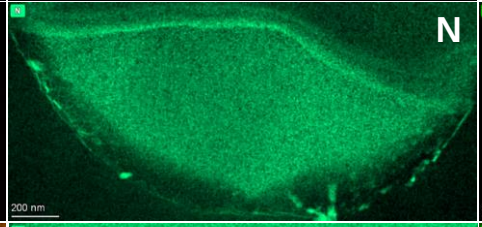
N
200 nm

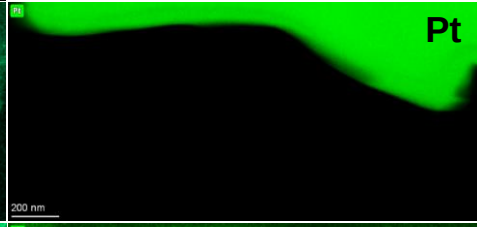
Pt
200 nm

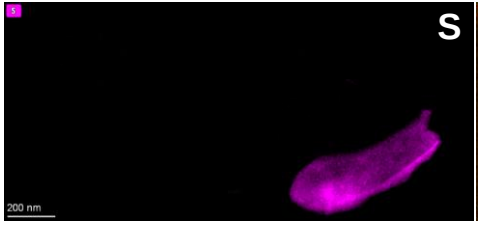
S
200 nm

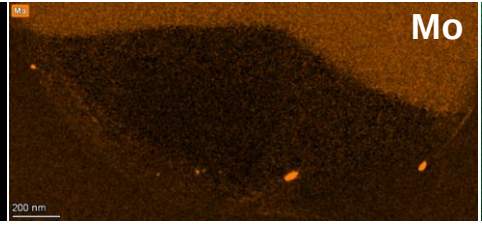
Mo
200 nm

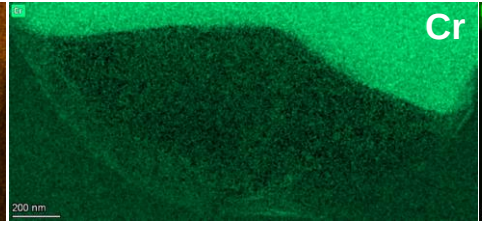
Cr
200 nm

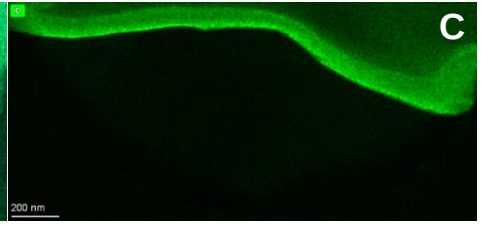
C
200 nm

EDS

(Grouped elements)(The same 12 elements of the previous page)

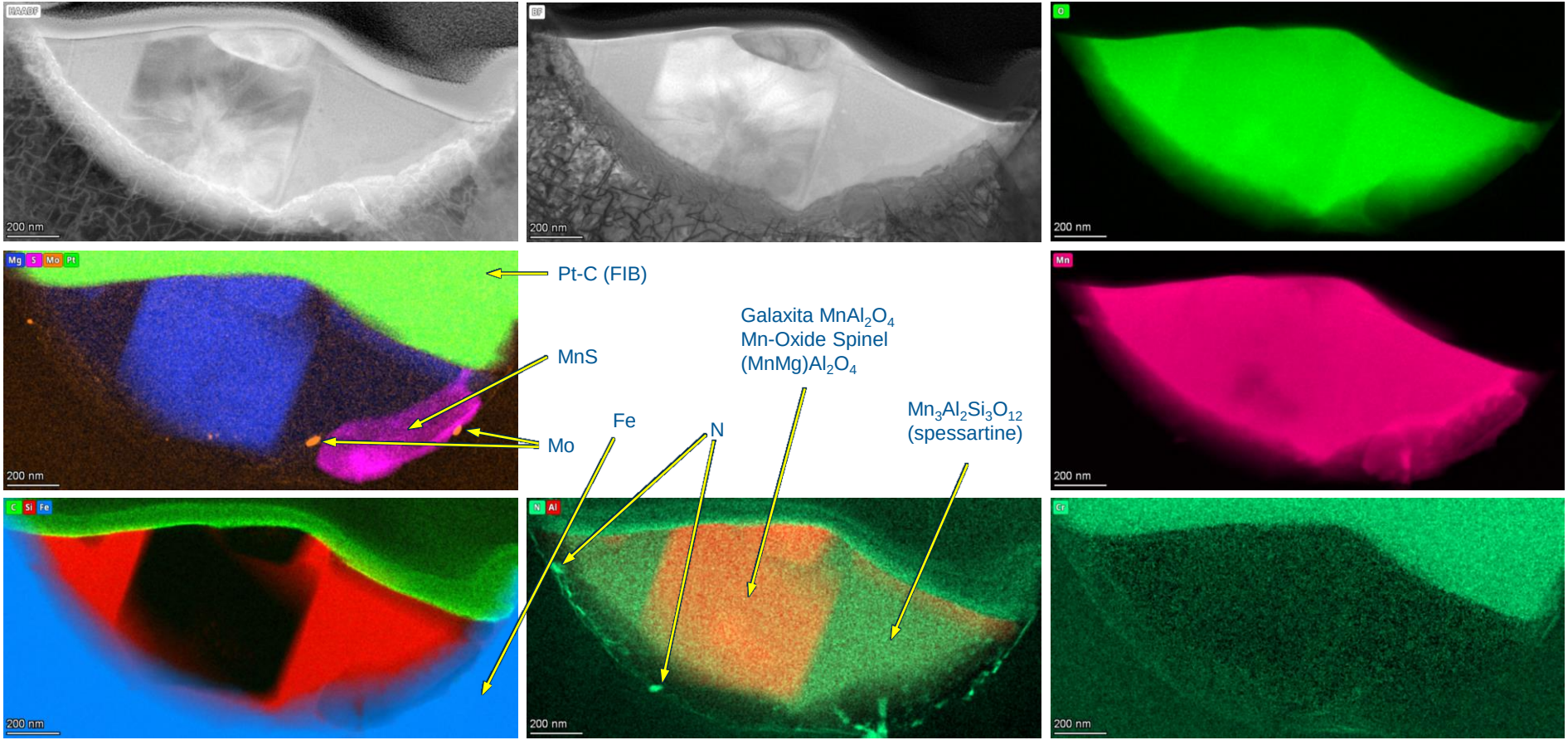

TEM

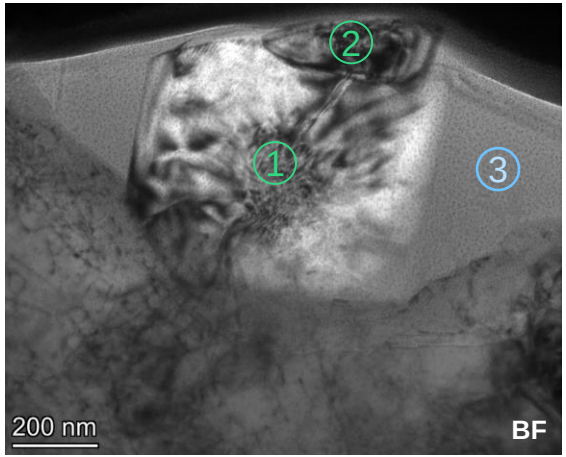

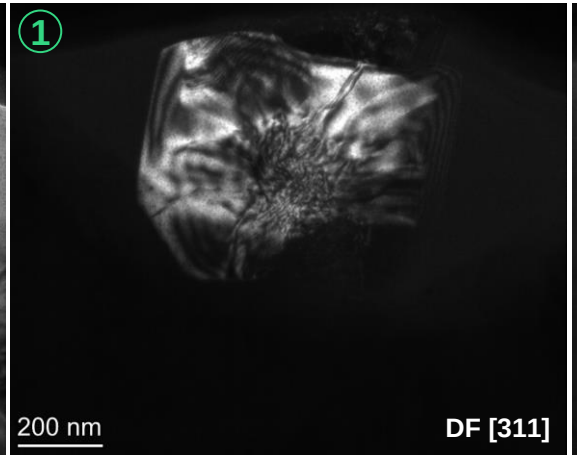

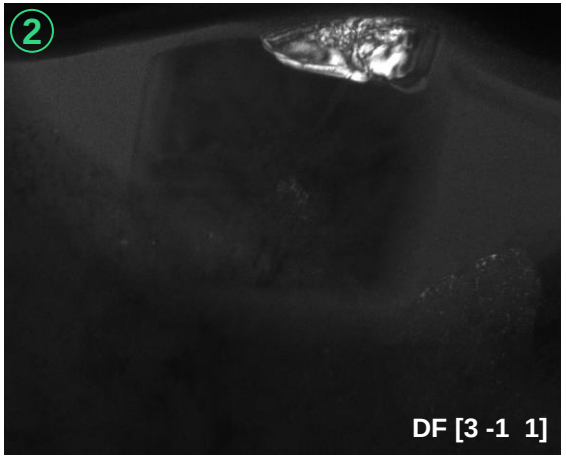

14% 29% 57%

Galaxita $MnAl_2O_4$

Mn-Oxide Spinel $(MnMg)Al_2O_4$

1

Element	Atomic Fraction (%)	Atomic Error (%)
O	53.3	3.3
Mg	1.9	0.4
Al	28.1	4.1
Mn	16.7	2.4

2

Element	Atomic Fraction (%)	Atomic Error (%)
O	49.2	3.3
Mg	2.0	0.4
Al	30.8	4.3
Mn	18.1	2.6

15% 10% 15% 60%

$Mn_3Al_2Si_3O_{12}$

(spessartine / spessartite)

3

Element	Atomic Fraction (%)	Atomic Error (%)
O	55.8	2.6
Al	9.6	1.8
Si	16.8	2.7
Mn	17.8	2.4

Amorphous phase

1100–1200 ° C cooling at:
400 °C /h **amorphous**
5 °C/h **Crystalline**

[1] G. C. Lau et al. Phys Rev B 80, 214414 (2009)

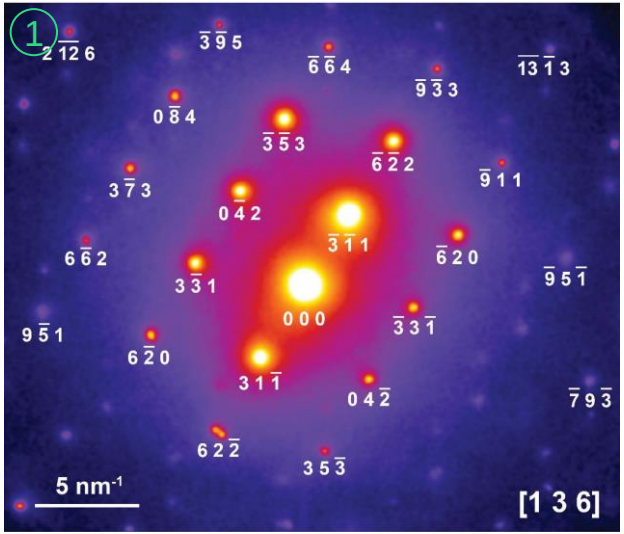

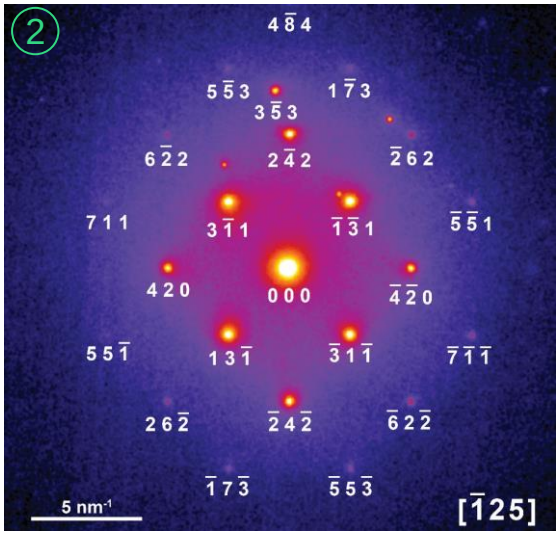

INDEXATION: Structure type Spinel#MgAl2O4

Phase diagram SiO_2-MnO-Al_2O_3

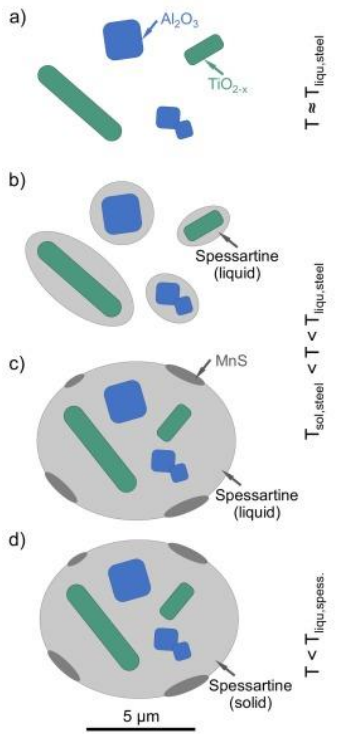

R. Wagner, R. Lehnert, E. Storti, L. Ditscherlein, C. Schröder, S. Dudczig, U.A. Peuker, O. Volkova, C.G. Aneziris, H. Biermann, A. Weidner, **Nanoindentation** of alumina and multiphase inclusions in 42CrMo4 steel, Materials Characterization, 193, (2022) 112257

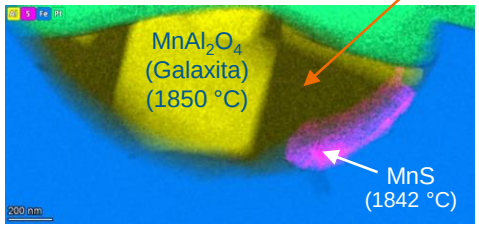

$Mn_3Al_2Si_3O_{12}$ (spessartine) (1249 °C)

Ref. [1]

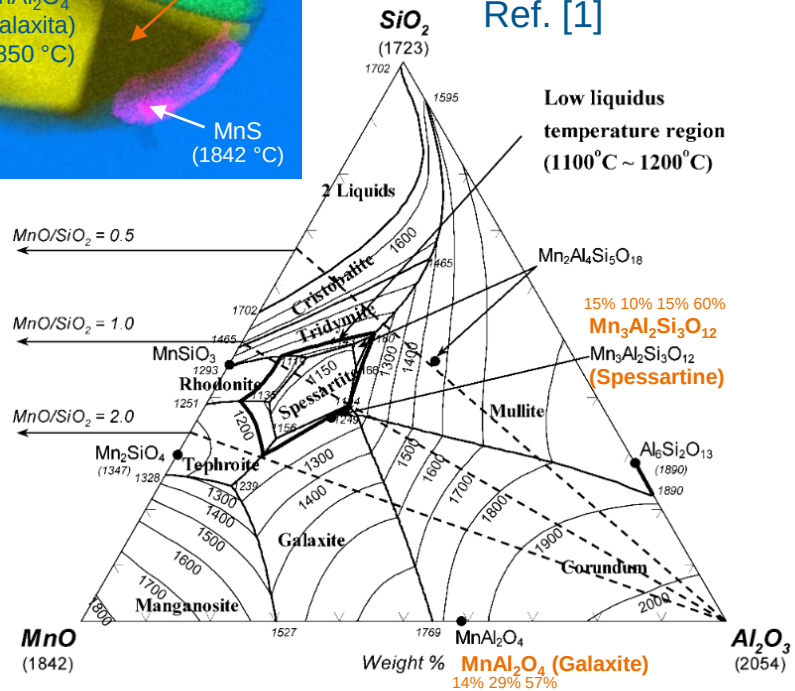

Fig. 2. Calculated liquidus surface of the MnO–SiO_2–Al_2O_3 system (temperature in degrees Celsius).

Brittle behaviour

↓

Inclusions with low plasticity

↓

High melting points inclusions (Al_2O_3)

Reduce harmful effect [1-2]

Low melting point high plasticity inclusions

↓

Low liquidus region (1200°C)

$Mn_3Al_2Si_3O_{12}$ (Spessartine)

[1] Youn-Bae Kang, Hae-Geon Lee. Inclusions ISIJ International, 44 (2004) 1006

[2] Jing Zhang, Fu-ming Wang, Chang-rong Li. International Journal of Minerals, Metallurgy and Materials 21 (2014) 647

Fracture of mini C(T)

Belt line specimen: Trepan #6, B6C12.3-B

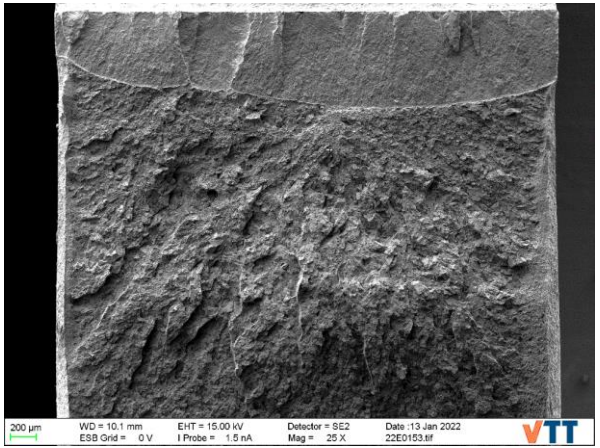

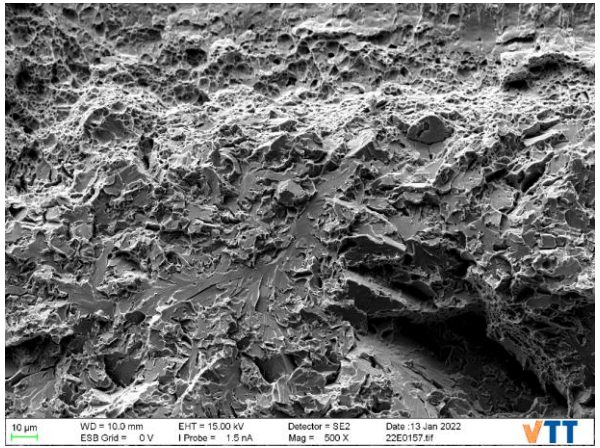

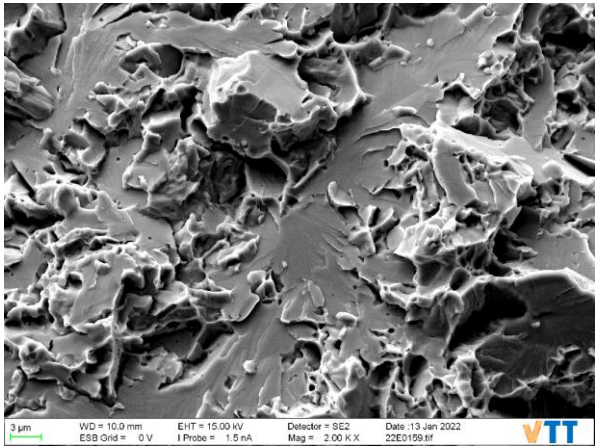

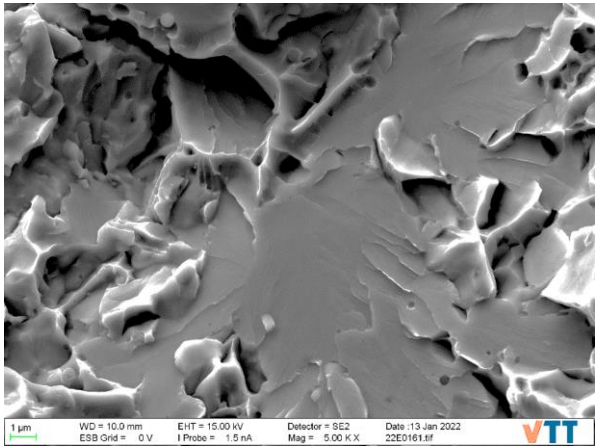

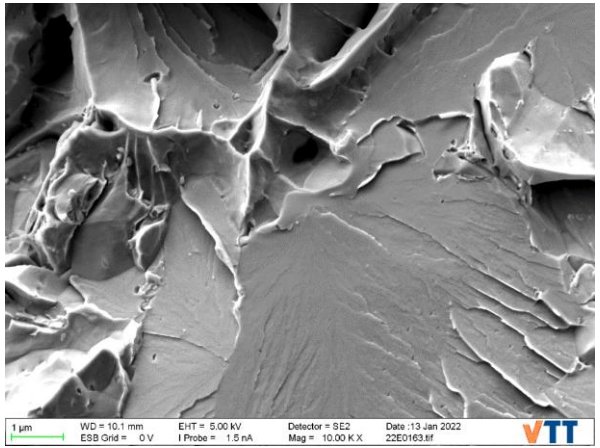

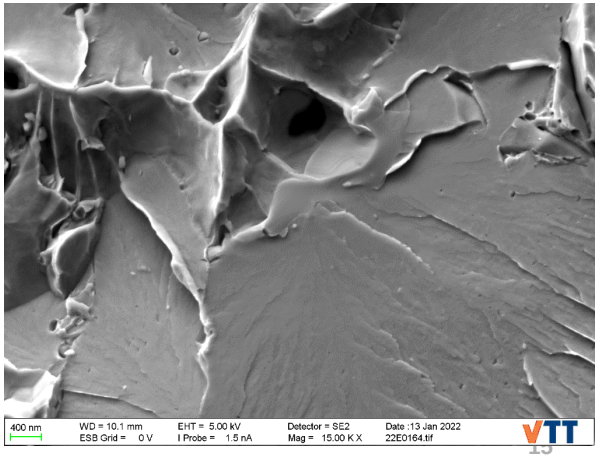

STEM

Belt line specimen: Trepan #6, B6C12.3-B

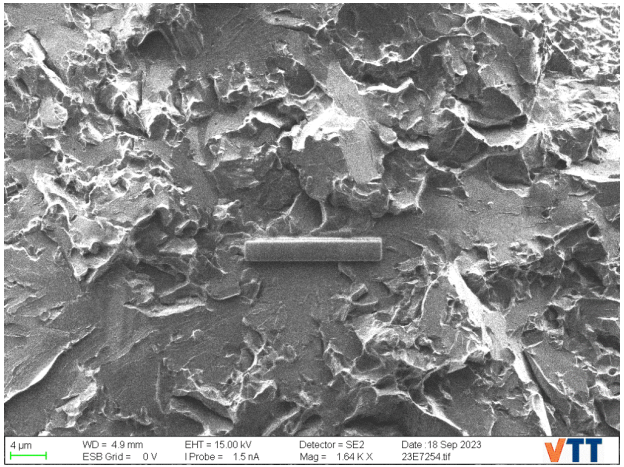

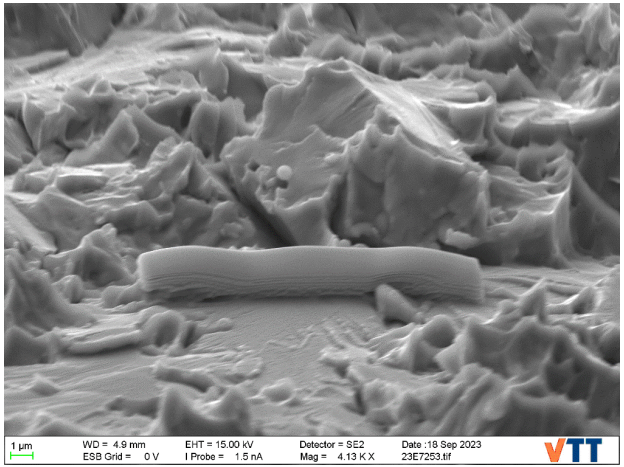

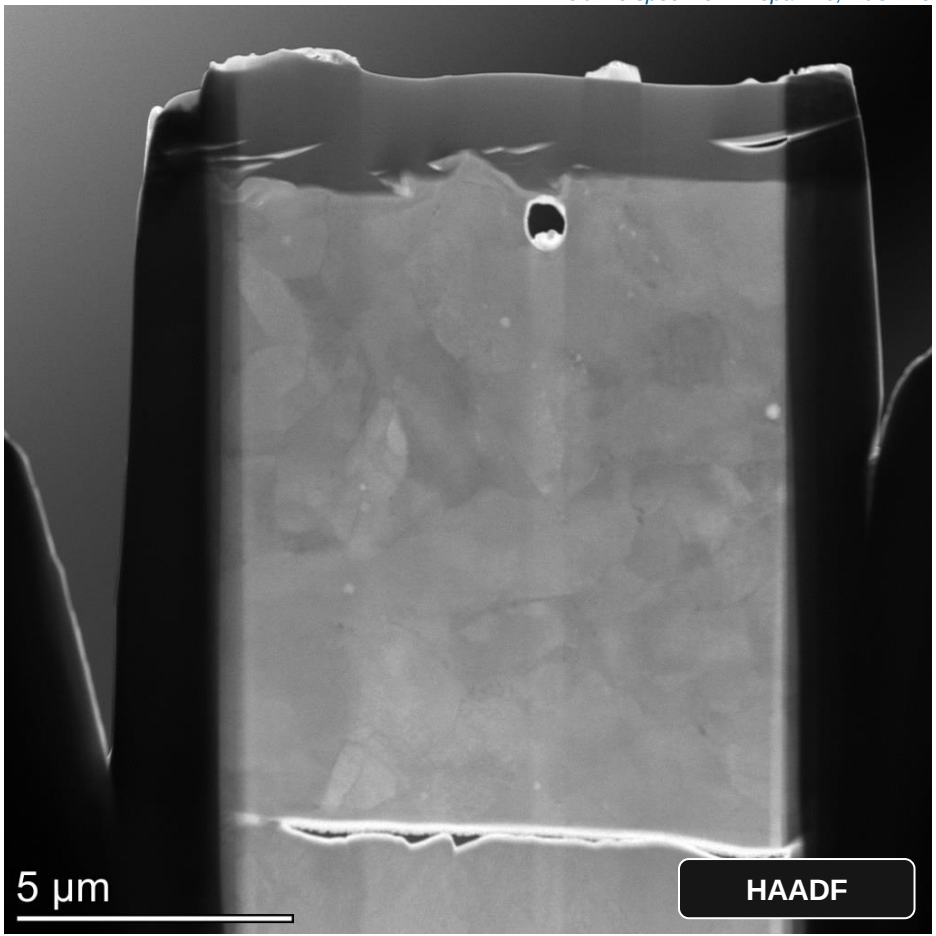

Belt line specimen: Trepan #6, B6C12.3-B

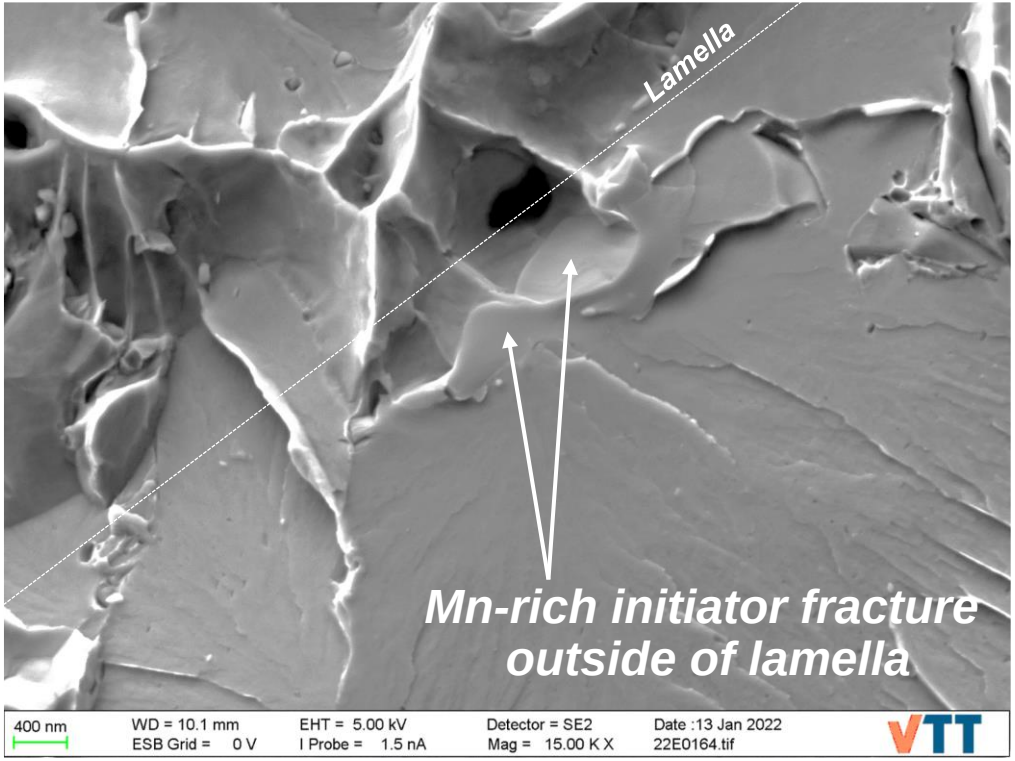

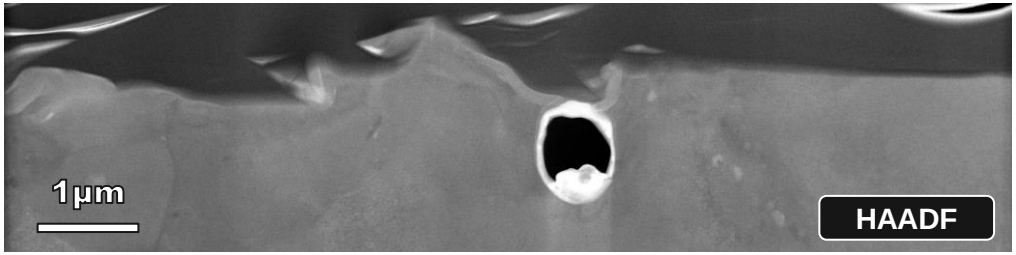

BF

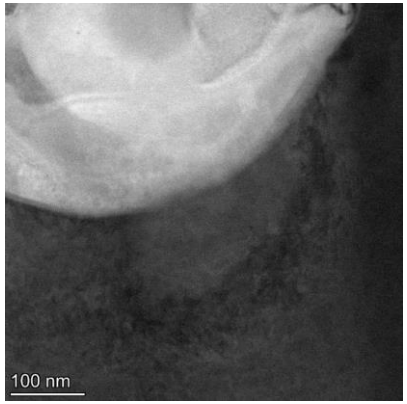

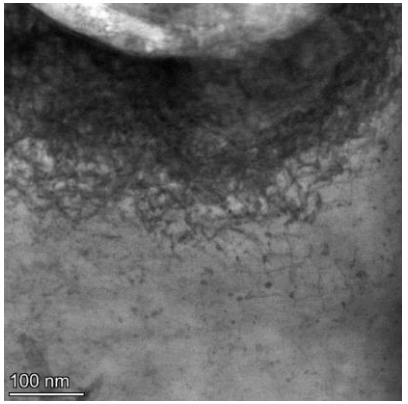

HAADF

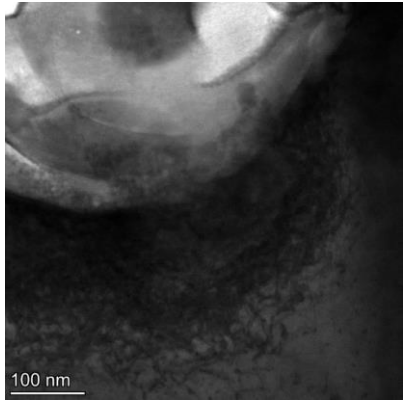

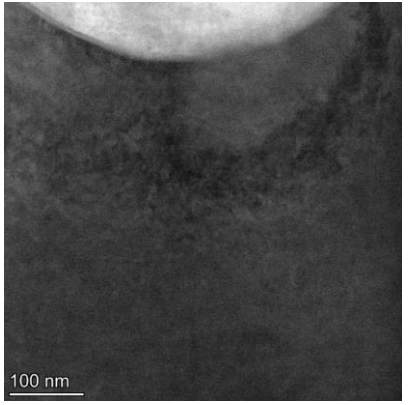

STEM

Belt line specimen: Trepan #6, B6C12.3-B

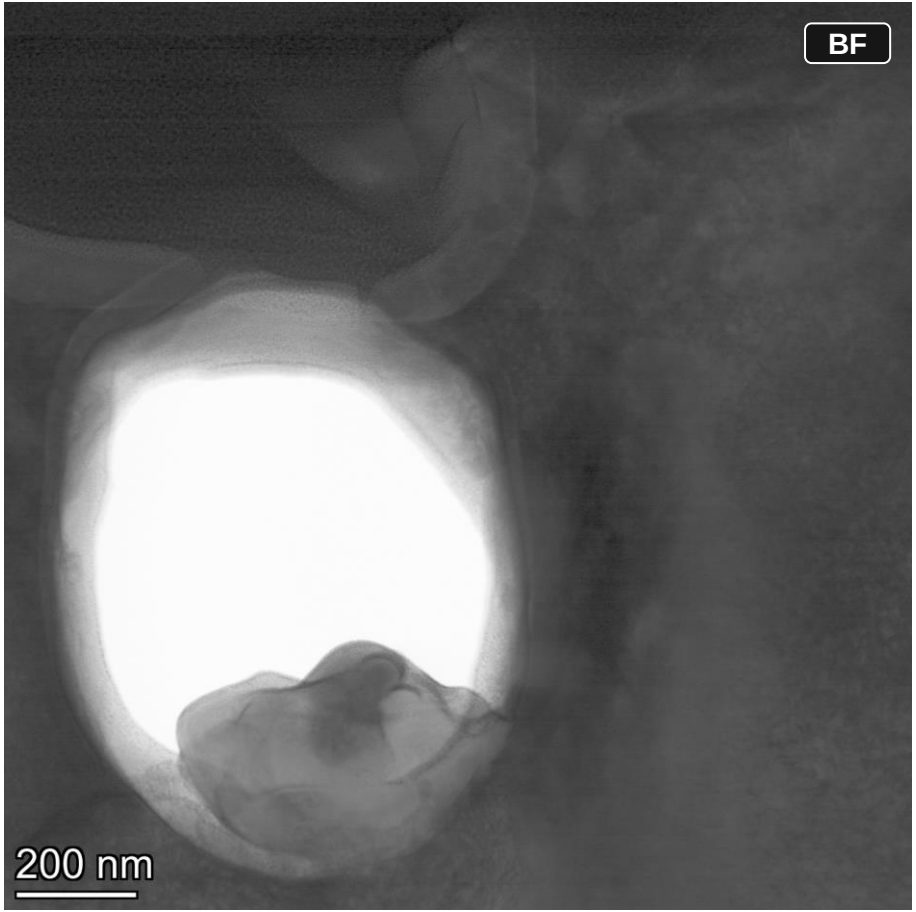

EDS (Net)

Belt line specimen: Trepan #6, B6C12.3-B

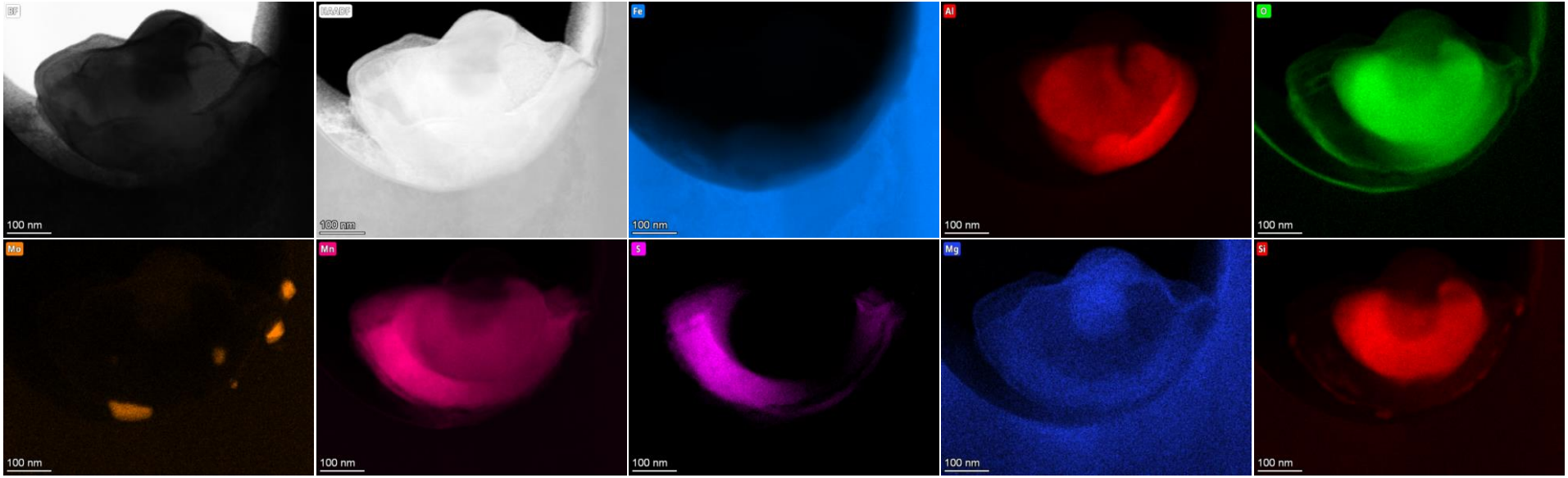

EDS Mix

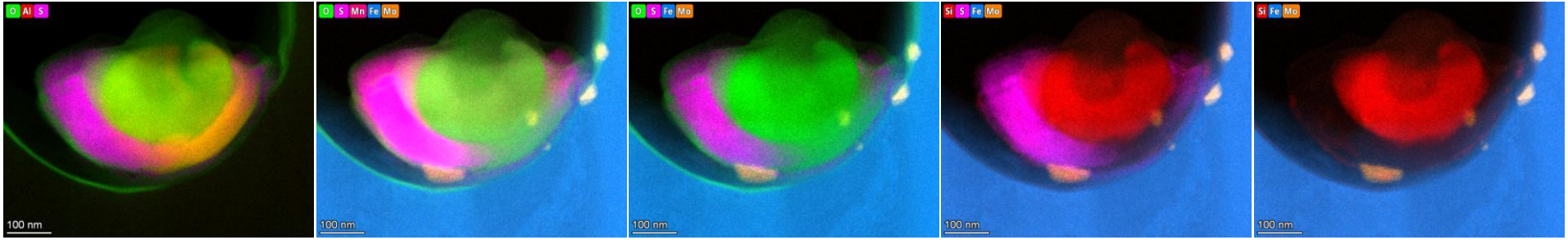

EDS (at)

Belt line specimen: Trepan #6, B6C12.3-B

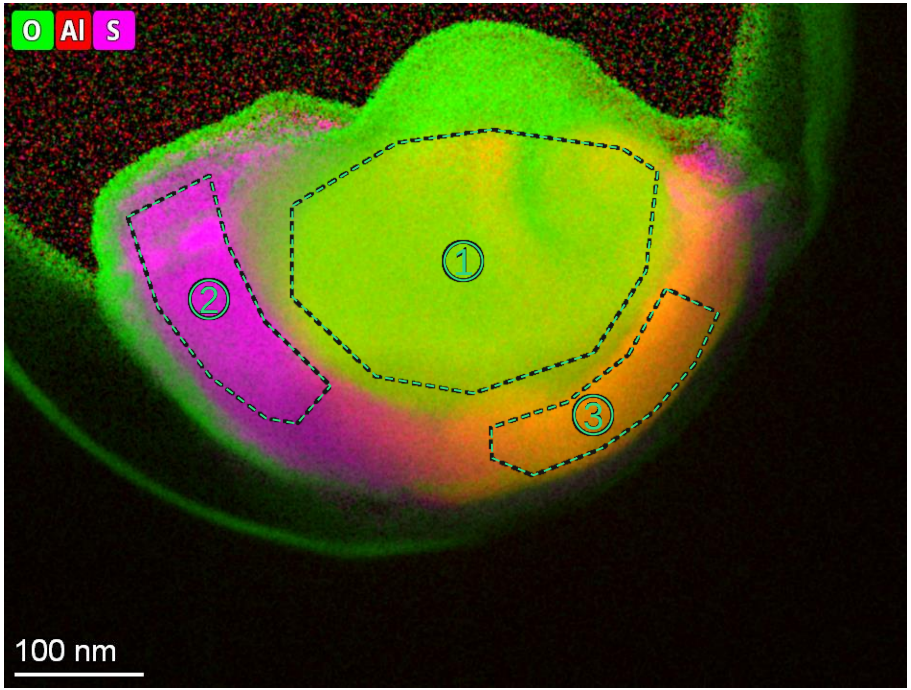

15% 10% 15% 60%

$Mn_3Al_2Si_3O_{12}$

(spessartine / spessartite)

① Element	Atomic Fraction (%)	Mass Fraction (%)
O	57.9	34.7
Al	10.5	10.6
Si	10.2	10.8
Mn	21.4	43.9

1MnO-3MnS (50Mn-37.5S-12.5O)

② Element	Atomic Fraction (%)	Mass Fraction (%)
O	12.2	4.7
S	37.7	29.1
Mn	50.1	66.3

2MnO-1Al_2O_3 (22Mn-22Al-56O)

③ Element	Atomic Fraction (%)	Mass Fraction (%)
O	56.1	33.6
Al	22.9	23.2
Mn	21.0	43.2

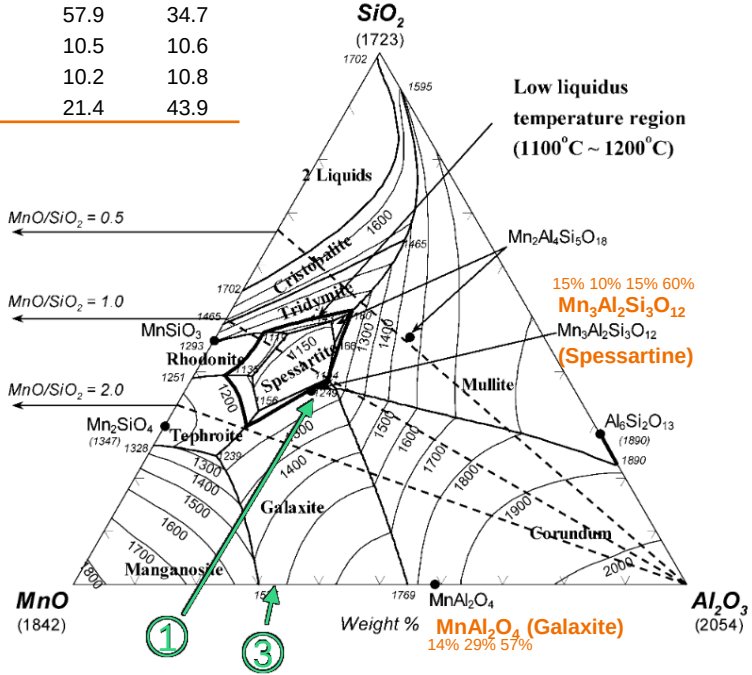

Summary

Two FIB liftouts were extracted from the fracture initiation sites of mini-C(T) specimens, and the TEM characterization showed the following:

a) **From the RPV head weld:**
   - A spherical non-metallic inclusion of 1.5 µm diameter, acting as initiation fracture, was broken in half.
   - The inclusion is formed by some cuboidal galaxite (MnMg)Al_2O_4 (600 nm of length) embedded in an amorphous spessartine $Mn_3Al_2Si_3O_{12}$. The external periphery contained a MnS (200x500 nm) and small particles (<80 nm) of Mo-rich and nitrides.

b) **From the axial beltline weld:**
   - A spherical non-metallic inclusion of 500 nm diameter was characterized. This was found next to the Mn-rich inclusion acting as fracture initiator.
   - The inclusion is formed by an amorphous spessartine $Mn_3Al_2Si_3O_{12}$ and two crystalline 1MnO-3MnS & 2MnO-1Al_2O_3 oxides. The external periphery contained small Mo-rich particles (<90 nm).

beyond
the obvious

Dr Pedro A. Ferreirós

Pedro.Ferreiros@vtt.fi

Advanced Materials for Nuclear Energy
VTT Technical Research Centre of Finland Ltd., Finland